JSCSEN 91(6)559-663(2026)

ISSN 1820-7421(Online)

Journal of the Serbian Chemical Society

Electronic version

VOLUME 91

No 6

BELGRADE 2026

Available on line at

www.shd.org.rs/JSCS/

The **Journal of the Serbian Chemical Society** (formerly Glasnik Hemijskog društva Beograd), one volume (12 issues) per year, publishes articles from the fields of chemistry. The **Journal** is financially supported by the **Ministry of Science, Technological Development and Innovation of the Republic of Serbia.**
Articles published in the **Journal** are indexed in **Clarivate Analytics products: Science Citation Index-Expanded™** – accessed *via* **Web of Science®** and **Journal Citation Reports®**.
Impact Factor announced for the year 2024: **0.700; 5-year Impact Factor**: **0.900**.
Articles appearing in the **Journal** are also abstracted by: **Scopus, Chemical Abstracts Plus (CAplus℠), Directory of Open Access Journals, Referativnii Zhurnal (VINITI), RSC Analytical Abstracts, EuroPub, Pro Quest** and **Asian Digital Library.**

Publisher:	**Serbian Chemical Society**, Karnegijeva 4/III, P. O. Box 36, 1120 Belgrade 35, Serbia tel./fax: +381–11–3370–467, E-mails: **Society** – shd@shd.org.rs; **Journal** – jscs@shd.org.rs Home Pages: **Society** – http://www.shd.org.rs/, **Journal** – http://www.shd.org.rs/JSCS/
Internet Service:	Contents, Abstracts and full papers (from Vol. 64, No. 1, 1999) are available in the electronic form at the Web Site of the **Journal** (http://www.shd.org.rs/JSCS/).
Former Editors:	**Nikola A. Pušin** (1930–1947), **Aleksandar M. Leko** (1948–1954), **Panta S. Tutundžić** (1955**–**1961), **Miloš K. Mladenović** (1962–1964), **Đorđe M. Dimitrijević** (1965–1969), **Aleksandar R. Despić** (1969–1975), **Slobodan V. Ribnikar** (1975–1985), **Dragutin M. Dražić** (1986–2006), **Branislav Ž. Nikolić** (2006-2026).
Editor-in-Chief:	DUŠAN **SLADIĆ**, Faculty of Chemistry, University of Belgrade
Deputy Editors:	MARIO **ZLATOVIĆ**, Faculty of Chemistry, University of Belgrade, VLADIMIR **PANIĆ**, Institute of Chemistry, Technology and Metallurgy, University of Belgrade
Sub editors:	
,	
Organic Chemistry	DEJAN **OPSENICA**, Institute of Chemistry, Technology and Metallurgy, University of Belgrade JÁNOS **CSANÁDI**, Faculty of Science, University of Novi Sad
Biochemistry and Biotechnology	OLGICA **NEDIĆ**, INEP – Institute for the Application of Nuclear Energy, University of Belgrade
Inorganic Chemistry	BILJANA **GLIŠIĆ**, Faculty of Science, University of Kragujevac
Theoretical Chemistry	MATIJA **ZLATAR**, Institute of Chemistry, Technology and Metallurgy, University of Belgrade MILOŠ **MILIČIĆ**, Faculty of Chemistry, University of Belgrade
Physical Chemistry	LJILJANA **DAMJANOVIĆ-VASILIĆ**, Faculty of Physical Chemistry, University of Belgrade
Electrochemistry	SNEŽANA **GOJKOVIĆ**, Faculty of Technology and Metallurgy, University of Belgrade
Analytical Chemistry	RADA **BAOŠIĆ**, Faculty of Chemistry, University of Belgrade
Polymers	BRANKO **DUNJIĆ**, Faculty of Technology and Metallurgy, University of Belgrade
Thermodynamics	MIRJANA **KIJEVČANIN**, Faculty of Technology and Metallurgy, University of Belgrade
Chemical Engineering	TATJANA **KALUĐEROVIĆ RADOIČIĆ**, Faculty of Technology and Metallurgy, University of Belgrade
Materials	RADA **PETROVIĆ**, Faculty of Technology and Metallurgy, University of Belgrade
Metallic Materials and Metallurgy	ANA **KOSTOV**, Mining and Metallurgy Institute Bor, University of Belgrade
Environmental and Geochemistry	VESNA **ANTIĆ**, Faculty of Agriculture, University of Belgrade
History of and Education in Chemistry	DRAGICA **TRIVIĆ**, Faculty of Chemistry, University of Belgrade
English Language Editors:	VLATKA **VAJS**, Serbian Chemical Society MIROSLAV **PAVLOVIĆ**, Institute of Chemistry, Technology and Metallurgy, University of Belgrade
Journal Manager & Web Master:	MARIO **ZLATOVIĆ**, Faculty of Chemistry, University of Belgrade
Office:	VERA **ĆUŠIĆ**, Serbian Chemical Society

Editorial Board
From abroad: **R. Adžić**, Brookhaven National Laboratory (USA); **A. Casini**, University of Groningen (The Netherlands); **G. Cobb**, Baylor University (USA); **D. Douglas**, University of British Columbia (Canada); **G. Inzelt**, Etvos Lorand University (Hungary); **J. Kenny**, University of Perugia (Italy); **Ya. I. Korenman**, Voronezh Academy of Technology (Russian Federation); **M. D. Lechner**, University of Osnabrueck (Germany); **S. Macura**, Mayo Clinic (USA); **M. Spiteller**, INFU, Technical University Dortmund (Germany); **M. Stratakis**, University of Crete (Grecce); **M. Swart**, University de Girona (Cataluna, Spain); **G. Vunjak-Novaković**, Columbia University (USA); **P. Worsfold**, University of Plymouth (UK); **J. Zagal**, Universidad de Santiago de Chile (Chile).
From Serbia: **B. Abramović**, **V. Antić**, **R. Baošić**, **V. Beškoski**, **J. Csanadi**, **Lj. Damjanović-Vasilić**, **A. Dekanski**, **V. Dondur**, **B. Dunjić**, **M. Đuran, B. Glišić, S. Gojković**, **I. Gutman**, **B. Jovančićević**, **I. Juranić**, **T. Kaluđerović Radoičić**, **L. Katsikas**, **M. Kijevčanin**, **A. Kostov**, **V. Leovac**, **S. Milonjić**, **V.B. Mišković-Stanković**, **O. Nedić**, **D. Opsenica**, **V. Panić**, **M. Pavlović**, **M. Petkovska**, **R. Petrović**, **I. Popović**, **B. Radak**, **S. Ražić**, **D. Sladić**, **S. Sovilj**, **S. Šerbanović**, **B. Šolaja**, **Ž. Tešić**, **D. Trivić**, **V. Vajs, M. Zlatović**.

Subscription: The annual subscription rate is **150.00 €** including postage (surface mail) and handling. For Society members from abroad rate is **50.00 €**. For the proforma invoice with the instruction for bank payment contact the Society Office (E-mail: shd@shd.org.rs) or see JSCS Web Site: http://www.shd.org.rs/JSCS/, option Subscription.
Godišnja pretplata: Za članove SHD: **2.500,00 RSD**, za penzionere i studente: **1000,00 RSD**, a za ostale: **3.500,00 RSD**:za organizacije i ustanove: **16.000,00 RSD**. Uplate se vrše na tekući račun Društva: **205-13815-62**, poziv na broj **320**, sa naznakom "pretplata za JSCS".

Nota: Radovi čiji su svi autori članovi SHD prioritetno se publikuju.
Odlukom Odbora za hemiju Republičkog fonda za nauku Srbije, br. 66788/1 od 22.11.1990. godine, koja je kasnije potvrđena odlukom Saveta Fonda, časopis je uvršten u kategoriju međunarodnih časopisa (**M-23**). Takođe, aktom Ministarstva za nauku i tehnologiju Republike Srbije, 413-00-247/2000-01 od 15.06.2000. godine, ovaj časopis je proglašen za publikaciju od posebnog interesa za nauku. **Impact Factor** časopisa objavljen za 2024. godinu je **0,700**, a petogodišnji **Impact Factor 0,900**.

Journal of the Serbian Chemical Society
JSCS-info@shd.org.rs • www.shd.org.rs/JSCS

J. Serb. Chem. Soc. Vol. 91, No. 6 (2026)

CONTENTS*

Published by the Serbian Chemical Society
Karnegijeva 4/III, P.O. Box 36, 11120 Belgrade, Serbia
Printed by the Faculty of Technology and Metallurgy
Karnegijeva 4, P.O. Box 35-03, 11120 Belgrade, Serbia

* For colored figures in this issue please see electronic version at the Journal Home Page: http://www.shd.org.rs/JSCS/

Journal of the Serbian Chemical Society
JSCS-info@shd.org.rs • www.shd.org.rs/JSCS
J. Serb. Chem. Soc. 91 (6) 559–571 (2026)
JSCS–5510
Original scientific paper
Published 6 July, 2026

December Armageddon: Biothermodynamic analysis of rhinoviruses based on the calculation of Gibbs energy change of antigen–receptor binding and biosynthesis of rhinovirus particles

MARKO E. POPOVIĆ[1]*, MARIJANA PANTOVIĆ PAVLOVIĆ[1,2] and MARIJA MIHAILOVIĆ[1]

[1]*University of Belgrade, Institute of Chemistry, Technology and Metallurgy, Njegoševa 12, 11000 Belgrade, Serbia and* [2]*University of Belgrade, Centre of Excellence in Chemistry and Environmental Engineering – ICTM, Belgrade, Serbia*

(Received 11 January, revised 12 February, accepted 8 April 2026)

Abstract: The subject of this research is a battle that is repeated every year and spreads epidemically across different territories, causing a large number of infected cases and casualties. Infections with rhinovirus are well known to the biomedical sciences. However, for a deeper understanding of the causes of rhinovirus disease and virus-host interaction (infection) it is necessary to understand them from the perspective of chemistry and biothermodynamics. This paper presents the empirical formulas, the driving forces of rhinovirus-host interactions, as well as a mechanistic model of virus-host interactions at the cell membrane and in the cytoplasm. Based on the described data, conclusions are presented about why 50 % of infections of the upper respiratory tract are caused by rhinoviruses. For the first time, the changes in Gibbs energies of biosynthesis of virus particles of rhinoviruses A2, B3 and C15, as well as change in Gibbs energy of binding of rhinovirus A2 are presented, which are needed to understand the lifecycle of rhinoviruses.

Keywords: enthalpy; entropy; growth reactions; empirical formulas; molar mass.

INTRODUCTION

Rhinovirus is the most common cause of seasonal respiratory infections. It's estimated that rhinovirus causes of 50 % of all viral respiratory infections. Rhinovirus belongs to the group of RNA viruses.[1,2] The rhinovirus virion is unenveloped.[3,4] The virion consists of 60 copies each of the structural proteins VP1, VP2, VP3 and VP4.[5–8] The viral structural proteins form a capsid that surrounds a

* Corresponding author. E-mail: marko.popovic@ihtm.bg.ac.rs
https://doi.org/10.2298/JSC260111019P

single-stranded positive-sense RNA genome.[9,10] Rhinoviruses are classified into RV-A, RV-B and RV-C species, each of which contains many subvariants.[11,12]

From the above, we can conclude that rhinovirus represents a macromolecular assembly that consists of nucleotides and amino acids. As such, rhinoviruses can be understood, not just as a biological entities, but also as chemical entities.[13] Due to their chemical nature, viruses can be characterized by an empirical formula, as well as thermodynamic properties (changes in enthalpy, entropy and Gibbs energy).[14] Rhinovirus performs life processes inside host cells.[15] In essence, life processes represent chemical reactions, which obey the laws of chemical kinetics and thermodynamics, and are led by a driving force. For example, binding of viruses to host cells is a reaction similar to protein–ligand interactions.[14,16] It is led by a driving force – change in Gibbs energy of binding.[14,17] Virus multiplication also represents a reaction of polymerization of amino acids into viral proteins and nucleotides into viral nucleic acid,[13,41–45] which then undergoes self-assembly into virus particles.[23,46,47] A virus, during the life process of multiplication, performs hijacking of the host-cell metabolic machinery, as well as the material resources of host cells (nucleotides, amino acids, *etc*.).[18–20] The reaction of polymerization is led by its driving force – change in Gibbs energy of biosynthesis.[21,22] Finally, the synthesized virus parts undergo the process of self-assembly and accumulate inside the host cell, which with time can lead to cell lysis and an increase in the number of virus particles inside the host organism.[23] The consequence of cell lysis is damage to the function and morphology of the tissue of the host organism.[13,24]

The aim of this paper is to chemically and thermodynamically characterize the rhinoviruses and make a comparison with other known viruses that have been described in the literature. Moreover, the known lifecycle of rhinoviruses is described using the fundamental physicochemical laws that describe virus-host interactions.

EXPERIMENTAL PROCEDURE

Data sources

The genetic sequences of the rhinoviruses were taken from the NCBI database.[25] The analyzed genetic sequences can be found under the accession numbers: X02316.1 for rhinovirus A2, NC 038312.1 for rhinovirus B3 and GU219984.1 for rhinovirus C15.

The protein sequences of the rhinoviruses were taken from the UniProt database.[26] The analyzed protein sequences can be found under the accession numbers: P04936 for rhinovirus A2, Q82081 for rhinovirus B3 and E5D8F2 for rhinovirus C15 (PTM/Processing section). The morphology of the rhinovirus particles was taken from the literature.[5–8]

The dissociation equilibrium constants, K_d, of rhinoviruses A2 and B3 were taken from the literature.[27,28] They were measured with atomic force spectroscopy and surface plasmon resonance.[27,28]

Atom counting method

The molecular formulas, empirical formulas and molar masses of the rhinoviruses were calculated with the atom counting method, as described in the literature.[29,30] The atom counting

method is a computational approach for the calculation of chemical properties of micromolecules and macromolecular assemblies.[29,30] It is applied with a computer program, which goes along the genetic and protein sequences and adds atoms that come from nucleotide and amino acid residues.[29,30] For macromolecular assemblies, the numbers of atoms coming from constituent molecules are multiplied by the number of their copies in the macromolecular assembly.[29,30]

Patel–Erickson–Battley model

Thermodynamic properties of the live matter of rhinoviruses were calculated with the Patel–Erickson–Battley model, as described in the literature.[13,14] Based on the empirical formula, the degree of reduction, E, was calculated as:

$$E = 4n_C + n_H - 2n_O - 0n_N + 5n_P + 6n_S \quad (1)$$

where n_C, n_H, n_O, n_N, n_P and n_S are the numbers of C, H, O, N, P and S atoms in the empirical formula.[31,32] Then the Patel–Erickson equation was used to find the enthalpy change of combustion, $\Delta_C H^o$, of live matter:[31,32]

$$\Delta_C H^0(\text{bio}) = -111.4 \frac{\text{kJ}}{\text{C-mol}} E \quad (2)$$

The enthalpy change of combustion was then converted into the enthalpy change of formation, $\Delta_f H^o$, of live matter with Hess's law, as described in the literature.[13,32]

The Battley equation was used to calculate the molar entropy, S_m^o, of live matter based on its empirical formula:

$$S_m^0(\text{bio}) = 0.187 \sum\nolimits_J \frac{S_m^0(J)}{a_J} n_J \quad (3)$$

where $S^o_m(J)$ is the molar entropy of element J, a_J is the number of atoms of element J in its standard state elemental form, n_J is the number of atoms of element J in the empirical formula of live matter and the summation is made over all J elements that are present in the live matter.[33,34] Moreover, change in entropy of formation, $\Delta_f S^o$, of live matter was calculated with the modified Battley equation:[33,34]

$$\Delta_f S^0(\text{bio}) = -0.813 \sum\nolimits_J \frac{S_m^0(J)}{a_J} n_J \quad (4)$$

The change in Gibbs energy of formation, $\Delta_f G^o$, of live matter was calculated based on its enthalpy change of formation, $\Delta_f H^o$, and entropy change of formation, $\Delta_f S^o$:

$$\Delta_f G^0(\text{bio}) = \Delta_f H^0(\text{bio}) - T\Delta_f S^0(\text{bio}) \quad (5)$$

where T is temperature.[13]

The Patel–Erickson–Battley model has been widely used in research on the thermodynamic properties of organisms.[49,50] It gives results in good agreement with experimental data.[33,34,50] The uncertainty in $\Delta_C H^o$ calculated with the Patel–Erickson equation is 5.36 %.[50] The uncertainty in S_m^o calculated with the Battley equation is 19.7 %.[33,34]

Biosynthesis reactions and thermodynamic properties

Biosynthesis reactions are macrochemical equations that show how new live matter is produced from nutrients by organisms.[13,14,48] The biosynthesis reactions of viruses have the form:

$$(\text{Amino acid}) + O_2 + HPO_4^{2-} + HCO_3^- \rightarrow (\text{Bio}) + SO_4 + H_2O + H_2CO_3 \quad (6)$$

where (Amino acid) represents amino acids with the empirical formula $CH_{1.798}O_{0.4831}N_{0.2247}S_{0.022472}$ and (Bio) represents the empirical formula of new live matter. Amino acids are the source of energy, carbon, nitrogen and sulfur.[1,13,14] O_2 is the electron acceptor.[13,14,35] HPO_4^{2-} is the source of phosphorus.[1,13] SO_4^{2-} is an additional metabolic product that takes excess sulfur.[13,14] HCO_3^- and H_2CO_3 form a bicarbonate buffer that maintains a constant pH.[13,14]

The biosynthesis reactions and thermodynamic properties of live matter were used to calculate thermodynamic properties of biosynthesis with Hess's law:

$$\Delta_{bs}H^0 = \sum_{products} \nu \Delta_f H^0 - \sum_{reactants} \nu \Delta_f H^0 \quad (7)$$

$$\Delta_{bs}S^0 = \sum_{products} \nu S_m^0 - \sum_{reactants} \nu S_m^0 \quad (8)$$

$$\Delta_{bs}G^0 = \sum_{products} \nu \Delta_f G^0 - \sum_{reactants} \nu \Delta_f G^0 \quad (9)$$

where $\Delta_{bs}H^o$ is the enthalpy change of biosynthesis, $\Delta_{bs}S^o$ change in the entropy of biosynthesis, $\Delta_{bs}G^o$ change in Gibbs energy of biosynthesis and ν represents a stoichiometric coefficient.[13,14]

Antigen–receptor binding

Thermodynamic properties of antigen–receptor binding of rhinoviruses were calculated with the methodology of thermochemistry, as described in the literature.[13,14,16] Antigen–receptor binding represents a chemical reaction similar to protein–ligand interactions.[13,14,16] The reaction of antigen–receptor binding is:

$$(An) + (Re) \rightleftarrows (An - Re) \quad (10)$$

where (An) is the free virus antigen, (Re) is the free host cell receptor, while (An–Re) is the antigen–receptor complex.[13,14,16] The dissociation equilibrium constant, K_d, is given as:

$$K_d = \frac{[An][Re]}{[An - Re]} \quad (11)$$

where [An], [Re] and [An–Re] are the concentrations of the free virus antigen, free host cell receptor and antigen–receptor complex.[13,14,16] The binding equilibrium constant, K_B, was calculated from K_d as:[13,14,16]

$$K_B = \frac{1}{K_d} = \frac{[An - Re]}{[An][Re]} \quad (12)$$

The change in Gibbs energy of binding, $\Delta_B G^o$, was calculated from K_B as:

$$\Delta_B G^0 = -RT \ln K_B \quad (13)$$

where T is temperature and R is the universal gas constant.[13,14,16]

RESULTS AND DISCUSSION

Rhinovirus, in terms of its morphology might not be quite the simplest, but it belongs to the simpler (and smaller) virus particles. It can be characterized chemically by an empirical formula, which is different from those of all other viruses and thermodynamic properties that represent the driving force for physiological processes that comprise the lifecycle of the virus. Having in mind its simplicity, it can be expected that the process of virus multiplication proceeds relatively rapidly

compared to that of other larger viruses. Indeed, as was said in the introduction, infections caused by rhinovirus comprise half of all respiratory viral infections.

Rhinovirus A is characterized by the empirical formula $CH_{1.4750}O_{0.3938}N_{0.2973}P_{0.0222}S_{0.0060}$, which is different from that of the JN.1 variant of SARS-CoV-2 $CH_{1.6390}O_{0.2841}N_{0.2300}P_{0.006439}S_{0.003765}$ (Ref. 36) or coxsackievirus A $CH_{1.4665}O_{0.4007}N_{0.2963}P_{0.023292}S_{0.005318}$ (Ref. 30). The molar mass of a rhinovirus particle is 7.961 MDa. The molar masses of other viruses are 219.2 MDa for the virion of the JN.1 variant of SARS-CoV-2[36] and 8.16 MDa for the virion of coxsackievirus A.[30] The molar mass of rhinovirus is similar to that of coxsackievirus, while the molar mass of a SARS-CoV-2 particle is 27 times greater. The reason is that a SARS-CoV-2 particle is more complex and contains, in addition to the nucleocapsid, a lipid envelope with viral spike and membrane proteins. Empirical formulas of rhinoviruses are given in Table I. Molecular formulas of rhinoviruses are given in Table II.

TABLE I. Empirical formulas of rhinoviruses. The empirical formulas have the form $CH_{n_H}O_{n_O}N_{n_N}P_{n_P}S_{n_S}$, where n_H, n_O, n_N, n_P and n_S are the numbers of H, O, N, P and S atoms present in live matter per carbon atom

Name	n_H	n_O	n_N	n_P	n_S	Mr / g C-mol^{-1}
Rhinovirus A2	1.4750	0.3938	0.2973	0.0222	0.0060	24.84
Rhinovirus B3	1.4861	0.3986	0.2958	0.0225	0.0053	24.89
Rhinovirus C15	1.4727	0.3918	0.2962	0.0223	0.0068	24.82

TABLE II. Molecular formulas of rhinoviruses. The molecular formulas have the form $C_{m_C}H_{m_H}O_{m_O}N_{m_N}P_{m_P}S_{m_S}$, where m_C, m_H, m_O, m_N, m_P and m_S are the total numbers of C, H, O, N, P and S atoms in the virus particles. Mr(tot) represents the total molar mass of the virus particle

Name	m_C	m_H	m_O	m_N	m_P	m_S	Mr(tot) / MDa
Rhinovirus A2	320500	472733	126204	95297	7102	1920	7.961
Rhinovirus B3	319933	475467	127510	94635	7208	1680	7.965
Rhinovirus C15	319244	470164	125080	94557	7119	2160	7.924

Thermodynamic properties of the live matter of rhinovirus particles are given in Table III. Enthalpy changes of formation of rhinovirus particles are negative, which means that the particles have a lower total energy content than their constituent elements. The reason for this is the attraction of valence electrons of less electronegative elements (C, H, P and S) by more electronegative elements, O and N. Entropy changes of the virions are positive, which is in agreement with the third law of thermodynamics. Changes in Gibbs energy of formation of the virions are negative. This means that the usable energy content of the virions is lower than that of their constituent elements.

TABLE III. Thermodynamic properties of live matter of rhinoviruses: enthalpy changes of formation, $\Delta_f H^0$, standard molar entropy, $S_m{}^0$, and the change in Gibbs energy of formation, $\Delta_f G^0$

Name	$\Delta_f H^0$ / kJ C-mol^{-1}	$S_m{}^0$ / J C-mol^{-1} K^{-1}	$\Delta_f G^0$ / kJ C-mol^{-1}
Rhinovirus A2	–86.07	32.14	–44.41
Rhinovirus B3	–87.76	32.34	–45.85
Rhinovirus C15	–85.38	32.06	–43.82

Based on the empirical formulas, biosynthesis reactions of the rhinoviruses were formulated and are presented in Table IV. The biosynthesis reaction of rhinovirus A is:

$$1.3232CH_{1.798}O_{0.4831}N_{0.2247}S_{0.022472} + 0.4343O_2 + 0.0222HPO_4^{2-} + \\ + 0.0032HCO_3^- \rightarrow CH_{1.4750}O_{0.3938}N_{0.2973}P_{0.0222}S_{0.0060} + \\ 0.0237SO_4^{2-} + 0.1382H_2O + 0.3263H_2CO_3 \quad (14)$$

where $CH_{1.798}O_{0.4831}N_{0.2247}S_{0.022472}$ is the empirical formula of amino acids and $CH_{1.4750}O_{0.3938}N_{0.2973}P_{0.0222}S_{0.0060}$ is the empirical formula of the newly synthesized virions.

TABLE IV. Biosynthesis reactions of rhinoviruses. The biosynthesis reactions have the form (Amino acid) + O_2 + HPO_4^{2-} + HCO_3^- → (Bio) + SO_4^{2-} + H_2O + H_2CO_3, where (Amino acid) represents amino acids with the empirical formula $CH_{1.798}O_{0.4831}N_{0.2247}S_{0.022472}$ and (Bio) represents new live matter

Name	Reactants				Products			
	Amino acid	O_2	HPO_4^{2-}	HCO_3^-	Bio	SO_4^{2-}	H_2O	H_2CO_3
Rhinovirus A2	1.3232	0.4343	0.0222	0.0032	1	0.0237	0.1382	0.3263
Rhinovirus B3	1.3163	0.4260	0.0225	0.0036	1	0.0243	0.1333	0.3199
Rhinovirus C15	1.3180	0.4261	0.0223	0.0011	1	0.0229	0.1409	0.3192

Changes in thermodynamic properties of the biosynthesis reactions are given in Table V. The enthalpy changes of biosynthesis of rhinoviruses are negative. The negative enthalpy changes contribute favorably to the thermodynamic feasibility of the biosynthesis reactions. Entropy changes of biosynthesis of rhinoviruses are negative, due to the assembly of simpler precursors, like amino acids into more complex virus particles. Changes in Gibbs energy of biosynthesis of virus particles are negative, which means that the biosynthesis process is thermodynamically favorable.

Biosynthesis reactions show how new virus particles are produced from nutrients during multiplication of viruses. Every process in nature is led by a driving force.[37,38] Chemical reactions are led by a driving force – changes in Gibbs energy.[37,39,40] Phenomenological equations belong to nonequilibrium thermodynamics and show how rates of processes depend on their driving forces.[37,39,40] The

biosynthesis rate, r_{bs}, depends on the change in Gibbs energy of biosynthesis, $\Delta_{bs}G^{o}$, according to the biosynthesis phenomenological equation:

$$r_{bs} = -\frac{L_{bs}}{T}\Delta_{bs}G \quad (15)$$

where L_{bs} is the biosynthesis phenomenological coefficient.[13,14,37] According to the biosynthesis phenomenological equation, an organism with a more negative change in Gibbs energy of biosynthesis will have a higher biosynthesis rate.

TABLE V. Thermodynamic properties of biosynthesis of rhinoviruses: enthalpy changes of biosynthesis, $\Delta_{bs}H^{o}$, changes in entropy of biosynthesis, $\Delta_{bs}S^{o}$, and change in Gibbs energy of biosynthesis, $\Delta_{bs}G^{o}$

Name	$\Delta_{bs}H^{o}$ / kJ C-mol^{-1}	$\Delta_{bs}S^{o}$ / J C-mol^{-1} K^{-1}	$\Delta_{bs}G^{o}$ / kJ C-mol^{-1}
Rhinovirus A2	–202.58	–34.32	–192.59
Rhinovirus B3	–198.85	–33.75	–189.04
Rhinovirus C15	–198.64	–33.53	–188.89

A viral infection represents an interaction between a virus and its host organism. The interaction occurs at the chemical level. The virus enters the host cell and performs hijacking of the host metabolic machinery to multiply in a chemical process that requires energy and nutrients. The host cell also uses its metabolic machinery, energy and nutrients for the chemical reactions of reparation of damages that appear during life processes. Therefore, the virus–host interaction represents a competition for metabolic machinery, energy and nutrients. Virus multiplication and host cell reparation are competitive chemical reactions. According to the biosynthesis phenomenological equation, the reaction with a greater driving force (a more negative change in Gibbs energy) will dominate in the competition.

Rhinoviruses infect the tissues of the respiratory tract.[1] Fig. 1 shows changes in Gibbs energies of biosynthesis of rhinoviruses and their host tissue. The change in Gibbs energy of biosynthesis of the respiratory tract is –49.76 kJ C-mol^{-1}.[24] Changes in Gibbs energies of biosynthesis of rhinoviruses are between –188.89 and –192.59 kJ C-mol^{-1}. Therefore, rhinoviruses are characterized by a much greater driving force for multiplication, in the form of a more negative change in Gibbs energy of biosynthesis, than their host tissue. According to the biosynthesis phenomenological equation, due to this greater driving force, the biosynthesis rate of the rhinovirus is higher than that of its host cells. This means that the metabolic machinery of infected host cells will produce more new virus particles than host cell components. Moreover, the production of new virus particles will consume more nutrients and energy. Therefore, the virus performs hijacking of the host metabolic machinery, due to its more negative change in Gibbs energy of biosynthesis.

The initial interaction between the virus and its host cell occurs at the cell membrane with antigen-receptor binding. The process of antigen–receptor binding

is a chemical reaction similar to protein–ligand interactions. The driving force of the antigen–receptor binding reaction is the change in Gibbs energy of binding. Table VI presents changes in Gibbs energies of antigen–receptor binding of rhinoviruses. Rhinoviruses have negative changes in Gibbs energy of binding, which means that the antigen–receptor binding process is favorable. Due to the favorable Gibbs energy change, the virus can enter into the host cells and perform the infection process.

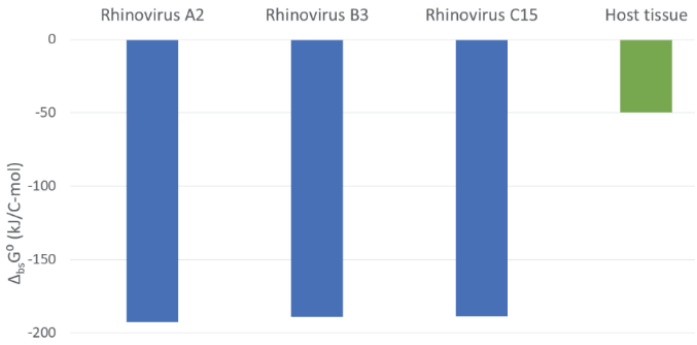

Fig. 1. Changes in Gibbs energy of biosynthesis of rhinoviruses and their host tissue. The change in Gibbs energy of biosynthesis represents the driving force for virus multiplication in host cells.[13]

TABLE VI. Thermodynamic properties of antigen–receptor binding of rhinoviruses: dissociation equilibrium constant, K_d, binding equilibrium constant, K_B, and standard change in Gibbs energy of binding, $\Delta_B G^o$. VLDLR1-8 is a soluble native-like recombinant very-low-density-lipoprotein receptor (VLDLR) fragment that encompasses the entire ligand binding domain, which is fused to maltose binding protein (MBP) at the N-terminus and to His_6 at the C-terminus. ICAM-1 is intercellular adhesion molecule 1 (also known as CD54). The K_d values were taken from Refs.[27,28] The $\Delta_B G^o$ value of rhinovirus B3 was taken from Ref.[28]

Name	Interaction	K_d / M	K_B / M^{-1}	$\Delta_B G^o$ / kJ mol^{-1}
Rhinovirus A2	Virion and VLDLR1-8	2.40E-08	4.17E+07	–43.49
Rhinovirus B3	Virion and ICAM-1	8.3E-07	1.20E+06	–34.72

Viruses interact with their host organisms during infection. Infections with different viruses can lead to different signs and symptoms of disease, even if they multiply in the same host tissue. Rhinovirus and SARS-CoV-2 cause infections of the respiratory tract. As of March 2026, the dominant SARS-CoV-2 variant worldwide is the XFG variant, while JN.1 has been designated as a variant of interest by WHO.[51,52] Change in the Gibbs energy of biosynthesis of the XFG variant of SARS-CoV-2 is –221.75 kJ $C\text{-}mol^{-1}$.[14] Change in the Gibbs energy of biosynthesis of the JN.1 variant of SARS-CoV-2 is –221.74 kJ $C\text{-}mol^{-1}$.[36] Change in Gibbs energy of biosynthesis of the XFG and JN.1 variants of SARS-CoV-2 are more negative than those of rhinoviruses. The more negative change in Gibbs

energy of biosynthesis means that the XFG and JN.1 variants of SARS-CoV-2 have a greater driving force for multiplication inside host cells. This means that the XFG and JN.1 variants of SARS-CoV-2 will multiply inside host cells at a greater rate, according to the biosynthesis phenomenological equation. The greater rate of multiplication leads to the production of more virus particles and greater damage to host tissues. Greater damage to host tissues leads to more pronounced signs and symptoms of disease. This means that the XFG and JN.1 variants of SARS-CoV-2 are characterized by greater pathogenicity than rhinoviruses. Therefore, rhinoviruses produce less pronounced signs and symptoms of disease and are characterized by a lower pathogenicity than SARS-CoV-2 due to their lower driving force for multiplication (a less negative change in Gibbs energy of biosynthesis).

The COVID-19 pandemic has shown how suddenly an emerging virus can appear and how rapidly it can spread all over the world. This is why it is important to have a method to predict the risk posed by an emerging virus to human health early after its appearance. This is often difficult since very little information is known about viruses soon after their appearance. The biothermodynamic methodology applied in this research uses genetic and protein sequence data that can be collected early during an epidemic caused by an emerging virus. It allows the prediction of the driving forces of antigen–receptor binding (change in Gibbs energy of binding) and virus multiplication inside host cells (change in Gibbs energy of biosynthesis). Based on these properties, it is possible to analyze the severity of signs and symptoms and the pathogenicity of the virus. This provides an advantage in the analysis of risks posed by emerging viruses to human health.

CONCLUSION

Chemical and thermodynamic properties of rhinoviruses A, B and C are reported, which include molecular formulas, empirical formulas, molar masses, biosynthesis reactions and thermodynamic properties of live matter, biosynthesis and binding. The chemical and thermodynamic properties of rhinoviruses are different from those of other viruses described in the literature.

During infection, virus multiplication and host cell reparation are chemical reactions that compete for energy and nutrients. Rhinoviruses have a much more negative change in Gibbs energy of biosynthesis than their host cells. This means that rhinovirus multiplication has a much greater driving force than host cell reparation. Due to the greater driving force of virus multiplication, the host metabolic machinery will produce more new virus particles than host cell components needed for reparation. Virus multiplication will also consume more energy and nutrients. This means that rhinoviruses hijack the metabolism of their host cells due to their greater driving force for multiplication in the form of a more negative Gibbs energy of biosynthesis.

Different viruses that interact with the same tissue during infection lead to signs and symptoms of different severity. Rhinoviruses and SARS-CoV-2 are respiratory viruses. However, change in Gibbs energy of biosynthesis of the XFG and JN.1 variants of SARS-CoV-2 are more negative than those of rhinoviruses, which means that the XFG and JN.1 variants of SARS-CoV-2 have a greater driving force for multiplication. Due to the greater driving force, according to the biosynthesis phenomenological equation, the XFG and JN.1 variants of SARS-CoV-2 will multiply faster and produce more new virus particles and greater damage to host tissue. The greater damage to host tissues will lead to more severe signs and symptoms of disease, as well as greater pathogenicity of the XFG and JN.1 variants of SARS--CoV-2. Therefore, different driving forces of multiplication lead to differences in the severity of signs and symptoms of disease and pathogenicity between rhinoviruses and SARS-CoV-2. The biothermodynamic methodology described in this research can be used in the analysis of risks posed to human health by emerging viruses.

NOMENCLATURE

VLDLR1-8 is a soluble native-like recombinant very-low-density-lipoprotein receptor (VLDLR) fragment that encompasses the entire ligand binding domain, which is fused to maltose binding protein (MBP) at the N-terminus and to His_6 at the C-terminus. ICAM-1 is intercellular adhesion molecule 1 (also known as CD54).

Acknowledgements. This work was supported by the Ministry of Science, Technological Development and Innovation of the Republic of Serbia (Grant No. 451-03-136/2025-03/ /200026).

ИЗВОД

ДЕЦЕМБАРСКИ АРМАГЕДОН: БИОТЕРМОДИНАМИЧКА АНАЛИЗА РИНОВИРУСА ЗАСНОВАНА НА ПРОРАЧУНУ ПРОМЕНЕ ГИБСОВЕ ЕНЕРГИЈЕ АНТИГЕН–РЕЦЕПТОР ВЕЗИВАЊА И БИОСИНТЕЗЕ ЧЕСТИЦА РИНОВИРУСА

МАРКО Е. ПОПОВИЋ[1], МАРИЈАНА ПАНТОВИЋ ПАВЛОВИЋ[1,2] и МАРИЈА МИХАИЛОВИЋ[1]

[1]Универзитет у Београду, Институт за хемију, технологију и металургију, Његошева 12, 11000 Београд и [2]Универзитет у Београду, Центар за хемију и инжењеринг животне средине – ИХТМ, Београд

Предмет овог истраживања је битка која се понавља сваке године и епидемијски се шири на различитим територијама, узрокујући велики број заражених случајева и жртава. Инфекције риновирусом су добро познате биомедицинским наукама. Инфекције риновирусима су добро познате биомедицинским наукама. Међутим, за дубље разумевање узрока болести риновируса и интеракције вирус–домаћин (инфекције) неопходно је разумети је из перспективе хемије и биотермодинамике. Овај рад представља емпиријске формуле, покретачку силу интеракција риновирус–домаћин, као и механистички модел интеракција вирус–домаћин на ћелијској мембрани и у цитоплазми. На основу описаних података, изнети су закључци о томе зашто је 50 % инфекција горњих дисајних путева узроковано риновирусима. По први пут су представљене вредности промена Гибсове енергије биосинтезе вирусних честица риновируса A2, B3 и C15, као и промена Гибсове енергије везивања риновируса A2, које су потребне за разумевање животног циклуса риновируса.

(Примљено 11. јануара, ревидирано 12. фебруара, прихваћено 8. априла 2026)

REFERENCES

1. S. Riedel, J. A. Hobden, S. Miller, S. A. Morse, T. A. Mietzner, B. Detrick, T. G. Mitchell, J. A. Sakanari, P. Hotez, R. Mejia, *Jawetz, Melnick and Adelberg's Medical Microbiology,* 28th ed., McGraw-Hill, New York, 2019 (ISBN-13: 978-1260012026)
2. D. Bouzid, O. Hadad, M. Bertine, N. Houhou-Fidouh, A. Mirand, X. Duval, V. Bunel, R. Borie, J. C. Lucet, D. Descamps, B. Visseaux, *Int. J. Infect. Dis.* **118** (2022) 144 (https://doi.org/10.1016/j.ijid.2022.02.055)
3. S. Ljubin-Sternak, T. Meštrović, *Viruses* **15** (2023) 825 (https://doi.org/10.3390/v15040825)
4. L. Andrup, K. A. Krogfelt, K. S. Hansen, A. M. Madsen, *Am. J. Infect. Control* **51** (2023) 938–957. (https://doi.org/10.1016/j.ajic.2022.12.005)
5. C. Esneau, N. Bartlett, Y. A. Bochkov, in *Rhinovirus infections*, N. Bartlett, P. Wark, D. Knight, Eds., Academic Press, Cambridge, MA, 2019, p. 1 (https://doi.org/10.1016/B978-0-12-816417-4.00001-9)
6. D. Gil-Cantero, C.P. Mata, L. Valiente, A. Rodríguez-Huete, A. Valbuena, R. Twarock, P. G. Stockley, M. G. Mateu, J. R. Castón, *Commun. Biol.* **7** (2024) 1501 (https://doi.org/10.1038/s42003-024-07213-2)
7. M. G. Rossmann, E. Arnold, J. W. Erickson, E. A. Frankenberger, J. P. Griffith, H. J. Hecht, J. E. Johnson, G. Kamer, M. Luo, A. G. Mosser, *Nature* **317** (1985) 145 (https://doi.org/10.1038/317145a0)
8. A. R. Alsayed, A. Abed, M. J. Al Shawabkeh, R. R. Aldarawish, M. Al-Shajlawi, N. Alabbas, *Pharm. Pract. (Granada)* **22** (2024) 1 (https://dialnet.unirioja.es/servlet/articulo?codigo=9414131)
9. S. Maitra, J. Rajak, A. Ghoshal, B. Roy, S. Ghosh, A. K. Mitra, A. Kumer, B. Dhara, *Health Sci. Rep.* **8** (2025) e70922 (https://doi.org/10.1002/hsr2.70922)
10. C. Esneau, N. E. Bryant, S. L. Johnston, N. W. Bartlett, *CMI Commun.* **2** (2025) 105081 (https://doi.org/10.1016/j.cmicom.2025.105081)
11. A. C. Palmenberg, J. E. Gern, *Methods Mol. Biol.* **1221** (2014) 1 (https://doi.org/10.1007/978-1-4939-1571-2_1)
12. W. Li, B. Yu, J. Zhou, Y. Wang, B. Xue, J. Pan, Y. Ran, X. Yang, X. Wang, F. Yang, H. Li, *Virol. J.* **18** (2021) 174 (https://doi.org/10.1186/s12985-021-01645-6)
13. M. E. Popović, V. Tadić, M. Popović, *Virology* **603** (2025) 110319 (https://doi.org/10.1016/j.virol.2024.110319)
14. M. E. Popović, M. Stevanović, V. Tadić, *Virology* **614** (2026) 110742 (https://doi.org/10.1016/j.virol.2025.110742)
15. S. L. Kerr, C. Mathew, R. Ghildyal, *Viruses* **13** (2021) 629 (https://doi.org/10.3390/v13040629)
16. X. Du, Y. Li, Y.-L. Xia, S.-M. Ai, J. Liang, P. Sang, X.-L. Ji, S.-Q. Liu, *Int. J. Mol. Sci.* **17** (2016) 144 (https://doi.org/10.3390/ijms17020144)
17. M. E. Popović, V. Tadić, D. Pei, *Therm. Sci.* (2025) (http://dx.doi.org/10.2298/TSCI250729209P)
18. S. S. Bappy, M. M. Haque Asim, M. M. Ahasan, A. Ahsan, S. Sultana, R. Khanam, A. Z. Shibly, Y. Kabir, *Rev. Med. Virol.* **34** (2024) e2505 (https://doi.org/10.1002/rmv.2505)
19. M. Özilgen, B. Yilmaz, *Int. J. Energy Res.* **45** (2021) 1157 (https://doi.org/10.1002/er.5883)
20. B. Şimşek, M. Özilgen, F. Ş. Utku, *Energy Storage* **4** (2022) e298 (https://doi.org/10.1002/est2.298)

21. M. J. Assael, G. C. Maitland, T. Maskow, U. von Stockar, W. A. Wakeham, S. Will, *Commonly Asked Questions in Thermodynamics,* 2nd ed., CRC Press, Boca Raton, FL, 2022 (https://doi.org/10.1201/9780429329524)
22. U. von Stockar, J. Liu, *Biochim. Biophys. Acta* **1412** (1999) 191 (https://doi.org/10.1016/s0005-2728(99)00065-1)
23. P. Buzón, S. Maity, P. Christodoulis, M. J. Wiertsema, S. Dunkelbarger, C. Kim, G. J. L. Wuite, A. Zlotnick, W. H. Roos, *Sci. Adv.* **7** (2021) eabg0811 (https://doi.org/10.1126/sciadv.abg0811)
24. M.E. Popović, M. Popović, G. Šekularac, M. Pantović Pavlović, *J. Serb. Chem. Soc.* **89** (2024) 807 (https://doi.org/10.2298/JSC240322051P)
25. E. W. Sayers, J. Beck, E. E. Bolton, J. R. Brister, J. Chan, R. Connor, M. Feldgarden, A. M. Fine, K. Funk, J. Hoffman, S. Kannan, C. Kelly, W. Klimke, S. Kim, S. Lathrop, A. Marchler-Bauer, T. D. Murphy, C. O'Sullivan, E. Schmieder, Y. Skripchenko, A. Stine, F. Thibaud-Nissen, J. Wang, J. Ye, E. Zellers, V. A. Schneider, K. D. Pruitt, *Nucleic Acids Res.* **53** (2025) D20 (https://doi.org/10.1093/nar/gkae979)
26. UniProt Consortium, *Nucleic Acids Res.* **53** (2025) D609 (https://doi.org/10.1093/nar/gkae1010)
27. C. Rankl, F. Kienberger, L. Wildling, J. Wruss, H. J. Gruber, D. Blaas, P. Hinterdorfer, *Proc. Natl. Acad. Sci. U.S.A.* **105** (2008) 17778 (https://doi.org/10.1073/pnas.0806451105)
28. J. M. Casasnovas, T. A. Springer, *J. Biol. Chem.* **270** (1995) 13216 (https://doi.org/10.1074/jbc.270.22.13216)
29. M. Popovic, *Comput. Biol. Chem.* **96** (2022) 107621 (https://doi.org/10.1016/j.compbiolchem.2022.107621)
30. M. E. Popović, G. M. Šekularac, V. M. Tadić, M. R. Pantović Pavlović, *Therm. Sci.* **28** (2024) 4737-4757 (https://doi.org/10.2298/TSCI240429213P)
31. S. A. Patel, L. E. Erickson, *Biotechnol. Bioeng.* **23** (1981) 2051 (https://doi.org/10.1002/bit.260230910)
32. E. H. Battley, *Thermochim. Acta* **309** (1998) 17 (https://doi.org/10.1016/S0040-6031(97)00357-2)
33. E. H. Battley, *Thermochim. Acta* **326** (1999) 7 (https://doi.org/10.1016/S0040-6031(98)00584-X)
34. E. H, Battley, J. R. Stone, *Thermochim. Acta* **349** (2000) 153 (https://doi.org/10.1016/S0040-6031(99)00509-2)
35. K. Annamalai, *Systems* **9** (2021) 54 (https://doi.org/10.3390/systems9030054)
36. M. E. Popović, M. Stevanović, M. Mihailović, *J. Serb. Chem. Soc.* **89** (2024) 305 (https://doi.org/10.2298/JSC240119019P)
37. Y. Demirel, *Nonequilibrium Thermodynamics: Transport and Rate Processes in Physical, Chemical and Biological Systems,* 3rd ed., Elsevier, Amsterdam, 2014 (ISBN: 9780444595812)
38. R. T. Balmer, *Modern Engineering Thermodynamics*, Academic Press, Cambridge, MA, 2010 (https://doi.org/10.1016/C2009-0-20199-1)
39. K. J. Hellingwerf, J. S. Lolkema, R. Otto, O. M. Neijssel, A. H. Stouthamer, W. Harder, K. van Dam, H. V. Westerhoff, *FEMS Microbiol. Lett.* **15** (1982) 7 (https://doi.org/10.1111/j.1574-6968.1982.tb00028.x)
40. H. V. Westerhoff, J. S. Lolkema, R. Otto, K. J. Hellingwerf, *Biochim. Biophys. Acta* **683** (1982) 181 (https://doi.org/10.1016/0304-4173(82)90001-5).

41. F. Fenner, P. A. Bachmann, E. P. J. Gibbs, F. A. Murphy, M. J. Studdert, D. O. White, in *Veterinary Virology*, Accademic Press, 1987, p. 3 (https://doi.org/10.1016/B978-0-12-253055-5.50005-0)
42. M. Y. Chen, S. S. Butler, W. Chen, J. Suh, *WIRE Nanomed. Nanobiotech.* **11** (2019) e1545 (https://doi.org/10.1002/wnan.1545)
43. S. Himbert, M. Chapman, D. Deamer, M. C. Rheinstädter, *Sci. Rep.* **6** (2016) 31285 (https://doi.org/10.1038/srep31285)
44. J. Lee, K. J. Schwarz, D. S. Kim, J. S. Moore, M. C. Jewett, *Nature Comm.* **11** (2020) 4304 (https://doi.org/10.1038/s41467-020-18001-x)
45. A. S. Spirin, L.P. Gavrilova, in *The Ribosome. Molecular Biology Biochemistry and Biophysics*, Vol. 4, Springer, Berlin, 1969 (https://doi.org/10.1007/978-3-642-88446-7_8)
46. R. F. Garmann, A. M. Goldfain, V. N. Manoharan, *PNAS* **116** (2019) 22485 (https://doi.org/10.1073/pnas.1909223116)
47. R. D. Cadena-Nava, M. Comas-Garcia, R. F. Garmann, A. L. Rao, C. M. Knobler, W. M. Gelbart, *J. Virol.* **86** (2012) 3318 (https://doi.org/10.1128/JVI.06566-11)
48. U. Von Stockar, in *Biothermodynamics: The Role of Thermodynamics in Biochemical Engineering*, U. von Stockar, Ed., EPFL Press, Lausanne, 2013, p. 399 (https://doi.org/10.1201/b15428)
49. M. Ozilgen, E. Sorguven Oner, *Biothermodynamics: Principles and Applications*, 1st ed., CRC Press, Boca Raton, FL, 2016 (https://doi.org/10.1201/9781315374147)
50. M. Popovic, *Heliyon* **5** (2019) e01950 (https://doi.org/10.1016/j.heliyon.2019.e01950)
51. WHO, *WHO COVID-19 dashboard – Summary [Online] World Health Organization*, 2026, (https://data.who.int/dashboards/covid19/summary?n=c) (Accessed on March 25, 2026)
52. *Next Strain Genomic epidemiology of SARS-CoV-2 with subsampling focused globally over the past 6 months [Online]*, 2026 (https://nextstrain.org/ncov/open/global/6m) (Accessed on March 25, 2026).

Journal of the Serbian Chemical Society
JSCS-info@shd.org.rs • www.shd.org.rs/JSCS
J. Serb. Chem. Soc. *91* (6) 573–588 (2026)
JSCS–5511
Original scientific paper
Published 2 July, 2026

Energetic networks of lone pair–π interactions in phycobiliprotein interfaces: Structural organization, geometry and cooperative stabilization

LUKA M. BREBERINA[1], MARIO V. ZLATOVIĆ[2], SRĐAN Đ. STOJANOVIĆ[3] and MILAN R. NIKOLIĆ[1]*

[1]University of Belgrade – Faculty of Chemistry, Department of Biochemistry, Belgrade, Serbia, [2]University of Belgrade – Faculty of Chemistry, Department of Organic Chemistry, Belgrade, Serbia and [3]University of Belgrade, Institute of Chemistry, Technology and Metallurgy – National Institute of the Republic of Serbia, Department of Chemistry, Belgrade, Serbia

(Received 3 February, revised 13 March, accepted 30 March 2026)

Abstract: Lone pair–π interactions represent an underexplored class of noncovalent forces in protein architecture, despite their fundamental electronic significance. Here, we present a comprehensive computational and bioinformatics analysis of lone pair–π interactions at phycobiliprotein interfaces based on 20 high-resolution X-ray crystal structures. Using defined geometric criteria and *ab initio* quantum-chemical calculations at the LMP2/cc-pVTZ++ level on reduced molecular models, we systematically characterized their distribution, geometry, topology and energetic contributions. We identified 2,245 lone pair–π interactions, revealing a highly non-random and chemically selective interaction landscape dominated by oxygen-based lone pair donors and aromatic π acceptors, particularly Tyr and Phe. Geometric analysis showed strong distance and angular preferences, consistent with directional donor–acceptor orbital interactions rather than nonspecific packing effects. Energy calculations revealed a structured interaction potential surface, with stabilizing energies clustering in the −0.1 to −5.0 kJ mol^{-1} range within defined geometric domains. Network analysis further demonstrated that more than half of the interactions participate in cooperative, furcated lone pair–π motifs, generating interfacial stabilization through multivalent interaction networks. Collectively, these results establish lone pair–π interactions as geometry-encoded, energetically selective and cooperatively organized stabilizing elements that contribute to interfacial specificity, structural precision and quaternary structure stability in phycobiliprotein assemblies.

Keywords: phycobiliproteins; lone pair–π; interfaces, interactions, *in silico* studies.

* Corresponding author. E-mail: mnikolic@chem.bg.ac.rs
https://doi.org/10.2298/JSC260230017B

INTRODUCTION

Noncovalent interactions provide the fundamental energetic framework that governs protein folding, molecular recognition and the formation of stable protein–protein interfaces in supramolecular assemblies. Classical interaction types such as hydrogen bonds, salt bridges, hydrophobic interactions and π–π stacking have long been recognized as central stabilizing forces in protein structure and protein–protein interfaces.[1,2] However, advances in quantum chemistry and structural bioinformatics have shown that protein stability and specificity are also influenced by a diverse range of weak but highly directional electronic interactions, including n→π*, cation–π, anion–π and lone pair–π interactions.[3–5] Although individually modest in energy, these interactions can have significant structural effects through cooperativity, spatial organization, and network formation.

Lone pair–π interactions arise from the interaction between a heteroatom lone pair orbital (n) and an aromatic or conjugated π system. These interactions involve electrostatic attraction, dispersion forces, and partial orbital donation from the lone pair into antibonding π* orbitals.[5–7] Unlike n→π* interactions, which involve carbonyl antibonding orbitals, lone pair–π interactions involve aromatic π-systems and therefore display distinct geometric preferences and interaction topologies. Quantum-mechanical studies have shown that these interactions are highly geometry-dependent, directional and energetically structured, forming defined stabilization minima in configuration space rather than diffuse, nonspecific attraction.[8,9] Lone pair–π interactions can be systematically classified by the identity of the lone pair donor atom (O, N, S, halogen), the electronic nature of the interacting π-system (aromatic hydrocarbons, heteroaromatics, conjugated systems, nucleobases) and the biological context in which they occur (protein–ligand binding, protein–protein interfaces, protein–nucleic acid recognition and water-mediated networks).[9–11] This multidimensional classification framework enables structured identification, annotation, and functional interpretation of lone pair–π interactions across biomolecular systems (Fig. 1).

Despite their well-established physical basis, lone pair–π interactions remain systematically underexplored in biological macromolecules, particularly at protein–protein interfaces.[2,12,13] Most structural analyses of protein complexes focus on hydrogen bonding, hydrophobic packing and electrostatic complementarity, while orbital-driven interactions are rarely included in standard interaction classifications.[14,15] Consequently, the contribution of lone pair–π interactions to interface organization, specificity and stability has not been quantitatively assessed at the proteome or structural family level.

Phycobiliproteins are an ideal model system for studying such interactions. These highly ordered, oligomeric light-harvesting proteins form stable supramolecular assemblies with dense packing, extensive interfacial contact surfaces and precise chromophore–protein and protein–protein organization. Their quaternary

structures depend on finely balanced noncovalent interaction networks that provide both structural stability and functional flexibility.[16] Although hydrogen bonds, salt bridges and hydrophobic interactions in phycobiliprotein assemblies have been extensively studied, the role of weak electronic interactions, such as lone pair–π interactions, remains largely unexplored.

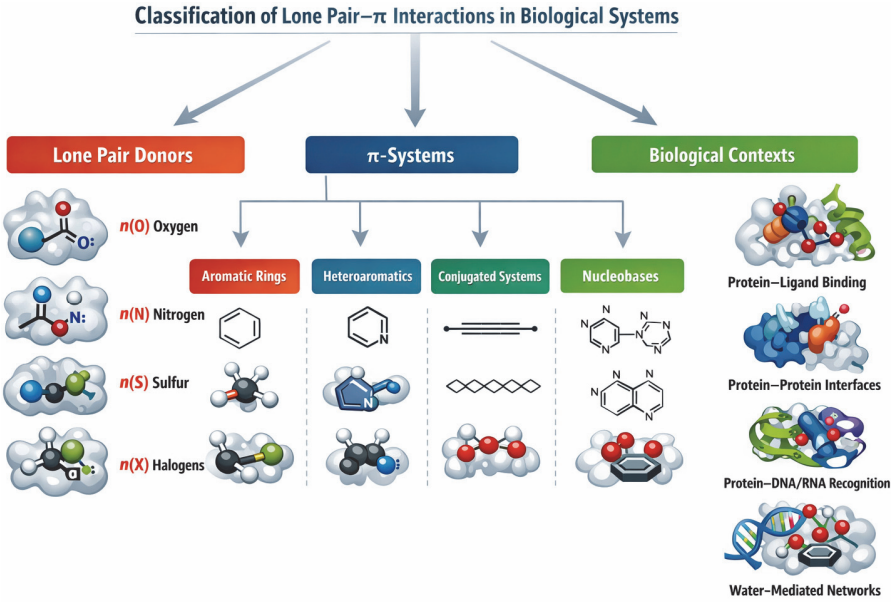

Fig. 1. Schematic representation of the multidimensional classification framework for lone pair–π interactions in biological systems. Lone pair–π interactions are organized along three orthogonal dimensions: 1) identity of the lone pair donor atom (oxygen, nitrogen, sulfur, halogens); 2) electronic nature of the interacting π-system (aromatic hydrocarbons, heteroaromatic systems, conjugated unsaturated systems, nucleobases) and 3) biological context (protein–ligand binding, protein–protein interfaces, protein–nucleic acid recognition, water-mediated interaction networks). This integrated classification highlights the structural diversity, mechanistic variability and functional relevance of lone pair–π interactions in biomolecular systems.

In this study, we present a comprehensive structural, geometric and energetic analysis of lone pair–π interactions at phycobiliprotein interfaces. Using a curated dataset of high-resolution X-ray crystal structures combined with ab initio quantum-chemical calculations, we characterize their distribution, preferred geometries and energetic contributions. Beyond pairwise interactions, we introduce a network-based perspective showing that lone pair–π contacts frequently form multivalent motifs that contribute to the cooperative structural organization of protein interfaces.

By integrating structural bioinformatics, quantum chemistry and energy landscape analysis, this study expands the current conceptual framework for protein

interface stabilization and highlights lone pair–π interactions as an important yet previously underappreciated component of supramolecular protein organization. The aim of this study was to systematically characterize the structural organization, geometry and energetic contributions of lone pair–π interactions at phycobiliprotein interfaces.

EXPERIMENTAL

Dataset

For this study, we used the PDB, accessed on November 10, 2025, which listed 247,081 resolved structures.[17] The selection criteria for including phycobiliproteins in the dataset were as follows: a) structures of proteins containing the phycobiliprotein alpha or beta subunit domain (SCOP Classification, version 1.75)[18] were included; b) theoretical models and NMR structures were excluded due to difficulties in assessing their accuracy compared to X-ray diffraction studies. Only crystal structures with a resolution of 2.0 Å or better and a crystallographic *R*-factor of 25.0 % or lower were accepted; c) only representatives with at least 30 % sequence identity were included in the analyses.

After assembling the dataset, several structures containing ligands and mutant amino acids were excluded, leaving 20 phycobiliproteins in the dataset used for our bioinformatics analysis. Hydrogen atoms were added and optimized as needed using the program REDUCE[19] with its default settings. This software adds hydrogen atoms to macromolecule (protein and DNA) structures in standardized geometry, optimizing their orientations for OH, SH, NH_3^+, Met methyls, Asn and Gln side-chain amides and His rings. REDUCE selects the optimal hydrogen positions by choosing the overall best score from all possible combinations, considering individual scores assigned to each residue and groups containing movable protons partitioned into closed sets of local interacting networks.

The PDB IDs of all selected phycobiliprotein structures were as follows: 1all (allophycocyanin (APC) from *Spirulina platensis*), 1b33 (APC from *Mastigocladus laminosus*), 1cpc (C-phycocyanin (C-PC) from *Microchaete diplosiphon*), 1f99 (R-PC from *Polysiphonia urceolata*), 1gh0 (C-PC from *Arthrospira platensis*), 1jbo (C-PC from *Synechococcus elongatus*), 1kn1 (APC from *Neopyropia yezoensis*), 1phn (PC from *Cyanidium caldarium*), 2bv8 (PC from *Nostoc sp.* R76DM), 2vjt (APC from *Gloeobacter violaceus*), 2vml (PC from *Gloeobacter violaceus*), 3dbj (APC from *Thermosynechococcus vulcanus*), 3o18 (C-PC from *Themosynechococcus vulcanus*), 4f0u (APC from *Synechococcus elongatus* PCC 7942), 4l1e (C-PC from *Leptolyngbya sp.* N62DM), 4lm6 (PC612 from *Hemiselmis virescens* M1635), 4lms (PC577 from *Hemiselmis pacifica* CCMP 706), 4po5 (APC from *Synechocystis* PCC 6803), 4rmp (APC from *Phormidium sp.* A09DM) and 4yjj (PC from *Phormidium rubidum*).

Lone pair–π interaction analysis

Protein structures containing various types of lone pair–π interactions were analyzed using Discovery Studio Visualizer 2025[20] with specific criteria and geometric feature settings. Lone pair–π interactions occur between a lone pair and a π-ring if the following criteria are met (Fig. 2): 1) hydrogen bond acceptor atoms are considered as long as they do not already participate in other atom–π ring interactions; 2) the distance between the acceptor and the ring centroid is within the π–lone pair (max dist) cutoff (7.0 Å); 3) the angle between the acceptor centroid vector and the normal to the ring plane is less than the π–lone pair angle (90°). Because lone pair orbitals cannot be directly observed in X-ray crystal structures, their orientation relative to the aromatic π-system must be approximated using geometric criteria. In this study, the donor

atom–centroid distance and the angle between the donor–centroid vector and the normal to the aromatic ring plane were used as geometric proxies to approximate the preferred directionality of the lone pair toward the π-electron cloud.

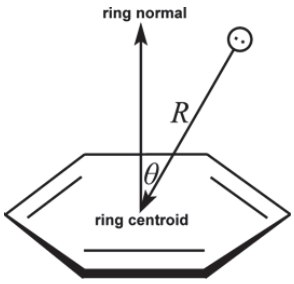

Fig. 2. Parameters for lone pair–π interactions: R – the distance between the lone pair and the centroid; θ – the angle between the lone pair–centroid vector and the normal to the ring plane.

Computation of lone pair–π interaction energy

To perform *ab initio* calculations to determine the energies of lone pair–π pairs at the desired level of theory, with adequate accuracy and within a satisfactory time frame, we used structurally reduced model systems.[21,22] Phenylalanine was simplified to methylbenzene (**1**), histidine to 5-methyl-1*H*-imidazole (**2**) and tryptophan and tyrosine were reduced to 3-methyl--1*H*-indole (**3**) and 4-methylphenol (**4**), respectively (Fig. 3).

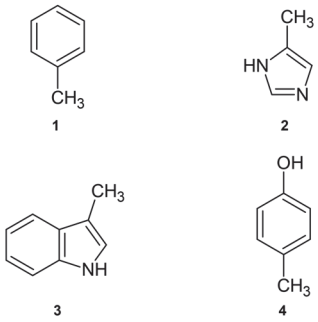

Fig. 3. Structurally simplified structures used for lone pair–π interaction energy calculations: **1** instead of Phe; **2** instead of His; **3** instead of Trp; **4** instead of Tyr.

Ab initio calculations were performed in a vacuum using Jaguar from Schrödinger Suite 2018-1,[23] employing the LMP2 method with the triple zeta Dunning correlation-consistent basis set[24] and ++ diffuse functions.[25] The LMP2 method, used to study lone pair–π interactions, was significantly faster than the MP2 method. However, the calculated interaction energies and equilibrium distances from both methods are almost identical.[26] Several authors have found that LMP2 is an excellent method for calculating protein interaction energies.[27-29]

Geometries of interacting structures were optimized using the LMP2/cc-pVTZ(-f)++ level of theory and their single-point energies were calculated at the LMP2/cc-pVTZ++ level. In practice, the optimized model fragments were first generated independently at the LMP2/cc--pVTZ(−f)++ level. The optimized fragments were then spatially aligned with the corresponding residues in the crystal structures by superimposing the heavy atoms of the model systems onto the atomic coordinates extracted from the protein structures. This procedure preserves the experimentally observed relative orientation of the interacting groups while using the optimized model geometries for reliable quantum-chemical energy evaluation. Frequency calculations were performed for all optimized model systems at the same level of theory to verify that the

structures correspond to true minima on the potential energy surface. All optimized structures showed no imaginary frequencies.

Interaction energies were evaluated using a large correlation-consistent triple-ζ basis set with diffuse functions (cc-pVTZ++). Although basis set superposition error (*BSSE*) can influence very weak interactions, using an extended basis set substantially reduces this effect. Consequently, *BSSE* is expected to introduce only a small systematic shift in absolute energies without affecting the qualitative trends observed across the interaction dataset.

The lone pair–π interaction energies in dimers (lone pair–π pairs) were calculated as the difference between the energy of the complex and the sum of the energies of the monomers in their optimized geometries.

The nature of the aromatic π system also influences the interaction energy. Phenylalanine and tyrosine represent the dominant π-acceptors in the analysed dataset. While both provide similar aromatic π-surfaces, the phenolic group of tyrosine introduces additional polarization and electrostatic effects that may slightly enhance lone pair–π stabilization compared with purely hydrocarbon aromatic systems such as phenylalanine. These electronic differences contribute to the observed distribution of interaction geometries and energies.

From the complete set of identified lone pair–π contacts, representative model dimers were constructed for quantum-chemical interaction energy calculations. The selected model systems preserve the experimentally observed geometry of the interacting fragments while allowing accurate evaluation of the interaction energies. Cartesian coordinates of the representative optimized dimers are provided in the Supplementary material to this paper.

RESULTS AND DISCUSSION

This manuscript examines the role of lone pair–π interactions at phycobiliprotein interfaces and their environmental preferences. We performed a computational analysis of 20 X-ray crystallographic structures of phycobiliproteins and summarized lone pair–π interactions to better understand the high stability of intrinsic phycobiliprotein oligomers. Furthermore, we analysed the relative preference of lone pair–π interacting amino acids at interfaces, interaction geometries and energetic contributions of lone pair–π interactions.

Distribution of lone pair–π interactions

Using the geometrical criteria defined in the Experimental, we analysed the frequency of aromatic amino acid residues involved in lone pair–π interactions. The results are shown in Table I. There are 2,245 lone pair–π interactions in phycobiliprotein interfaces in our dataset, with an average of 112 interactions per protein. This unexpectedly high interaction density indicates that lone pair–π contacts are not rare structural anomalies but are a systematic component of the noncovalent interaction landscape at phycobiliprotein interfaces.

The distribution of residues involved in lone pair–π interactions within phycobiliprotein interfaces is highly non-random and chemically selective, reflecting fundamental electronic and geometric principles that govern donor–acceptor interactions between lone pair orbitals and aromatic π-electron systems. These interactions result from a combination of electrostatic attraction, orbital polarization and

dispersion forces and are conceptually related to donor–acceptor frameworks described for n→π* interactions, while remaining mechanistically distinct because they involve aromatic π-systems rather than carbonyl antibonding orbitals.[2,5,7,30] The data reveal a pronounced donor–acceptor asymmetry, with electron-rich, oxygen-containing groups acting primarily as lone pair donors and aromatic residues serving as the main π-acceptors.

TABLE I. Frequency of occurrence of lone pair–π interaction-forming residues at phycobiliprotein interfaces

Residue	Lone pair		π	
	Number[a]	Occurrence[b], %	Number	Occurrence, %
Backbone	1197	53.3	–	–
Side-chain				
Asn	45	2.1	–	–
Asp	434	19.3	–	–
Gln	32	1.4	–	–
Glu	54	2.4	–	–
His	10	0.4	–	–
Met	37	1.7	–	–
Ser	113	5.0	–	–
Thr	176	7.8	–	–
Tyr	147	6.6	–	–
His	–	–	18	0.8
Phe	–	–	915	40.8
Trp	–	–	16	0.7
Tyr	–	–	1296	57.7
Total	2245	100	2245	100

[a]The number of times a particular amino acid occurs in an appropriate interaction; [b]the percentage of times the amino acid occurs in an appropriate interaction

Backbone atoms are the primary source of lone pair donors (53.3 %), highlighting the central role of peptide carbonyl oxygen atoms as universal and geometrically accessible lone pair contributors. Carbonyl oxygens are well-established participants in donor–acceptor orbital interactions in biological systems and are highly effective lone pair donors because of their strong electron density and favorable orbital orientation.[5,11] Their prevalence at protein interfaces underscores that lone pair–π interactions are intrinsic to protein architecture rather than dependent solely on side-chain chemistry.

Among side-chain contributors, oxygen-containing residues dominate the lone pair donor landscape, with Asp (19.3 %), Thr (7.8 %), Ser (5.0 %), Tyr (6.6 %), Glu (2.4 %) and Asn (2.1 %) accounting for most interactions. This distribution reflects the high electron density and favorable orbital orientation of oxygen lone pairs in carboxylate, carbonyl and hydroxyl groups, which are optimal for lone pair–π coupling.[8,31] Carboxylate-containing residues (Asp, Glu) are particularly effective

donors due to their delocalized negative charge and strong n-donor character, enabling robust electrostatic and polarization-driven interactions with π-systems. Hydroxyl-bearing residues (Ser, Thr, Tyr) provide geometrically flexible lone pairs that can participate in directional lone pair–π interactions, often forming cooperative networks with hydrogen bonds and enhancing interface stability.[5,31] In this work, the term "cooperative" is used primarily in a structural and qualitative sense, referring to the spatial clustering of multiple lone pair–π contacts within protein interfaces. The analysis does not explicitly quantify energetic cooperativity through many-body energy decomposition but instead highlights the structural organization of interaction networks that may collectively contribute to stabilization.

In contrast, sulfur- and nitrogen-containing side chains contribute minimally to lone pair donation (Met 1.7 %, His 0.4 %), reflecting the lower energetic favorability, reduced directionality and less optimal orbital overlap of sulfur and imidazole lone pairs in biological lone pair–π systems.[8] This selectivity indicates that lone pair–π interactions in proteins are chemically biased toward oxygen-based donors rather than representing a general lone pair phenomenon.

On the π-acceptor side, aromatic residues dominate the interaction landscape, with Tyr (57.7 %) and Phe (40.8 %) accounting for nearly all π-contributions. Aromatic rings are well-established π-electron acceptors in noncovalent interactions because of their delocalized electron clouds, quadrupole moments, and anisotropic electrostatic potentials.[4,7] Tyrosine plays a particularly central role, as its phenolic ring provides an efficient π-acceptor surface, while its hydroxyl group can serve as a lone pair donor in alternative geometries, enabling bidirectional lone pair–π connectivity and network formation within interfacial regions.[8,31]

The low contribution of tryptophan (0.7 %), despite its extended π-system, likely reflects steric constraints and structural burial of indole rings, which limit their accessibility for lone pair–π engagement at protein–protein interfaces. Similarly, histidine contributes minimally as a π-acceptor because the heteroaromatic nature of the imidazole ring alters its π-electron density distribution and electrostatic surface compared to phenyl systems.[4]

We have also examined multiple lone pair–π interactions at phycobiliprotein interfaces. The analysis showed that about 56 % of the dataset's lone pair–π interactions participate in multiple interactions. The presence of furcated lone pair networks at phycobiliprotein interfaces indicates that lone pair donors – primarily backbone carbonyl oxygens and polar side-chain oxygen atoms – and aromatic π--systems do not form isolated pairwise contacts, but instead create cooperative interaction clusters in which a single donor can engage multiple π-centers or a single π-system can accept multiple lone pair interactions. These topologies are consistent with cooperative donor–acceptor polarization and charge-redistribution models, where local electronic organization promotes network-like stabilization rather than discrete binary interactions.[3,32,33] Functionally, these furcated lone pair networks

likely contribute to interfacial robustness and dynamic stability, enabling stabilization through distributed weak interactions rather than reliance on a small number of strong directional bonds.[5,34]

An illustrative example of multiple lone pair–π interactions is shown in Fig. 4. The interaction pattern observed in allophycocyanin from *Spirulina platensis* represents a structurally and electronically coherent case of furcated (multiple) lone pair–π interactions, in which a single residue acts as a multivalent donor to multiple aromatic π-acceptors. The carboxylate group of A:Asp13 simultaneously engages both oxygen atoms (OD1 and OD2) in lone pair–π interactions with B:Tyr94 and B:Tyr97, generating a fourfold donor–acceptor network (OD1–Tyr94, OD1–Tyr97, OD2–Tyr94, OD2–Tyr97). This architecture reflects a bifurcated donor/multi-acceptor topology, where the delocalized lone pair electron density of the carboxylate group is distributed toward multiple π-systems rather than forming a single localized interaction. At the electronic level, this motif is consistent with n→π* donation and electrostatically driven lone pair–π coupling, in which electron density from oxygen lone pair orbitals is transferred into low-lying antibonding π*-orbitals of adjacent aromatic systems in a geometry-dependent and directional manner.[5,8]

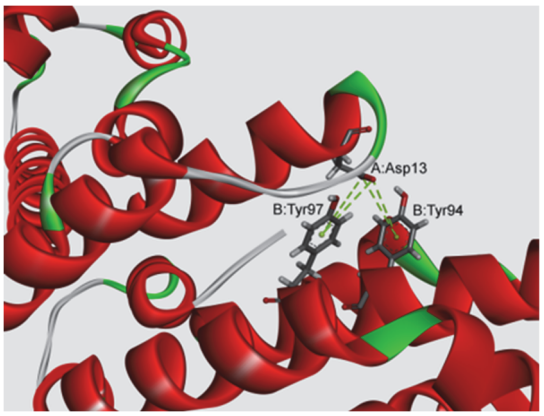

Fig. 4. Furcated (multiple) lone pair–π interaction network in allophycocyanin from *Spirulina platensis* (PDB ID: 1all). The carboxylate group of A:Asp13 simultaneously engages both oxygen atoms (OD1 and OD2) in lone pair–π interactions with two aromatic residues, B:Tyr94 and B:Tyr97, forming a fourfold interaction network: 1) A:Asp13:OD1–B:Tyr94, 2) A:Asp13:OD1–B:Tyr97, 3) A:Asp13:OD2–B:Tyr94 and 4) A:Asp13:OD2–B:Tyr97. This furcated lone pair–π motif reflects cooperative n→π* donation and multivalent electrostatic–orbital coupling, generating a stabilizing interaction network across the protein interface.[5,8]

The simultaneous involvement of both OD1 and OD2 atoms indicates that the carboxylate group acts as a cooperative donor unit, enabling charge delocalization

and interaction redundancy – a phenomenon analogous to cooperativity in hydrogen-bond networks but governed by orbital overlap and π-electron polarization rather than proton transfer.[35]

Lone pair–π interactions in protein environments rarely occur in isolation. In many cases, additional noncovalent interactions, such as π–π stacking, CH–π contacts, and general dispersion interactions, also contribute to the stabilization of the observed structural motifs. Therefore, the lone pair–π contacts identified here should be considered components of a broader network of weak interactions that collectively contribute to interface stability. Such furcated lone pair–π networks transform intrinsically weak individual noncovalent interactions into collectively stabilizing motifs, enhancing interfacial robustness, restricting local conformational flexibility and promoting precise aromatic alignment across protein–protein interfaces.[5,36] In phycobiliprotein assemblies, this multivalent lone pair–π architecture likely contributes to quaternary structure stabilization and electronic preorganization of the interface, supporting long-range structural coherence and highlighting lone pair–π furcation as a previously underappreciated but mechanistically significant stabilizing principle in protein complexes.

Interaction geometries of lone pair–π interactions

The frequency distribution of the distance and angle parameters for lone pair–π interaction pairs is analysed (Fig. 5).

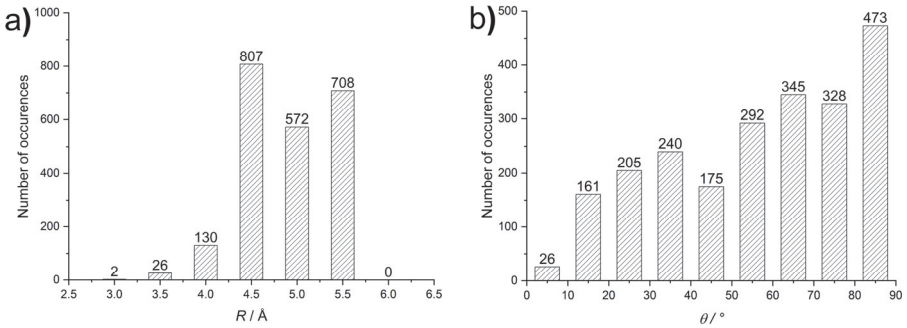

Fig. 5. Interaction geometries of lone pair–π interactions in phycobiliproteins: a) R distance distribution, b) θ angle distribution.

The R-distance distribution (Fig. 5a) shows a strong clustering of lone pair–π interactions in the 4.0–5.5 Å range, with clear maxima at 4.5 (807 occurrences) and 5.5 Å (708 occurrences) and a substantial population at 5.0 Å (572 occurrences). In contrast, very short distances (<3.5 Å) are extremely rare and no interactions are observed beyond approximately 6.0 Å. This distance range is fully consistent with the established geometric window for stabilizing lone pair–π and n→π* interactions, which typically occur at donor–acceptor separations of approx-

imately 3.0–5.5 Å, depending on the electronic nature of the donor atom and the π-system involved.[5,35] Importantly, the dominance of mid-range distances suggests that these interactions in phycobiliprotein interfaces are not random contacts but electronically optimized noncovalent interactions, where electrostatic attraction and orbital overlap (lone pair→π* donation) operate in a balanced regime that maximizes stabilization while avoiding steric repulsion.[8,37]

The θ-angle distribution (Fig. 5b) further supports a directional and anisotropic interaction pattern, with a progressive enrichment toward larger angles and a pronounced maximum in the 80–90° bin (473 occurrences). This angular preference is highly characteristic of lone pair–π geometries, where the lone pair orbital approaches the aromatic π-cloud approximately perpendicular to the ring plane, optimizing electrostatic complementarity and orbital alignment (lone pair orbital→π* orbital interaction).[4,5] Such near-orthogonal approach geometries are inconsistent with purely nonspecific van der Waals contacts and instead reflect orbital-controlled directionality, a hallmark of n→π* and lone pair–π interactions in biological systems.[5,8]

From a structural biology perspective, the combined distance–angle signature (R: 4.0–5.5 Å, θ: 60–90°) indicates that lone pair–π interactions in phycobiliprotein interfaces act as true structure-directing noncovalent interactions, comparable in geometric specificity to hydrogen bonds and π–π stacking, but governed by different electronic principles. Their enrichment at protein–protein interfaces supports the view that lone pair–π interactions contribute to interfacial complementarity, local stabilization, and interaction network formation, rather than representing incidental packing contacts.[5,8] The large number of interactions identified across independent crystal structures further supports the conclusion that lone pair–π contacts represent a recurrent, structurally encoded interaction type rather than incidental geometric contacts.

Taken together, these distributions demonstrate that lone pair–π interactions in phycobiliproteins are geometrically selective, directional and electronically driven, supporting their classification as functionally relevant stabilizing interactions within supramolecular protein assemblies rather than as passive geometric coincidences.

Energetic contribution of lone pair–π interactions

Quantifying noncovalent interactions is essential for a rational approach to biological systems, including protein structure and function, antibody binding, drug design and the development of supramolecular chemistry.[38] Therefore, the energetic contributions of residues involved in lone pair–π interactions were calculated using *ab initio* methods at the LMP2 level. The results for lone pair–π interacting pairs are shown in Fig. 6. To avoid calculating more than 2,000 interactions, we carefully selected 100 structures that represent nearly all of the interactions found.

Fig. 6 shows the three-dimensional energy–geometry landscape of lone pair–π interactions at phycobiliprotein interfaces, revealing a structured dependence of interaction energy on donor–π distance (R) and approach angle (θ). The three-dimensional energy–geometry landscape demonstrates that lone pair–π interactions at phycobiliprotein interfaces are governed by a well-defined energetic potential surface, rather than by a broad distribution of weak, nonspecific contacts. Energetically favorable interactions cluster within a narrow geometric domain defined by short donor–π distances (R: 3.5–5.5 Å) and intermediate approach angles (θ: 40––70°), corresponding to distinct local energy minima in the interaction landscape. The concentration of interaction energies in the range of approximately −0.1 to −5.0 kJ mol^{-1} indicates that lone pair–π contacts provide measurable and systematic stabilization, forming a reproducible energetic signature rather than stochastic low-energy fluctuations. This pattern reflects a structured stabilization mechanism, consistent with quantum-mechanical descriptions of lone pair–π and n→π* interactions, which predict energy minimization through optimized orbital overlap and electrostatic complementarity rather than purely distance-dependent Coulombic attraction.[5,39]

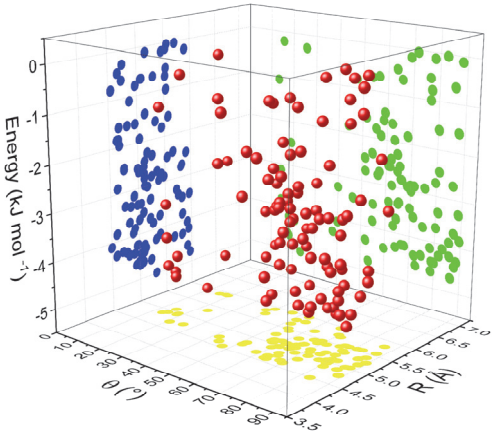

Fig. 6. 3D scatter plot from the energy analysis showing the distribution of energies depending on distance and angle for lone pair–π interacting pairs. A red circle denotes an energy that is an accepted lone pair–π interaction; yellow, green and blue circles denote *XY*, *XZ* and *YZ* projections, respectively.

Importantly, the energy distribution is highly anisotropic, showing strong stabilization only within restricted θ–R regions, indicating that lone pair–π interactions are governed by directional energetic constraints. The angular dependence of stabilization energy demonstrates that these interactions have a significant orbital delocalization component, where electron density transfer from heteroatom lone pairs into aromatic π*-orbitals generates a directional energy minimum (n→π* stabilization), rather than an isotropic, dispersion-dominated attraction. This creates a discrete energetic well in configuration space, characteristic of weak but electronically structured noncovalent interactions.[5,8]

The systematic increase in interaction energy (reduced stabilization) at longer distances ($R > 6.0$ Å) and at extreme angular values ($\theta < 30°$ or $\theta > 80°$) defines a steep energetic gradient away from the optimal stabilization zone, indicating rapid energetic decay outside the favorable interaction basin. This steep energy drop-off confirms the short-range energetic nature of lone pair–π interactions and rules out interpretations based on long-range electrostatics or diffuse van der Waals stabilization. Energy decomposition models also predict that lone pair–π stabilization results from localized orbital interactions and therefore decays sharply with geometric displacement.[6,9]

Within phycobiliprotein interfaces, this energy landscape suggests that lone pair–π interactions serve as energetically selective stabilizing elements, contributing not through large individual interaction energies but through energetic cooperativity and accumulation. Multiple lone pair–π contacts, organized within optimal energetic domains, can collectively generate distributed stabilization energy, forming interfacial energy networks that enhance interface robustness, reduce local conformational entropy and increase energetic barriers to dissociation. Thus, lone pair–π interactions act as fine-scale energetic modulators of protein–protein interfaces, refining stability and specificity through the spatial organization of multiple weak but energetically optimized interactions, directly analogous to cooperative hydrogen-bond and dispersion networks in structured protein interfaces.[5,8]

CONCLUSION

This study provides a systematic structural, geometric and energetic characterization of lone pair–π interactions in phycobiliprotein interfaces, establishing them as functionally relevant noncovalent interactions rather than incidental packing contacts. Through large-scale structural analysis and ab initio quantum-chemical energy calculations, we show that lone pair–π interactions in phycobiliproteins are chemically selective, geometrically constrained and energetically structured, forming reproducible stabilization patterns across protein–protein interfaces.

Our results show that lone pair–π interactions are primarily driven by oxygen-based lone pair donors and aromatic π acceptors, with specific distance and angular preferences that reflect directional donor–acceptor orbital coupling rather than diffuse electrostatic attraction. The computed energy landscape reveals discrete stabilization minima, indicating that lone pair–π interactions have intrinsic energetic organization, despite their individually modest interaction energies. Notably, the frequent occurrence of furcated and structurally cooperative lone pair–π motifs demonstrates that these interactions function as interfacial energy networks, where multiple weak contacts collectively generate distributed interaction networks that enhance interface robustness, reduce conformational entropy, and increase energetic barriers to dissociation.

In phycobiliprotein assemblies, this cooperative architecture positions lone pair–π interactions as fine-scale energetic modulators that complement hydrogen bonds, salt bridges, and hydrophobic interactions by providing geometric precision and electronic preorganization at protein–protein interfaces. More broadly, our findings support a conceptual shift from viewing lone pair–π interactions as isolated weak contacts to recognizing them as organized, network-forming stabilizing elements that contribute to supramolecular protein structure and stability. The identification of over two thousand lone pair–π interactions in a relatively small dataset of phycobiliprotein structures highlights that these interactions are a widespread and previously underappreciated stabilizing component of protein–protein interfaces.

These results expand the current understanding of noncovalent interaction networks in proteins and highlight lone pair–π interactions as a previously underappreciated stabilizing principle in biological assemblies. The energetic network model presented here provides a new framework for interpreting weak orbital interactions at protein interfaces and offers a foundation for future studies of their roles in protein folding, oligomerization, molecular recognition and biomolecular self-assembly.

SUPPLEMENTARY MATERIAL

Additional data and information are available electronically at the pages of journal website: https://www.shd-pub.org.rs/index.php/JSCS/article/view/13760, or from the corresponding author on request.

Acknowledgement. This research has been financially supported by the Ministry of Science, Technological Development and Innovation of the Republic of Serbia (Contracts No.: 451-03-136/2026-03/200026 and 451-03-33/2026-03/ 200168).

ИЗВОД

ЕНЕРГЕТСКЕ МРЕЖЕ СЛОБОДНИ ПАР–π ИНТЕРАКЦИЈА У МОЛЕКУЛСКИМ ПРОСТОРИМА ФИКОБИЛИПРОТЕИНА: СТРУКТУРНА ОРГАНИЗАЦИЈА, ГЕОМЕТРИЈА И КООПЕРАТИВНА СТАБИЛИЗАЦИЈА

ЛУКА М. БРЕБЕРИНА[1], МАРИО В. ЗЛАТОВИЋ[2], СРЂАН Ђ. СТОЈАНОВИЋ[3] и МИЛАН Р. НИКОЛИЋ[1]

[1]Универзитет у Београду, Хемијски факултет, Катедра за биохемију, Београд, [2]Универзитет у Београду, Хемијски факултет, Катедра за органску хемију, Београд и [3]Универзитет у Београду, Институт за хемију, технологију и металургију, Центар за хемију, Институт од националног значаја за Републику Србију, Београд

Слободни пар (*lone pair*)–π интеракције представљају недовољно истражену класу нековалентних сила у архитектури протеина, упркос њиховом фундаменталном електронском значају. У овом раду представљамо свеобухватну рачунарску и биоинформатичку анализу слободни пар–π интеракција у молекулским просторима фикобилипротеина, засновану на 20 рендгенских кристалографских структура високе резолуције. Применом дефинисаних геометријских критеријума и *ab initio* квантно-хемијских прорачуна на LMP2/cc-pVTZ++ нивоу теорије на редукованим молекулским моделима, систематски

смо окарактерисали њихову дистрибуцију, геометрију, топологију и енергетске доприносе. Идентификовано је укупно 2,245 слободни пар–π интеракција, што указује на изразито насумичан и хемијски селективан интеракциони пејзаж, којим доминирају донори слободних електронских парова кисеоника и ароматски π-акцептори, нарочито тирозин и фенилаланин. Геометријска анализа показала је изражене преференције у погледу дистанце и угла, у складу са усмереним донор–акцептор орбиталним интеракцијама, а не са неспецифичним ефектима паковања. Енергетски прорачуни открили су структурисану интеракциону потенцијалну површину, при чему се стабилизационе енергије групишу у опсегу од −0,1 to −5,0 kJ mol^{-1} унутар дефинисаних геометријских домена. Анализа мрежа додатно је показала да више од половине интеракција учествује у кооперативним, фуркованим слободни пар–π мотивима, који генеришу стабилизацију молекулских простора путем мултивалентних интеракционих мрежа. У целини, ови резултати успостављају слободни пар–π интеракције као геометријски кодиране, енергетски селективне и кооперативно организоване стабилизационе елементе који доприносе међумолекулској специфичности, структурној прецизности и стабилности кватернарне структуре у фикобилипротеинским агрегатима.

(Примљено 2. фебруара, ревидирано 13. марта, прихваћено 30. марта 2026)

REFERENCES

1. M. Konstantinidou, J. M. Virta, M. R. Arkin, *Acc. Chem. Res.* **58** (2025) 2840 (https://doi.org/10.1021/acs.accounts.5c00441)
2. P. Schake, S. N. Bolz, K. Linnemann, M. Schroeder, *Nucleic Acids Res*. **53** (2025) W463 (https://doi.org/10.1093/nar/gkaf361)
3. G. J. Bartlett, A. Choudhary, R. T. Raines, D. N. Woolfson, *Nat. Chem. Biol.* **6** (2010) 615 (https://doi.org/10.1038/nchembio.406)
4. D. A. Dougherty, *Acc. Chem. Res.* **46** (2013) 885 (https://doi.org/10.1021/ar300265y)
5. R. W. Newberry, R. T. Raines, *Acc. Chem. Res.* **50** (2017) 1838 (https://doi.org/10.1021/acs.accounts.7b00121)
6. I. V. Alabugin, M. Manoharan, S. Peabody, F. Weinhold, *J. Am. Chem. Soc.* **125** (2003) 5973 (https://doi.org/10.1021/ja034656e)
7. E. A. Meyer, R. K. Castellano, F. Diederich, *Angew. Chem. Int. Ed.* **42** (2003) 1210 (https://doi.org/10.1002/anie.200390319)
8. G. J. Bartlett, D. N. Woolfson, *Prot. Sci*. **25** (2016) 887 (https://doi.org/10.1002/pro.2896)
9. J. Novotny, S. Bazzi, R. Marek, J. Kozelka, *Phys. Chem. Chem. Phys.* **18** (2016) 19472 (https://doi.org/10.1039/C6CP01524G)
10. J. Kozelka, *Eur. Biophys. J*. **46** (2017) 729 (https://doi.org/10.1007/s00249-017-1210-1)
11. S. K. Singh, A. Das, *Phys. Chem. Chem. Phys.* **17** (2015) 9596 (https://doi.org/10.1039/C4CP05536E)
12. S. Jena, J. Dutta, K. D. Tulsiyan, A. K. Sahu, S. S. Choudhury, H. S. Biswal, *Chem. Soc. Rev.* **51** (2022) 4261 (https://doi.org/10.1039/D2CS00133K)
13. L. Hahn, T. Zorn, J. Kehrein, T. Kielholz, A. L. Ziegler, S. Forster, B. Sochor, E. S. Lisitsyna, N. A. Durandin, T. Laaksonen, V. Aseyev, C. Sotriffer, K. Saalwächter, M. Windbergs, A. C. Pöppler, R. Luxenhofer, *ACS Nano* **17** (2023) 6932 (https://doi.org/10.1021/acsnano.3c00722)
14. L. Chen, X. Ruan, X. Li, H. Fu, *Comput. Mol. Biol.* **14** (2024) 182 (https://doi.org/10.5376/cmb.2024.14.0021)
15. Y. Yuan, C. Chen, X. Guo, B. Li, N. He, S. Wang, *Compr. Rev. Food Sci. Food Saf.* **23** (2024) e13285 (https://doi.org/10.1111/1541-4337.13285)

16. C. García-Gómez, D. E. Aguirre-Cavazos, A. Chávez-Montes, J. M. Ballesteros-Torres, A. A. Orozco-Flores, R. Reyna-Martínez, Á. D. Torres-Hernández, G. M. González-Meza, S. L. Castillo-Hernández, M. A. Gloria-Garza, M. Kačániová, M. Ireneusz-Kluz, J. H. Elizondo-Luevano, *Mar. Drugs* **23** (2025) 201 (https://doi.org/10.3390/md23050201)
17. P. W. Rose, B. Beran, C. Bi, W. F. Bluhm, D. Dimitropoulos, D. S. Goodsell, A. Prlić, M. Quesada, G. B. Quinn, J. D. Westbrook, J. Young, B. Yukich, C. Zardecki, H. M. Berman, P. E. Bourne, *Nucleic Acids Res.* **39** (2011) D392-D401 (https://doi.org/10.1093/nar/gkq1021)
18. A. G. Murzin, S. E. Brenner, T. Hubbard, C. Chothia, *J. Mol. Biol.* **247** (1995) 536 (https://doi.org/10.1016/S0022-2836(05)80134-2)
19. J. M. Word, S. C. Lovell, J. S. Richardson, D. C. Richardson, *J. Mol. Biol*. **285** (1999) 1735 (https://doi.org/10.1006/jmbi.1998.2401)
20. D.S. Biovia, *Discovery Studio Visualizer*, San Diego, CA (2025)
21. V. R. Ribić, S. Đ. Stojanović, M. V. Zlatović, *Int. J. Biol. Macromol*. **106** (2018) 559 (https://doi.org/10.1016/j.ijbiomac.2017.08.050)
22. S. Đ. Stojanović, Z. Z. Petrović, M. V. Zlatović, *J. Serb. Chem. Soc*. **86**, (2021) 781 (https://doi.org/10.2298/JSC210321042S)
23. *Schrödinger Release 2018-1*, Jaguar, Schrödinger, LLC, New York, NY (2018)
24. T. H. Dunning, Jr., *J. Chem. Phys*. **90** (1989) 1007 (https://doi.org/10.1063/1.456153)
25. T. Clark, J. Chandrasekhar, G. W. Spitznagel, P. V. R. Schleyer, *J. Comput. Chem.* **4** (1983) 294 (https://doi.org/10.1002/jcc.540040303)
26. A. D. Bochevarov, E. Harder, T. F. Hughes, J. R. Greenwood, D. A. Braden, D. M. Philipp, D. Rinaldo, M. D. Halls, J. Zhang, R. A. Friesner, *Int. J. Quantum Chem.* **113** (2013) 2110 (https://doi.org/10.1002/qua.24481)
27. G. J. Jones, A. Robertazzi, J. A. Platts, *J. Phys. Chem., B* **117** (2013) 3315 (https://doi.org/10.1021/jp400345s)
28. K. E. Riley, J. A. Platts, J. Řezáč, P. Hobza, J. G. Hill, *J. Phys. Chem., A* **116** (2012) 4159 (https://doi.org/10.1021/jp211997b)
29. E. Cukuroglu, A. Gursoy, O. Keskin, *Nucleic Acids Res*. **40** (2012) D829 (https://doi.org/10.1093/nar/gkr929)
30. M. Egli, S. Sarkhel, *Acc. Chem. Res.* **40** (2007) 197 (https://doi.org/10.1021/ar068174u)
31. T. Steiner, *Angew. Chem. Int. Ed.* **41** (2002) 48 (https://doi.org/10.1002/1521-3773(20020104)41:1%3C48::AID-ANIE48%3E3.0.CO;2-U)
32. T. J. Mooibroek, P. Gamez, J. Reedijk, *CrystEngComm* **10** (2008) 1501 (https://doi.org/10.1039/B812026A)
33. R. W. Newberry, G. J. Bartlett, B. VanVeller, D. N. Woolfson, R. T. Raines, *Prot. Sci.* **23** (2014) 284 (https://doi.org/10.1002/pro.2413)
34. V. A. Adhav, K. Saikrishnan, *ACS Omega* **8** (2023) 22268 (https://doi.org/10.1021/acsomega.3c00205)
35. H. B. Bürgi, J. D. Dunitz, J. M. Lehn, G. Wipff, *Tetrahedron* **30** (1974) 1563 (https://doi.org/10.1016/S0040-4020(01)90678-7)
36. L. M. Salonen, M. Ellermann, F. Diederich, *Angew. Chem. Int. Ed.* **50** (2011) 4808 (https://doi.org/10.1002/anie.201007560)
37. H. B. Bürgi, J. D. Dunitz, E. Shefter, *J. Am. Chem. Soc.* **95** (1973) 5065 (https://doi.org/10.1021/ja00796a058)
38. P. A. Maury, D. N. Reinhoudt, J. Huskens, *Curr. Opin. Colloid Interface Sci.* **13** (2008) 74 (https://doi.org/10.1016/j.cocis.2007.08.013)
39. H. B. Bürgi, *Inorg. Chem.* **12** (1973) 2321 (https://doi.org/10.1021/ic50128a021).

Journal of the Serbian Chemical Society
JSCS-info@shd.org.rs • www.shd.org.rs/JSCS
J. Serb. Chem. Soc. 91 (6) S161–S173 (2026)
Supplementary material

SUPPLEMENTARY MATERIAL TO

Energetic networks of lone pair–π interactions in phycobiliprotein interfaces: Structural organization, geometry and cooperative stabilization

LUKA M. BREBERINA[1], MARIO V. ZLATOVIĆ[2], SRĐAN Đ. STOJANOVIĆ[3] and MILAN R. NIKOLIĆ[1]*

[1]*University of Belgrade – Faculty of Chemistry, Department of Biochemistry, Belgrade, Serbia,* [2]*University of Belgrade – Faculty of Chemistry, Department of Organic Chemistry, Belgrade, Serbia and* [3]*University of Belgrade, Institute of Chemistry, Technology and Metallurgy – National Institute of the Republic of Serbia, Department of Chemistry, Belgrade, Serbia*

J. Serb. Chem. Soc. 91 (6) (2026) 573–588

The tables below present the Cartesian coordinates (xyz format) of the representative dimers selected for the Supplementary Material. R denotes the distance between the lone pair donor atom (O) and the centroid of the aromatic π system. θ represents the angle between the donor–centroid vector and the normal to the aromatic ring plane, describing the approach of the lone pair toward the π system. All optimized structures correspond to true minima on the potential energy surface, with no imaginary frequencies.

Because the full dataset contains a large number of interacting pairs, only representative dimers illustrating the principal classes of lone pair–π interactions were selected for detailed presentation in the Supplementary Material. The selected examples cover the main types of donor residues and aromatic π systems observed in the structural dataset and reproduce the characteristic geometrical parameters identified in the statistical analysis.

* Corresponding author. E-mail: mnikolic@chem.bg.ac.rs

Table S-I. Cartesian coordinates of representative dimers

1. 4F0U - A:THR96:OG1 - B:TYR18

Donor residue	Donor atom	Aromatic residue	R (Å)	θ (°)
THR A96	OG1	TYR B18	5.11	57.17

XYZ coordinates

Atom	X	Y	Z
C	-47.9740	25.3270	80.8670
O	-49.1390	26.1040	80.5650
C	-47.2110	25.9910	82.0180
H	-48.2390	24.4320	81.1310
H	-48.9120	26.8930	80.3890
H	-47.7870	26.0510	82.7960
H	-46.4280	25.4610	82.2360
H	-46.9340	26.8820	81.7520
H	-47.3330	25.2730	79.9870
C	-53.1440	26.7670	83.9440
C	-52.1970	27.9510	84.0300
C	-50.8230	27.7790	83.8620
C	-52.6670	29.2380	84.3090
C	-49.9470	28.8510	83.9710
C	-51.7970	30.3120	84.4220
C	-50.4400	30.1110	84.2510
O	-49.5740	31.1680	84.3570
H	-53.6280	26.7020	84.7820
H	-52.6150	25.9580	83.8580
H	-50.4880	26.9320	83.6740
H	-53.5800	29.3760	84.4210
H	-49.0330	28.7210	83.8560
H	-52.1240	31.1620	84.6120
H	-49.9800	31.8320	84.6730
H	-53.8300	26.8760	83.1040

2. 1CPC - L:THR96:OG1 - K:PHE18

Donor residue	Donor atom	Aromatic residue	R (Å)	θ (°)
THR L96	OG1	PHE K18	5.08	59.80

XYZ coordinates

Atom	X	Y	Z
C	11.0670	-28.2090	-6.4320
C	11.8900	-27.7530	-7.6390
C	12.6700	-26.6110	-7.5420
C	11.7760	-28.4370	-8.8380
C	13.3320	-26.0900	-8.6530
C	12.4610	-27.9130	-9.9520
C	13.2210	-26.7290	-9.8620
H	11.5890	-28.1100	-5.6210
H	10.8510	-29.1510	-6.5170
H	12.7530	-26.1840	-6.7200
H	11.2670	-29.2120	-8.9050
H	13.8440	-25.3170	-8.5750
H	12.4110	-28.3590	-10.7670
H	13.6430	-26.3840	-10.6150
H	10.1520	-27.6210	-6.3610
C	8.6210	-30.4880	-11.9670
O	8.5540	-29.3560	-11.0670
C	10.0640	-30.7940	-12.3830
H	8.3200	-31.2620	-11.4660
H	8.3900	-28.6580	-11.5050
H	10.6290	-30.8230	-11.5950
H	10.0960	-31.6520	-12.8350
H	10.3820	-30.1010	-12.9830
H	7.9920	-30.3250	-12.8420

3. 2BV8 - P:TYR74:OH - K:TYR90

Donor residue	Donor atom	Aromatic residue	R (Å)	θ (°)
TYR K90	OH	TYR P74	4.90	74.72

XYZ coordinates

Atom	X	Y	Z
C	2.2490	46.8700	86.8180
C	2.3420	47.4430	88.2260
C	1.2890	47.3000	89.1630
C	3.4330	48.2530	88.5610
C	1.3240	47.9710	90.3810
C	3.4840	48.9290	89.7500
C	2.4210	48.7920	90.6520
O	2.4740	49.5430	91.7750
H	3.1250	46.5330	86.5720
H	2.0430	47.5970	86.2100
H	0.5660	46.7510	88.9610
H	4.1400	48.3340	87.9620
H	0.6350	47.8750	90.9990
H	4.2120	49.4700	89.9560
H	3.1810	49.9970	91.7760
H	1.4950	46.0850	86.7620
C	1.4710	55.4340	91.0980
C	0.7760	54.3180	90.3650
C	1.3080	53.0090	90.3600
C	-0.3900	54.5740	89.6510
C	0.6760	51.9690	89.6350
C	-1.0360	53.5650	88.9300
C	-0.5050	52.2720	88.9180
O	-1.1330	51.3230	88.1480
H	1.6180	55.1650	92.0180
H	0.8890	56.2100	91.1190
H	2.0840	52.8280	90.8390
H	-0.7470	55.4330	89.6530

Atom	X	Y	Z
H	1.0290	51.1090	89.6310
H	-1.8160	53.7530	88.4600
H	-1.7550	51.6820	87.7120
H	2.4170	55.6780	90.6150

4. 1F99 - N:MET79:SD - K:PHE122

Donor residue	Donor atom	Aromatic residue	R (Å)	θ (°)
MET N79	SD	PHE K122	5.69	65.81

XYZ coordinates

Atom	X	Y	Z
C	-27.9410	38.8900	59.3320
C	-26.7160	38.9550	60.2390
C	-26.6930	39.8310	61.3110
C	-25.6500	38.0970	60.0320
C	-25.6100	39.8400	62.1720
C	-24.5740	38.1120	60.8960
C	-24.5540	38.9800	61.9680
H	-27.6700	38.6210	58.4400
H	-28.3340	39.7740	59.2540
H	-27.4050	40.4130	61.4520
H	-25.6590	37.5100	59.3110
H	-25.5950	40.4290	62.8910
H	-23.8590	37.5340	60.7550
H	-23.8300	38.9840	62.5510
H	-28.6710	38.1870	59.7330
C	-18.7680	37.7120	58.5160
C	-20.0970	37.8890	59.2390
S	-19.9610	38.5510	60.9210
C	-19.7100	40.2510	60.4960
H	-18.3890	38.5870	58.3390
H	-18.9330	37.2950	57.6560
H	-20.6600	38.4810	58.7160
H	-20.5470	37.0310	59.2780
H	-19.6130	40.7760	61.3060
H	-18.9070	40.3350	59.9580
H	-20.4720	40.5740	59.9910
H	-18.0830	37.1090	59.1120

5. 1F99 - N:SER94:OG - M:PHE18

Donor residue	Donor atom	Aromatic residue	R (Å)	θ (°)
SER N94	OG	PHE M18	5.12	61.56

XYZ coordinates

Atom	X	Y	Z
C	-26.5750	21.9370	70.3080
C	-26.0230	23.3590	70.3590
C	-25.7200	24.0440	69.1940
C	-25.8180	23.9620	71.5850
C	-25.2110	25.3250	69.2730
C	-25.3090	25.2440	71.6530
C	-25.0040	25.9260	70.4980
H	-27.1790	21.8670	69.5520
H	-27.1010	21.7810	71.1080
H	-25.8580	23.6450	68.3660
H	-26.0240	23.5030	72.3670
H	-25.0060	25.7880	68.4930
H	-25.1720	25.6460	72.4800
H	-24.6600	26.7890	70.5420
H	-25.7670	21.2100	70.2270
C	-24.2480	23.3660	75.9470
O	-23.8090	22.6280	74.8140
H	-25.0830	22.9830	76.2580
H	-24.4400	24.2740	75.6660
H	-22.9890	22.7630	74.6920
H	-23.4960	23.3530	76.7360

6. 1B33 - A:SER31:OG - J:TYR72

Donor residue	Donor atom	Aromatic residue	R (Å)	θ (°)
SER A31	OG	TYR J72	4.72	70.20

XYZ coordinates

Atom	X	Y	Z
C	84.5680	55.1380	62.0110
O	83.5100	54.3010	61.5580
H	85.0480	55.4890	61.2450
H	85.1990	54.6080	62.5230
H	83.2340	53.8280	62.1950
H	84.1750	55.9530	62.6190
C	85.7980	51.6340	57.5020
C	85.5740	53.1320	57.3700
C	85.5920	53.7530	56.1200
C	85.3930	53.9330	58.4950
C	85.4400	55.1300	55.9950
C	85.2440	55.3160	58.3790
C	85.2690	55.9040	57.1270
O	85.1320	57.2670	57.0050
H	85.1480	51.1680	56.9540
H	85.6360	51.3700	58.4210
H	85.7080	53.2360	55.3560
H	85.3710	53.5400	59.3380
H	85.4530	55.5280	55.1540
H	85.1290	55.8390	59.1390
H	85.2410	57.4890	56.2020
H	86.8120	51.3700	57.2010

7. 2BV8 - O:TYR74:OH - E:PHE63

Donor residue	Donor atom	Aromatic residue	R (Å)	θ (°)
TYR O74	OH	PHE E63	5.39	78.09

XYZ coordinates

Atom	X	Y	Z
C	31.8940	120.3860	59.0470
C	30.5110	120.0440	59.5600
C	30.3250	119.6500	60.8950
C	29.3960	120.1410	58.7190
C	29.0390	119.3630	61.3860
C	28.1050	119.8590	59.1830
C	27.9040	119.4700	60.5180
H	31.9000	120.2970	58.0810
H	32.5260	119.7380	59.3960
H	31.0600	119.5780	61.4600
H	29.5150	120.3980	57.8330
H	28.9250	119.1040	62.2720
H	27.3790	119.9290	58.6060
H	27.0490	119.2850	60.8330
H	32.1760	121.3970	59.3430
C	29.4980	121.1460	70.6350
C	29.2330	120.6950	69.2200
C	29.9220	119.6050	68.6740
C	28.2570	121.3270	68.4370
C	29.6440	119.1500	67.3780
C	27.9690	120.8840	67.1460
C	28.6630	119.7930	66.6200
O	28.3580	119.3370	65.3490
H	29.0260	121.9770	70.8010
H	30.4440	121.3310	70.7410
H	30.5740	119.1760	69.1790
H	27.7930	122.0540	68.7840
H	30.1090	118.4260	67.0260

Atom	X	Y	Z
H	27.3180	121.3130	66.6390
H	27.7540	119.8170	65.0170
H	29.1790	120.3810	71.3430

8. 4L1E - A:GLN33:OE1 - C:PHE28

Donor residue	Donor atom	Aromatic residue	R (Å)	θ (°)
GLN A33	OE1	PHE C28	5.04	57.50

XYZ coordinates

Atom	X	Y	Z
C	-64.2980	-4.9460	-31.8280
C	-65.3780	-4.0120	-31.3100
C	-66.0540	-4.5310	-30.0540
O	-65.4560	-5.2710	-29.2710
N	-67.3090	-4.1440	-29.8560
H	-63.7040	-5.1750	-31.0960
H	-63.7660	-4.4750	-32.4880
H	-64.9870	-3.1430	-31.1260
H	-66.0460	-3.8820	-32.0010
H	-67.6940	-3.6270	-30.4250
H	-67.7360	-4.4110	-29.1590
H	-64.7400	-5.8440	-32.2600
C	-61.3090	-6.8840	-25.7900
C	-62.6050	-6.4500	-25.1580
C	-63.0480	-7.0200	-23.9760
C	-63.3830	-5.4690	-25.7500
C	-64.2360	-6.6220	-23.3990
C	-64.5750	-5.0690	-25.1740
C	-64.9970	-5.6440	-23.9980
H	-61.0430	-6.2220	-26.4470
H	-61.4550	-7.7150	-26.2680
H	-62.5370	-7.6800	-23.5660
H	-63.1010	-5.0750	-26.5440
H	-64.5230	-7.0140	-22.6060
H	-65.0910	-4.4110	-25.5820
H	-65.7960	-5.3720	-23.6080
H	-60.5340	-7.0070	-25.0330

9. 1B33 - O:GLN41:OE1 - K:TYR87

Donor residue	Donor atom	Aromatic residue	R (Å)	θ (°)
GLN O41	OE1	TYR K87	5.38	68.67

XYZ coordinates

Atom	X	Y	Z
C	111.3190	1.4800	72.0210
C	110.0370	0.7600	71.6620
C	109.9240	-0.6200	71.8120
C	108.9720	1.4430	71.0790
C	108.7770	-1.3140	71.3770
C	107.8180	0.7660	70.6420
C	107.7240	-0.6170	70.7890
O	106.6010	-1.2950	70.3280
H	111.6630	1.1320	72.8580
H	111.1340	2.4220	72.1600
H	110.6200	-1.0930	72.2070
H	109.0250	2.3660	70.9760
H	108.7230	-2.2360	71.4820
H	107.1180	1.2410	70.2550
H	106.0560	-0.7450	70.0020
H	112.0570	1.3540	71.2290
C	102.2830	4.4460	72.6030
C	103.6160	3.8410	72.9740
C	104.3110	3.2470	71.7820
O	105.1110	3.9130	71.1260
N	103.9810	2.0050	71.4610
H	101.5870	3.7830	72.7310
H	102.2890	4.6720	71.6600
H	104.1810	4.5220	73.3710
H	103.4840	3.1550	73.6460
H	103.4180	1.5710	71.9450
H	104.3300	1.6320	70.7690
H	102.0840	5.3310	73.2070

10. 1ALL - A:GLY34:O - B:PHE31

Donor residue	Donor atom	Aromatic residue	R (Å)	θ (°)
GLY A34	O	PHE B31	4.70	35.17

XYZ coordinates

Atom	X	Y	Z
N	5.3890	16.0670	10.0080
C	6.0910	16.4900	11.1890
C	7.0790	15.4710	11.7110
O	8.2350	15.8040	11.9580
H	4.5320	16.1310	10.0510
H	6.5620	17.3160	10.9960
H	5.4450	16.6880	11.8850
H	5.6360	15.0420	9.8250
H	6.7650	14.4390	11.8680
C	2.9170	16.5310	14.9570
C	4.0070	17.5050	14.5450
C	3.7150	18.6100	13.7450
C	5.3260	17.3170	14.9740
C	4.7120	19.5150	13.3790
C	6.3360	18.2120	14.6170
C	6.0240	19.3200	13.8130
H	3.2510	15.9730	15.6770
H	2.7230	15.9440	14.2100
H	2.8430	18.7450	13.4510
H	5.5330	16.5830	15.5060
H	4.5020	20.2480	12.8460
H	7.2080	18.0760	14.9090
H	6.6900	19.9220	13.5700
H	2.0200	17.0660	15.2690

Journal of the Serbian Chemical Society
JSCS-info@shd.org.rs • www.shd.org.rs/JSCS
J. Serb. Chem. Soc. 91 (6) 589–602 (2026)
JSCS–5512
Original scientific paper
Published 2 July, 2026

Embracing green chromatography principles in perindopril, amlodipine and indapamide drug mixture analysis using *β*-cyclodextrin modified mobile phase

HUSEINATU OSMAN*, JEVREM STOJANOVIĆ, ANA PROTIĆ, MIRA ZEČEVIĆ and BILJANA OTAŠEVIĆ**

Department of Drug Analysis, University of Belgrade – Faculty of Pharmacy, Vojvode Stepe 450, 11221 Belgrade, Serbia

(Received 4 December 2025, revised 6 February, accepted 11 March 2026)

Abstract: Raising the level of environmental awareness in the field of liquid chromatography is considered indispensable while the use of *β*-cyclodextrin, as additive, in a mobile phase is promising strategy in this regard. This study presents a method development in line with ICH Q14 regulatory requirements for introducing sustainability and method life-cycle management to separate components of a cardiovascular multi-drug tablet formulation. At the beginning, the analytical method target profile was defined, separation of perindopril, amlodipine, and indapamide in a shortest possible analytical run time. Following risk analysis pointed out that the mobile phase constituents represent the critical method parameters affecting the chromatographic analyses. Design of experiments methodology and desirability function calculation was employed to simultaneously optimize the levels of concentration of *β*-cyclodextrin solution, pH value and acetonitrile content in the mobile phase investigated in the ranges 5–15 mM, 4.0–6.0 and 20–30 vol. %, respectively. The optimal chromatographic conditions consisted of 10 mM *β*-cyclodextrin (pH 5.4) and acetonitrile in the volume ratio 70:30, 2 mL min^{-1} flow rate, RP-18e column kept at 25 °C, 215 nm detection wavelength, and 10 µL injection volume. The eco-friendliness of the method was assessed using the AGREE tool indicating a green and sustainable method was successfully developed.

Keywords: HPLC method development; design of experiments; desirability function; cardiovascular multi-drug tablet formulation; AGREE assessment tool.

*,** Corresponding authors. E-mail: (*)oshusei@gmail.com; (**)biljana.otasevic@pharmacy.bg.ac.rs
https://doi.org/10.2298/JSC251204013O

INTRODUCTION

Achieving sustainability in the domain of pharmaceutical sciences involves integrating environmental and social considerations from the earliest stages of development through to end-of-life management. This includes using green chemistry principles, developing eco-friendly analytical methods, designing sustainable manufacturing processes and optimizing drug product formulations, packaging and distribution to reduce waste and energy consumption.[1]

Multi-drug formulations have increasingly become a significant challenge in the field of drug analysis due to the complexity and resource demanding requirements associated with resolving these compounds. This is attributed to the growing interest in rationally designed multi-target drugs, also known as multimodal drugs, network therapeutics or designed multiple ligands. These drugs have emerged as an appealing drug discovery paradigm over the past decade to address diseases with complex etiologies and those exhibiting substantial drug resistance.[2,3] Multi--drugs are also means to sustainable environment as less resources are used in their manufacture and consecutive quality control analysis.

Multi-component drug formulation used in this research comprised of a mixture of perindopril *tert*-butylamine (also referred as perindopril erbumine), amlodipine besylate and indapamide active pharmaceutical substances which structures are presented in Fig. 1. Their respective drug formulation has been successfully used for the treatment of cardiovascular diseases, considering that perindopril is an angiotensin-converting enzyme inhibitor that lowers blood pressure by reducing sodium and water retention,[4] amlodipine besylate is a calcium channel blocker that lowers blood pressure by relaxing blood vessels[5] and indapamide is a diuretic that causes water elimination hence reducing the pressure inside blood vessels.[6]

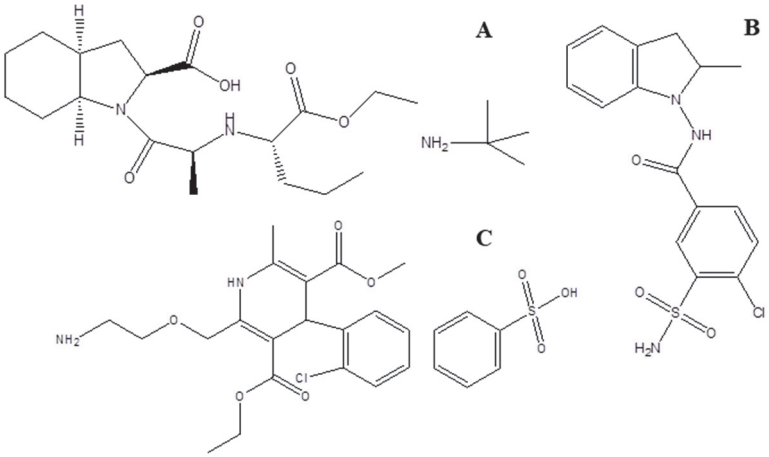

Fig. 1. Chemical structures of: A) perindopril erbumine, B) indapamide and C) amlodipine besylate.

In the realm of drug analysis, high pressure liquid chromatography (HPLC) stands as the de facto gold standard. Among the various HPLC techniques, reversed phase high performance liquid chromatography (RP-HPLC) predominates, comprising approximately 75 % of the reported methodologies. Historically, the technique has predominantly utilized acetonitrile as preferred organic solvent in the mobile phase. At the same time, contemporary scientific advancements, particularly the green analytical chemistry (GAC) concept, emphasize the primary objective of reducing or eliminating the utilization and production of substances that pose risks to human health or the environment, as delineated by Anastas.[1] It is evident now that HPLC inherently lacks environmental friendliness due to the substantial quantities of solvents employed, which ultimately become waste at the end of the analysis. These wastes become more hazardous to the environment as well as the health and wellbeing of analysts involved if the solvents used are toxic. In the light of the growing need to achieve the global Sustainable Development Goals, SDG 9.4, which aims to enhance research and upgrade industrial technologies, particularly in developing countries, by 2030. SDG 12.4–6 also focuses on the environmentally sound management of chemicals and waste, aiming to reduce their release and minimize adverse impacts on human health and the environment.[7] However, new and promising strategies highlighted as green chromatography principles that rely on the adjustment of the mobile phase composition emerge, thereby enhancing sustainability of the HPLC method without compromising its performance.[8–11] There have been several assessment tools for measuring such achievement of a method, such as the GAPI, ESA and NEMI index. However, recently released AGREE tool incorporated in an open access software outstands out for his notable and relevant advantages. In addition to the ecological criteria evaluated by other tools, AGREE considers the number of analytes determined in a single run, sample throughput, automation, and the use of chemicals from renewable sources.[12,13]

The inclination towards introducing GAC concept in the field of drug analysis and the literature review of the reported HPLC methods used for the quality control of ternary drug combination containing perindopril erbumine, amlodipine besylate and indapamide revealing that these methods have predominantly utilized extensive amounts of toxic organic solvents, indicated that it is necessary to offer analytical procedure improvement by means of development of an alternative sustainable and eco-friendly HPLC method.[14,15]

Cyclodextrins (CDs) are semi-natural compounds derived from starch (a renewable resource) through enzymatic conversion. Their diverse applications in chemistry, pharmaceuticals, food and cosmetics stem from their non-toxicity and cost-effectiveness.[16] When CDs are used as additives into the mobile phases in HPLC analysis they could reduce the organic solvent–water ratio without compromising selectivity or resolution. The potential usefulness of CDs in HPLC separations comes out of the ability of CDs to form inclusion complexes with the guest

molecules thus affecting their retention. The efficiency of complexation depends on the structural compatibility between the CD and the guest molecule. The height and internal diameter of the CD cavity are determined by the number of glucose units. α-CD has a lower internal diameter compared to β-CD and γ-CD, enabling them to incorporate low molecular weight compounds with aliphatic chains, β-CD can accommodate heterocyclic and aromatic compounds, spanning a wide range of active pharmaceutical substances (APIs), while γ-CD can accommodate complex macrocycles and steroids. Among others, β-CDs are the most utilized CDs in pharmaceutical formulations. Furthermore, β-CD's weak adsorption onto C18 columns ensures preserving high column performance, facilitates easy washing, and minimizes damage compared to other CDs. At the same time, all CDs possess a unique advantage over other commonly used mobile phase additives by being transparent within the ultraviolet-visible range predominantly used in detectors in HPLC instruments.[13,17,18]

Sustainability in the field of development of analytical methods may be achieved by using various computer technology related products such as advanced data processing software and strategies that enable reduction of experimental work while maintaining high quality of gathered data. In that respect, the application of Design of Experiments (DoE) methodology has been recognized in the field of drug analysis over past decades. DoE is a robust structural approach based on the multifactorial planning of order and number of experiments to be executed thus reducing the use of resources as well the generation of waste, but as the most important fact, enabling better insight into factor interactions and factor response relations. DoE serves as a technique for optimizing multivariate systems, such as liquid chromatography, where various interdependent mechanisms, including column efficiency, retention factor, ionization efficiency and ion suppression, analytes' solubility, significantly impact the analysis.[19–21] At the same time, according to the International council for harmonization of technical requirements for pharmaceuticals for human use (ICH) Q14 guideline, adopting smarter method development approach supported by principles of quality risk management, enhances the reliability of analytical methods.[22] Developed methods also undergo the systematic process of method validation in accordance with ICH Q2(R1/R2)[23] guideline which is considered as necessary to ensure that the developed method is fit for its intended use.

Having all this in mind, the aim of this study was focused on the DoE supported development and validation of a HPLC method with β-CD-modified mobile phase as an eco-friendly HPLC alternative for the separation of the three APIs, perindopril erbumine, amlodipine besylate and indapamide from a comercially available tablet formulation.

EXPERIMENTAL

Chemicals and reagents

β-CD of 98 % purity was purchased from Acros Organics, USA. An HPLC grade acetonitrile, water and ethanol were purchased from J.T. Baker Inc., USA. Perindopril erbumine, amlodipine besylate and indapamide reference substances were of Ph. Eur. quality. Co-Amlessa tablets containing 4 mg of perindopril erbumine, 10 mg of amlodipine besylate and 1.25 mg of indapamide per one tablet (Krka-Farma, Serbia) were purchased from a local drug store.

Chromatographic conditions and equipment

The experiments were performed on a Vanquish Core 3000 HPLC system (Thermo Fisher Scientific) equipped with quaternary pumps, autosampler, thermostated column department, and PDA detector. Chromatographic data was collected using Chromeleon® 7.0 and Chrom Quest 4.2 chromatography data system. Merck Chromolith RP-18e column (100 mm×4.6 mm, macropore size 2 μm, mesopore size 13 nm) was used for separations. *β*-CD aqueous solutions were prepared in the concentration range 5–15 mM. The organic part of mobile phase consisted of acetonitrile in range 20–30 vol. %. Column temperature was 25 °C, flow rate 2 mL min^{-1}, injection volume 20 μL and detection wavelength 215 nm.

Stock and working solutions preparation

Stock solutions were prepared by dissolving the powder reference substances in 50 vol. % ethanol to attain concentrations of 1 mg mL^{-1} for each API. Stock solutions were further diluted using the mixture of 10 mM *β*-CD (pH 5.4) and acetonitrile (70:30 volume ratio) as solvent to prepare one working solution containing 20 μg mL^{-1} of perindopril erbumine, 50 μg mL^{-1} of amlodipine besylate and 6.25 μg mL^{-1} of indapamide to be used within method optimization. A series of five working solutions containing raising concentrations of all APIs were prepared from stock solutions by dilution with the aforementioned solvent to be used within method linearity evaluation. Raising concentrations of working solutions were as follows: 10, 15, 20, 25 and 30 μg mL^{-1} for perindopril erbumine, 25.0, 37.5, 50.0, 62.5 and 75 μg mL^{-1} for amlodipine besylate and 3.125, 4.688, 6.250, 7.813 and 9.325 μg mL^{-1} for indapamide.

Sample preparation

The stock sample solution was prepared with the appropriate amount of powdered tablet mass containing 4 mg of perindopril erbumine, 10 mg of amlodipine besylate and 1.25 mg of indapamide and transferring it to a 50 mL volumetric flask. The volumetric flask was filled with 50 vol. % ethanol and the solution was filtered. Working sample solution was prepared by transferring of 2.5 mL of stock solution in 10 mL volumetric flask and dilution with the aforementioned solvent to attain concentrations 20, 50 and 6.25 μg mL^{-1} for perindopril erbumine, amlodipine besylate and indapamide, respectively, denoted as 100 % concentration level with respect to the declared value for each API. This sample solution was used both for method optimization and method repeatability test (6 sample solutions repetitive analysis) and intermediate method precision test (6 working solutions repetitive analysis performed on three separate days by different analysts) within method validation procedure. The similar procedure was applied for preparation of test sample solutions for accuracy test within method validation procedure with the difference that respective volumes of stock solution were transferred in a 50 mL volumetric flask, mixed with placebo and filled to volume with the aforementioned solvent to attain concentrations 80, 200 and 25 μg mL^{-1} for perindopril erbumine, amlodipine besylate and indapamide, respectively. This solution was filtered and diluted with the same solvent to attain test solution

containing 16, 40 and 5.00 μg mL^{-1} for perindopril erbumine, amlodipine besylate and indapamide, respectively, representing 80 % concentration level for each API. Similarly, test solutions containing 20, 50 and 6.25 μg mL^{-1} representing 100 % concentrations level and 24, 60 and 7.50 μg mL^{-1} representing 120 % concentration level for perindopril erbumine, amlodipine besylate and indapamide, respectively, were prepared. The test sample solutions were prepared in triplicate for each of these concentration levels.

Method optimization

The influence of experimental factors on the retention behavior of the analytes was assessed with experimental design whose plan was constructed as well as obtained results processing using multiple regression analysis was performed using Design Expert 11.0.0 software (Stat-Ease Inc., USA). The Box–Behnken response surface design was used comprising of a total of 15 runs within which 3-level factors are varied in a predefined manner involving factor levels at the midpoints of the edges of the experimental space and level positioned at the center of the experimental space. The center point experiment was repeated 3 times in order to evaluate the experimental error.[15,16] Simultaneous optimizations of multiple responses or multi-objective method optimization, was also performed using the same software upon setting the specific numerical target values for each of the observed responses. Firstly, individual desirability functions are calculated with a value of 1 for the most ideal outcome for each of the observed responses reaching its target value and 0 for the least desirable outcome. Afterwards, the global desirability function was calculated combining the results of individual desirability functions assigning an overall score also expressed in a range of values 0–1. The overall desirability function represents a compromise and points out to the optimal experimental setup for which all observed responses are the closest possible to their individual target value.

Greenness assessment

Using the AGREE assessment scale, the method was graded for its greenness according to a twelve-point metric system adopted from the 12 GAC principles. Each of the 12 input variables is transformed into a scale in the 0–1 range, and the final result is the product of the assessment results for each GAC principle. The output is a clock-like graph, with the overall score and color representation generated using AGREE calculator (University of Vigo, Spain).

RESULTS AND DISCUSSION

According to the analytical method development strategy described within ICH Q14 recommendations, the first step is to define the target analytical profile of the new method. The optimization goals were accordingly aligned for the developed method to demonstrate satisfactory separation of adjacent peaks achieved within the least possible total analysis time. The observed chromatographic responses recognized as critical method attributes for achieving these optimization goals (CMAs) were retention factor (k) of the last eluting compound from the mixture, indapamide, as well as measure of separation, selectivity factors between all peak pairs (according to the observed elution order, the selectivity factors were: α_{1-2} between amlodipine and perindopril peaks and α_{2-3} between perindopril and indapamide peaks).

Multiple factors may affect the retention properties of the APIs under review. They may be classified as analysts, samples, mobile phase, column, instrument and

detection related factors, as presented in Ishikawa or fishbone diagram (Fig. 2). The factor classification followed with constant, noise and experimental (CNX) evaluation as a risk analysis approach, enables insight into the critical method parameters (CMPs) of the analytical method.[21] The CNX risk-based approach defines the method parameters that should be kept under control, at constant level (marked with yellow color), which ones may be disregarded as noise factors (colored in green) and which parameters require detail experimental evaluation (colored in red). From the perspective of the GAC concept, special attention must be paid to materials, energy and waste. Factors that influence solvent consumption and directly affect the amount of generated wasted include the composition of the mobile phase. Therefore, the selection of suitable solvents is considered the most important step in the intended method development process.

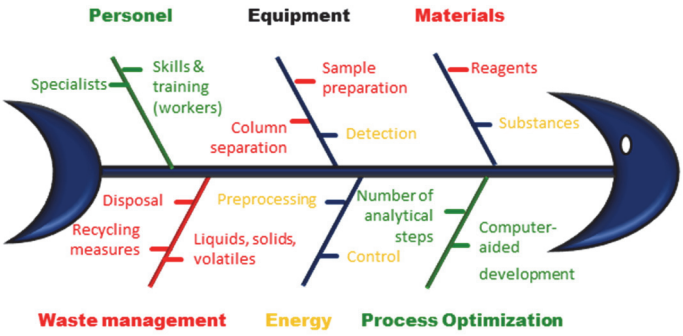

Fig. 2. Classification of important analytical method aspects with risk-assessment.

C18 reversed-phase stationary phase and the type of chromatographic column was selected before the method is optimized, based on previous experience and recommendations from the literature.[18] The stationary phase of monolithic columns is composed of highly porous continuous silica network, with macro- and mesopores. Macropores are 2 μm in size, and they are responsible for low resistance towards mobile phase flow. Therefore, monolithic columns are compatible with a high mobile phase flow rate, even up to 10 mL min^{-1}, accompanied by low pressure in the system. On the other hand, mesopores are smaller in comparison to macropores and they account for a huge active surface, approximately 300 m^2 g^{-1}, which enables efficient chromatographic separation. Allowing faster mobile phase flow rates and thus shortening the duration of chromatographic analyses, together with its compatibility with highly viscous mobile phases, such as CD-modified mobile phases, made the monolithic column the ideal choice for the separation of the intended drug mixture. With reference to other studies dealing with the use of β-CD in HPLC analysis, a study performed by Đajić *et al.*[18] recommended the use of β-CD aqueous solutions in a concentration range of 5–15 mM. The pH range for intended β-CD solutions was considered to be aligned with the pK_a values of the APIs. It

was considered reasonable to for perindopril being the least lipophilic compound, to select a pH range where he is present in an undissociated form (pK_a values of perindopril, indapamide and amlodipine are 3.79, 8.85 and 9.60, respectively), while for other two compounds being very lipophilic to select pH value where they will have smaller affinity towards reversed-phase stationary phase (log *P* values of perindopril, indapamide and amlodipine are 0.63, 2.52 and 2.20, respectively). Therefore, the pH range of pH 4.0–6.0 was selected. To provide an appropriate total analytical run time, a relatively small amount of acetonitrile (20–30 vol. %) was used to complete the mobile phase. The relationship between selected CMPs whose levels were investigated inside experimental space bordered as described and CMAs was investigated using DoE supported regression analysis. The plan of experiments according to Box–Behnken response surface design together with results obtained for observed responses is presented in Table I.

TABLE I. DoE plan of experiments and results obtained for observed responses

β-CD concentration, mM	Acetonitrile content, vol. %	pH	$\alpha_{1\text{-}2}$	$\alpha_{2\text{-}3}$	*k*
15	20	5	11.388	7.834	13.024
15	25	6	3.301	8.378	6.992
5	20	5	7.097	2.589	5.030
15	25	4	1.945	5.474	4.392
10	25	5	5.087	8.060	7.171
10	25	5	3.884	6.668	6.234
5	30	5	7.920	3.174	4.158
15	30	5	2.507	6.610	4.222
5	25	4	2.812	6.783	7.325
10	25	5	3.693	7.557	7.270
10	30	6	3.191	7.574	4.089
10	20	6	4.960	3.478	4.952
10	30	4	2.469	5.953	4.051
10	20	4	2.863	10.806	14.114
5	25	6	4.885	6.100	3.522

Processing the data in Design Expert 11.0.0 software, regression mathematical models were obtained which enabled interpreting the dependence of the selected responses on the examined factors in their corresponding ranges. All models were in the form of a quadratic polynomial equation, while the need for response transformation was indicated by the software in some cases: the response $\alpha_{1–2}$ was used as is, while the response $\alpha_{2–3}$ was used as inverse square root and the response *k* was transformed with the power function, as shown in Table II. To facilitate the presentation of the polynomial equation, investigated factors are coded as follows: *A* stands for *β*-CD concentration (mM), *B* for acetonitrile content, vol. % and *C* for pH value of the aqueous part of the mobile phase. Only coefficients of regression

model whose *p*-values were lower than 0.05 threshold limit indicating their statistical significance to the observed response were presented. The negative value of a coefficient in a polynomial equation indicates that the observed response decreases with the increase of the investigated factor levels, while the positive value of a coefficient indicated the same direction of a change of levels of investigated factors and values of observed responses. According to the size of the absolute values of coefficients in polynomial equations, it was evident that acetonitrile content, vol. %, appeared as the most influential factor for all observed responses, usually resulting in the observed response decrease, while the influence of other factors as well as the intensity of two-factor interactions changed from response to response. Regression models were also evaluated according to obtained values of coefficients of determination (R^2, adjusted R^2 and R^2 predicted), and the statistical significance of lack of fit value (Table III). The closeness of coefficients of determination to 1 and *p*-values of lack of fit being greater than 0.5 threshold limit indicated satisfactory ability of mathematical models to describe the observed chromatography systems and thus may be used for predicting retention properties of APIs according to predefined optimization goals.[19,20]

TABLE II. Coefficients of the regression models

Coefficient	$\alpha_{1\text{-}2}$	$1/(\sqrt{\alpha_{2\text{-}3}})$	$k^{2.36}$
Intercept	4.220	0.370	0.011
A	–0.450	–0.097	–0.005
B	–1.280	–0.021	0.011
C	0.780	0.065	0.005
AB	–2.430	0.023	0.004
AC	–0.180	–0.140	–0.016
BC	–0.340	–0.051	–0.005
A^2	1.440	0.120	0.007
B^2	1.570	–0.004	0.006
C^2	–2.420	0.021	0.008

TABLE III. Statistical profile of the regression models

Model	R^2	Adjusted R^2	Predicted R^2	Lack of fit *p*-value
$\alpha_{1\text{-}2}$	0.9367	0.8228	0.7602	0.2825
$1/(\sqrt{\alpha_{2\text{-}3}})$	0.9872	0.9641	0.8281	0.2701
$k^{2.36}$	0.9958	0.9882	0.9775	0.8938

3D-response surfaces were constructed and used as visualization tools for easier understanding of the APIs' retention behavior (Fig. 3). They show the dependence of each of the observed CMAs from the two selected CMPs while the remaining CMP is kept on a constant level. The analysis of the 3D response surfaces indicated that the increase in the acetonitrile content led to a decrease in

retention of all APIs. When observing the influence of acetonitrile on the selectivity factors, the wavy appearance of response surfaces indicated the significant presence of factor interactions or mutual influence of acetonitrile in combination with other CMPs. In addition, the increase of β-CD concentration demonstrated a similar influence on retention pointing out that significant complexation between drug guest molecules and β-CD occurred enabling the mobile phase to retain appropriate elution strength.

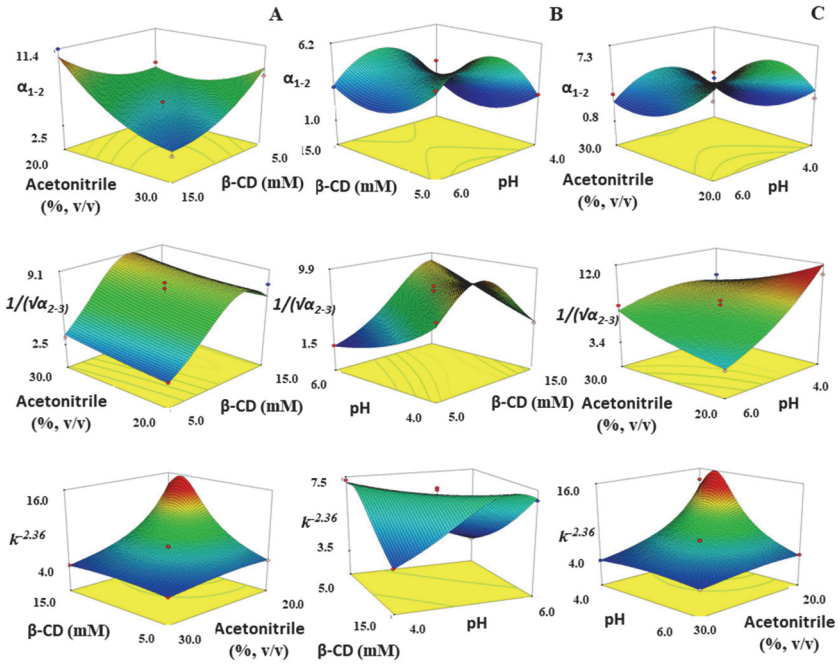

Fig. 3. Response surfaces describing dependencies of observed responses $\alpha_{1\text{-}2}$, $1/(\sqrt{\alpha_{2\text{-}3}})$ and $k^{2.36}$, respectively from factors: acetonitrile content (vol. %) and β-CD concentration (mM), *A*, pH value and β-CD concentration (mM), *B*, and pH value and acetonitrile content (vol. %), *C*.

The steep slope of the response surfaces describing the variation of β-CD concentration indicated the most significant influence of this factor on all observed responses, while the pH of the aqueous part of the mobile phase was always of lower importance. Interestingly, although the appearance of the response surfaces for the response $1/(\sqrt{\alpha_{2-3}})$ pointed out to very dramatic shifts within investigated ranges of CMPs, its values revealed relatively good separation of amlodipine and indapamide peaks, while other CMPs needed more detail considerations prior to selection of the optimal conditions. Having in mind that the responses α_{1-2} and $k^{2.36}$ demonstrated different trends upon the influence of investigated factors, it was difficult to define from the response surfaces what would the optimal solution be.

Therefore, numerical multi-objective optimization was performed using the desirability function (*D*) calculation.[11] It is considered that the desired fulfillment of predefined CMAs is reached if the maximal value of *D* is equal to 1, indicating that the compromise solution is met for which all the optimization goals are as close as possible to the predefined goals. For the proposed method, analytical target profile of the method was achieved using the following chromatographic conditions: 10 mM *β*-CD (pH 5.4) and acetonitrile (70:30 volume ratio), 25 °C column temperature, 215 nm detection wavelength, 2 mL min^{-1} flow rate and 10 μL injection volume. In accordance with ICH Q14 concept,[22] measures of quality assurance were further considered in order to prove that CMAs will be reached under these conditions with appropriate probability and therefore model coefficients uncertainty were discussed. Low values of standard errors of model coefficients (varying from model to model in range –0.026–0.090) and low correlation of residuals for all regression models (0.182, 0.093 and 0.091, respectively) were noted thus proving appropriate regression model quality.

The verification chromatogram was recorded both with mixture of reference substances and sample solution under selected optimal chromatographic conditions with a total analytical run time within three min, as shown in Fig. 4.

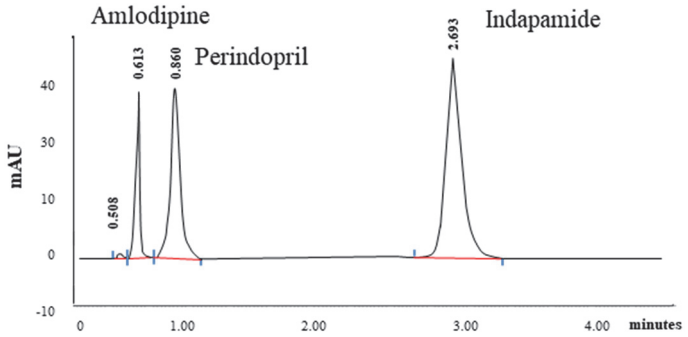

Fig. 4. Representative HPLC chromatogram recorded using mobile phase composed of 10 mM *β*-CD (pH 5.4) and acetonitrile (70:30 volume ratio).

System suitability test parameters were further evaluated: the asymmetry factor (*As*) meeting the acceptance criteria $0.8 < As < 1.5$, the number of theoretical plates (*N*) greater than 2000 and appropriate system precision expressed as percent relative standard deviation value (*RSD*) being lower than 1 % (Table IV). The HPLC method was validated to prove its suitability for intended use, the quality control of commercially available tablets. Method linearity and range, precision, repeatability and accuracy were tested following the procedure required by ICH guideline.[23] From the data shown in Table IV, it may be seen that all validation parameters met appropriate acceptance criteria. Method linearity was demonstrated by the value of calculated correlation coefficient being greater than 0.998.

The *RSD* values indicated good method repeatability and intermediate precision since they were lower than 2 and 3 % in average, respectively. Average percent Recovery values calculated for 3 concentration levels were in range 98–102 % indicating good method accuracy.

Table IV. Results of method validation and system suitability tests

Parameter	Amlodipine besylate	Perindopril erbumine	Indapamide
Asymmetry factor	1.33	1.45	1.36
Number of theoretical plates	4150	5907	4856
System precision, *RSD* / %	0.39	0.72	0.12
Linearity range, μg mL^{-1}	25–75	10–30	3.125–9.325
Correlation coefficient	0.9997	0.9991	0.9993
Repeatability, *RSD* / %	1.35	1.25	1.77
Intermediate precision, *RSD* / %	1.41	1.30	1.56
Accuracy (Recovery, %)	98.53	99.32	100.01

In order to evaluate HPLC method greenness and sustainability profile, the assignment of penalty points to every step of the analytical procedure was performed in the accordance with the procedure of calculating AGREE score.[12,13] In that respect, acetonitrile present in the mobile phase was labeled as danger and so appropriate penalty points were taken. In contrast, *β*-CD was considered safe. Then, it was noted that none of the chemicals used exceeded the amount of 20 mL per analysis. Afterwards, energy consumption was considered. HPLC instruments commonly use more than 1.5 kWh or less than 0.5 kWh of electrical currency per sample, and therefore penalty points are assigned to this technique. The PDA detector was used, which takes less than 0.5 kWh of electrical energy per sample. The generated waste was collected and it is possible to be recycled. HPLC system used is hermetically closed system. Therefore, penalty points accounting for produced waste are assigned only on the basis of its amount. The positioning of the analytical instrument was also taken into consideration, which is an inline analysis. This adds to greenness points as there's is elimination of manual sampling and reduction of waste. Considering all mentioned, the final AGREE score obtained was 0.7 (Fig. 5) which is higher compared to the values obtained from similar studies analyzing

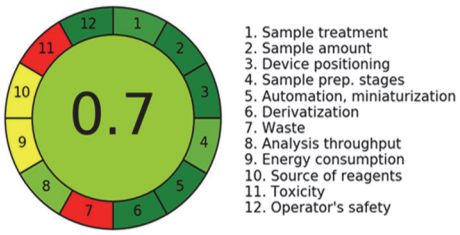

Fig. 5. AGREE greenness assessment results.

the same three APIs (0.45 and 0.5).[14,15] This method is therefore declared as far superior in its eco-friendliness.

CONCLUSION

Understanding that in recent times there is a need to develop analytical procedures for the drug analysis which are sustainable and eco-friendly is of outmost importance. The contribution of every stakeholder in the industry is much needed towards the achievement of the sustainable development goals, in this regard the present work is the kind contribution of the authors to develop a new greener and sustainable HPLC method for the analysis of perindopril, amlodipine and indapamide in a ternary mixture. The method has AGREE score 0.7 indicating the most compliant profile to sustainability and GAC principles compared to previous reports.

Acknowledgement. The research was funded by the Ministry of Science, Technological Development and Innovation, Republic of Serbia through Grant Agreements with University of Belgrade Faculty of Pharmacy, No. 451-03-33/2026-03/200161 and 451-03-34/2026-03/ /200161.

И З В О Д

ПРИМЕНА ПРИНЦИПА ЗЕЛЕНЕ ХРОМАТОГРАФИЈЕ У АНАЛИЗИ СМЕШЕ ПЕРИНДОПРИЛА, АМЛОДИПИНА И ИНДАПАМИДА КОРИШЋЕЊЕМ *β*-ЦИКЛОДЕКСТРИНА КАО МОДИФИКАТОРА МОБИЛНЕ ФАЗЕ

ХУСЕИНАТУ ОСМАН, ЈЕВРЕМ СТОЈАНОВИЋ, АНА ПРОТИЋ, МИРА ЗЕЧЕВИЋ и БИЉАНА ОТАШЕВИЋ

Катедра за аналитику лекова, Универзитет у Београду – Фармацеутски факултет, Војводе Степе 450, 11221 Београд

Подизање нивоа еколошке свести у домену развоја метода течне хроматографије је неопходно, при чему употреба *β*-циклодекстрина као адитива мобиле фазе представља релативно новију стратегију која обећава. Овај рад приказује развој методе усаглашен са захтевима ICH Q14 смернице за сагледавањем одрживости и управљањем животним циклусом методе, са циљем да се обезбеди хроматографска анализа вишекомпоненте таблетне формулације која се користи у терапији кардиоваскуларних болести. Најпре је дефинисан жељени профил методе, постизање добре раздвојености пикова периндоприла, амлодипина и индапамида у што краћем времену, а затим је урађена анализа ризика које је указала да компоненте мобиле фазе представљају критичне параметре методе који утичу на ток хроматографске анализе. Методологија дизајна експеримената и израчунавање функције пожељних одговора, искоришћени су за истовремену оптимизацију нивоа концентрације раствора *β*-циклодекстрина, pH вредности и удела ацетонитрила у мобилној фази који су испитивани у опсезима редом 5–15 mM, 4,0–6,0 и 20–30 запр. %. Оптимални хроматографски услови укључивали су: 10 mM раствор *β*-циклодекстрина (pH 5,4) и ацетонитрил у запреминском односу 70:30 при протоку од 2 mL min^{-1}, RP-18e колону загрејану на 25 °C, таласну дужину детекције од 215 nm и запремину узорка од 10 μL. Процена еколошке прихватљивости методе помоћу AGREE алата је потврдила да је успешно развијена зелена и одржива хроматографска метода.

(Примљено 4. децембра 2025, ревидирано 6. фебруара, прихваћено 11. марта 2026)

REFERENCES

1. P. Anastas, *Crit. Rew. Anal. Chem.* **29** (2010) 167 (https://doi.org/10.1080/10408349891199356)
2. W. Löscher, *Front. Pharmacol.* **12** (2021) 730257 (https://doi.org/10.3389/fphar.2021.730257)
3. J. J. Lu, W. Pan, Y. J. Hu, Y. T. Wang, *PLOS One* **7** (2012) 40262 (https://doi.org/10.1371/journal.pone.0040262)
4. S. Julius, J. N. Cohn, J. Neutel, M. Weber, P. Turlapaty, Y. Shen, V. Dong, A. Batchelor, H. Lagast. *J. Clin. Hypertens.* **25** (2007) 10 (https://doi.org/10.1111/j.1524-6175.2004.02440.x)
5. T. Godfraind, *J. Cardiovasc. Pharmacol. Ther.* **19** (2014) 501 (https://doi.org/10.1177/1074248414530508)
6. D. B. Campbell, *Curr. Med. Res. Opin.* **8** (1983) 9 (https://doi.org/10.1185/03007998309109832)
7. United Nations General Assembly, *Transforming our world: the 2030 Agenda for Sustainable Development*, A/RES/70/1 (2015) (https://docs.un.org/en/A/res/70/1)
8. M. Yabré, L. Ferey, I. T. Somé, K. Gaudin, *Molecules* **23** (2018) 1065 (https://doi.org/10.3390/molecules23051065)
9. S. El Deeb, *Molecules* **29** (2024) 3205 (https://doi.org/10.3390/molecules29133205)
10. J. Stojanović, J. Krmar, B. Otašević, A. Protić, *Arh. Farm.* **73** (2023) 146 (https://doi.org/10.5937/arhfarm73-43479)
11. N. Đajić, J. Krmar, J. Stojanović, B. Svrkota, B. Otašević, A. Malenović, A. Protić, *Arh. Farm.* **74** (2024) 235 (https://doi.org/10.5937/arhfarm74-49572)
12. F. Pena-Pereira, W. Wojnowski, M. Tobiszewski, *Anal. Chem.* **92** (2020) 10076 (https://doi.org/10.1021/acs.analchem.0c01887)
13. L. A. Yahya, C. Vakh, O. Dushna, O. Kalisz, S. Bocian, M. Tobiszewski, *Anal. Chim. Acta* **1357** (2025) 344052 (https://doi.org/10.1016/j.aca.2025.344052)
14. K. Patel, *Sep. Sci. Plus* **3** (2020) 175 (https://doi.org/10.1002/sscp.202000010)
15. K. N. Prashant, Y. Pragathi, S. Yenduri, *Green Anal. Chem.* **12** (2024) 100182 (https://doi.org/10.1016/j.greeac.2024.100182)
16. S. Agatonović-Kustrin, M. Lebete, M. E. Brown, D. W. Morton, B. Glass, *J. Serb. Chem. Soc.* **81** (2016) 1037 (https://doi.org/10.2298/JSC150915018A)
17. V. González-Ruiz, A. G. León, A. I. Olives, M. A. Martín, J. C. Menéndez, *Green Chemistry* **13** (2011) 115 (https://doi.org/10.1039/C0GC00456A)
18. N. Maljurić, J. Golubović, B. Otašević, M. Zečević, A. Protić, *Anal. Bioanal. Chem.* **410** (2018) 2533 (https://doi.org/10.1007/s00216-018-0911-3)
19. U. A. Thorsteinsdóttir, M. Thorsteinsdóttir, *J. Mass Spectrom.* **56** (2021) 4727 (https://doi.org/10.1002/jms.4727)
20. S. N. Hidayah, M. Mazidatu lakmam, S. M. F. Bukhari, R. N. Yani, *J. Serb. Chem. Soc.* **90** (2025) 1203 (https://doi.org/10.2298/JSC250124062S)
21. B. Svrkota, J. Krmar, F. Petronijević, A. Protić, B. Otašević, *J. Sep. Sci.* **48** (2025) 70136 (https://doi.org/10.1002/jssc.70136)
22. European medicinal agency, *ICH Q14 Guideline on analytical procedure development* (2023) (https://www.ema.europa.eu/en/ich-q14-analytical-procedure-development-scientific-guideline)
23. European medicinal agency, *ICH Q2(R2) Guideline on validation of analytical procedures* (2024) (https://www.ema.europa.eu/en/ich-q2r2-validation-analytical-procedures-scientific-guideline).

Journal of the Serbian Chemical Society
JSCS-info@shd.org.rs • www.shd.org.rs/JSCS
J. Serb. Chem. Soc. 91 (6) 603–616 (2026)
JSCS–5513
Original scientific paper
Published 2 July, 2026

Epoxy- and cyclopropane-functional copolymers: Synthesis, thermal properties and photocrosslinking behavior

VUSALA VAHABOVA*, KAZIM GULIYEV and ESFIRA ISKENDEROVA

Institute of Polymer Materials, Ministry of Science and Education of the Azerbaijan Republic, Sumgait, AZ5004, Azerbaijan

(Received 13 February, revised 23 March, accepted 21 April 2026)

Abstract: Copolymers bearing both epoxy and cyclopropane groups were synthesized by free-radical copolymerization of glycidyl 2-(4-vinylphenyl)cyclopropanecarboxylate (GVPCC) with methyl methacrylate (MMA) using AIBN at 343 K, in bulk and in benzene under inert atmosphere. Copolymer compositions were determined by spectroscopy and copolymerization parameters were evaluated by the Fineman–Ross method. The reactivity ratios were r_1(GVPCC) = = 0.68±0.05 and r_2(MMA) = 0.51±0.07; their product (r_1r_2 = 0.35) indicates random copolymerization with a tendency toward alternation. Alfrey–Price parameters (Q_1 = 0.96, e_1 = −0.63; Q_2 = 0.74, e_2 = 0.40) confirm strong comonomer interactions and pronounced polar effects. For a 50/50 copolymer, the intrinsic viscosity was 0.66 dL g^{-1} (benzene, 25 °C). Thermogravimetric analysis showed composition-dependent stability with T_5 250–320 °C, increasing with GVPCC content, alongside improved adhesion (up to 5.6 MPa) and Vicat softening temperature (121 °C). UV irradiation produced efficient crosslinking and negative-tone photoresist behavior (resolution with depth of penetration, D_p 0.25–0.35 μm; critical exposure energy, E_c, 14.5–16.4 mJ cm^{-2}; sensitivity, S, 61–69 cm^2 J^{-1}), demonstrating potential for UV-patternable microfabrication materials.

Keywords: cyclopropane ring; epoxy functionality; UV-induced crosslinking; negative-tone photoresist; working curve.

INTRODUCTION

As modern microelectronic technologies continue to advance, there is a growing demand for new functional polymeric materials with improved performance characteristics. Owing to their high thermal endurance, specific electrophysical properties and favorable deformation–strength behavior, such polymers are widely regarded as indispensable materials for forming protective and insulating layers in the fabrication of microelectronic devices.[1–6]

* Corresponding author. E-mail: vusalavahabova@gmail.com
https://doi.org/10.2298/JSC260213023V

High-resolution topological patterns in polymer films are typically produced by optical photolithography. In practice, two main strategies are used: either complex multilayer resist systems are employed, or the intrinsic photosensitivity of the polymer is exploited. Introducing built-in photosensitivity into the polymer matrix is considered the more promising approach, since it can significantly simplify processing and enhance the lithographic resolution. However, a persistent limitation remains: most currently available resists exhibit insufficient photosensitivity, which becomes a serious technological bottleneck.

To address this challenge and improve the lithographic performance of negative-tone photoresists, the synthesis of new monomers containing photoactive groups – and the preparation of polymers based on these monomers – remains a highly relevant task. In our earlier studies, the photochemical behavior of difunctional substituted cyclopropylstyrenes was investigated.[7] The present work represents a logical continuation of those efforts and is focused on the radical copolymerization of an epoxicarbonyl-substituted cyclopropylstyrene monomer, glycidyl 2-(4-vinylphenyl) cyclopropanecarboxylate (GVPCC), with methyl methacrylate (MMA).

Although the photochemical properties of cyclopropyl-containing styrene derivatives have been explored previously,[8–12] the combined incorporation of an epoxy functional group together with the cyclopropane fragment and, importantly, its potential synergistic contribution to photosensitivity, has not been systematically examined. Here, we investigate this effect for the first time.

The main objective of this study is to elucidate the copolymerization behavior of GVPCC and to systematically evaluate how the epoxicarbonyl substituent introduced into the cyclopropane fragment of the side chain influences the photosensitivity of the resulting macromolecules. The GVPCC monomer can be considered a promising starting material for producing polymers with properties valuable for microelectronic applications and, consequently, exhibits substantial potential for further practical use.

EXPERIMENTAL

The target monomer, glycidyl 2-(4-vinylphenyl)cyclopropanecarboxylate (GVPCC), was synthesized *via* the reaction of 2-(4-vinylphenyl)cyclopropanecarboxylic acid with epichlorohydrin (EClH) under basic conditions.

The synthesis was carried out by treating the acid with excess epichlorohydrin in the presence of sodium hydroxide, which facilitated the formation of the glycidyl ester through nucleophilic substitution and subsequent ring closure. The reaction proceeds *via* the intermediate chlorohydrin, followed by intramolecular cyclization to yield the epoxide-containing monomer.[13]

The overall synthetic route is presented in Scheme 1. The purity of the monomer was verified by gas chromatography (GC) and was found to be 99.8 %.

Copolymerization procedure

To evaluate the reactivity of the synthesized monomer and its potential for practical applications, it was subjected to radical copolymerization with methyl methacrylate (MMA). MMA, 99 % (Sigma–Aldrich) was used as received. The copolymerization of GVPCC with MMA was

carried out both in bulk and in benzene solution under a nitrogen atmosphere in sealed glass ampoules.

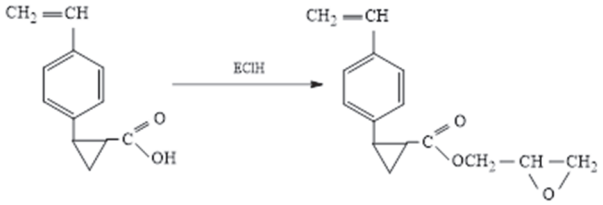

Scheme 1. Synthesis of glycidyl 2-(4-vinylphenyl)cyclopropanecarboxylate (GVPCC).

After mixing the monomers with the initiator (azobisisobutyronitrile AIBN, 98 % Sigma–Aldrich was used as received), the reaction mixture was transferred into a glass ampoule. The mixture was purged with nitrogen for 8 min, after which the ampoule was tightly sealed and maintained in a thermostat at 343 K. The initiator concentration was 0.3 wt. % relative to the total monomer mass.

The resulting polymer was purified from benzene solution by double reprecipitation into methanol and then dried under vacuum at 30 °C to constant mass at a residual pressure of 15–20 mmHg. Benzene (99.5 %, Sigma–Aldrich) and methanol (99.8 %, Sigma–Aldrich) were used as received. Yield: 259 mg (83 %, based on the total mass of monomers). The intrinsic viscosity of the copolymers was measured in benzene at 25 °C using an Ubbelohde-type viscometer. The radical copolymerization of GVPCC with methyl methacrylate (MMA) initiated by AIBN is shown in Scheme 2.

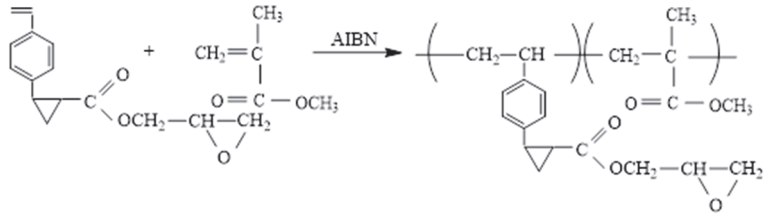

Scheme 2. AIBN-initiated radical copolymerization of GVPCC with methyl methacrylate (MMA).

Characterization of the copolymers

^{1}H-NMR spectra were recorded on a Bruker AFR-300 spectrometer (300 MHz) in $CDCl_3$ using tetramethylsilane (TMS) as the internal standard; chemical shifts are reported in ppm (δ) and coupling constants in Hz (J). FT-IR spectra were recorded on a Bruker Alpha FT-IR spectrometer (Germany). UV–Vis spectra were obtained on a Shimadzu UV-1800 spectrophotometer in the 200–400 nm range. Thermogravimetric analysis (TGA) was performed under nitrogen on a NETZSCH TG 209 F3 Tarsus thermal analyzer at a heating rate of 10 °C min^{-1}.

Adhesion strength was determined by the pull-off method according to ISO 4624 using an Elcometer 510 adhesion tester. Measurements were carried out on polymer films deposited on glass plates at 23±2 °C with a loading rate of 1 MPa s^{-1}. The Vicat softening temperature was determined according to ISO 306 (method B50) using a Vicat softening point apparatus at a heating rate of 50 °C h^{-1} under a load of 50 N. Tensile properties, including tensile strength and elongation at break, were measured on a ИМ-4P (IM-4R) universal testing machine, АКІМ-

-Metal, Russia, in accordance with ISO 527-2 at 23 °C and a crosshead speed of 10 mm min^{-1}. Impact resistance was evaluated by the Charpy method according to GOST 4647 using a MJI-09 pendulum impact tester (Tochpribor, Russia) at room temperature.

Method for evaluating the photosensitivity of the synthesized polymers

Photoresist solutions containing the copolymers (4–13 wt. %) were prepared in benzene and spin-coated onto glass substrates at 2500 rpm. Film thickness after drying (room temperature followed by vacuum drying at 50 °C) was 0.20–0.25 μm (Linnik microinterferometer). UV exposure through a photomask was carried out using a DRT/DPT-220 mercury lamp (2.2 A, 15 cm distance, 5–25 s), followed by development in dioxane:isopropyl alcohol (1:2 volume ratio) at 18–25 °C. Negative-tone behavior was confirmed by the insolubility of exposed areas in the developer. The surface exposure dose was calculated as:

$$E_o = It \tag{1}$$

The critical exposure energy (E_c) and penetration depth (D_p) were obtained from the working curve:

$$C_d = D_p \ln(E_o / E_c) \tag{2}$$

where D_p is determined from the slope and E_c from the x-intercept.

RESULTS AND DISCUSSION

Characterization of the copolymers

The structure of the GVPCC–MMA copolymers synthesized in this work was supported by FTIR and ^{1}H-NMR spectroscopy. In the FTIR spectrum of the GVPCC monomer, the characteristic absorption bands of the vinyl group are clearly observed at 1630 and 990 cm^{-1}. After polymerization, the vinyl-group bands disappeared in the copolymer, indicating consumption of the double bond, while the intense bands assigned to the cyclopropane ring (1030–1035 cm^{-1}), the ester carbonyl group (1735 cm^{-1}) and the epoxide ring (910 and 1250 cm^{-1}) remain preserved. The FTIR spectrum of the GVPCC/MMA copolymer is shown in Fig. 1.

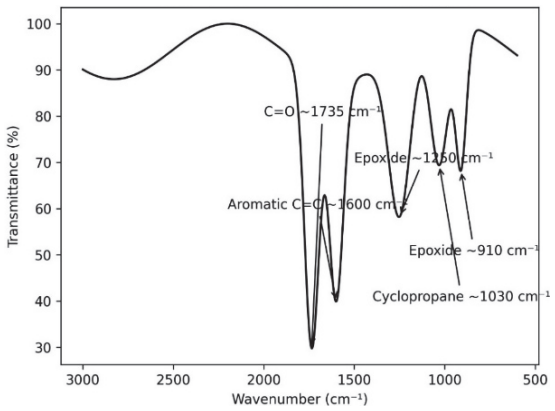

Fig. 1. FTIR spectrum of the GVPCC/MMA copolymer.

A similar spectral pattern is observed for the copolymer. However, incorporation of MMA leads to an increase in both the intensity and the breadth of the ester carbonyl (C=O) absorption band in the 1725–1735 cm^{-1} region. This effect can be attributed to the overlap of carbonyl absorptions from two different ester functionalities present in the copolymer structure.

Comparative ^{1}H-NMR analysis

Comparative ^{1}H-NMR analysis was used to determine the macromolecular composition. In the GVPCC monomer, the vinyl protons give distinct signals in the δ 5.2–6.7 ppm region. In the homopolymer, these signals were absent, demonstrating that polymerization proceeds *via* the vinyl double bond. The ^{1}H-NMR spectrum of the GVPCC/MMA copolymer is shown in Fig. 2. The protons of the cyclopropane ring were observed at δ 1.2–1.8 ppm, while the epoxide-ring protons were detected in the δ 2.6–3.2 ppm range.

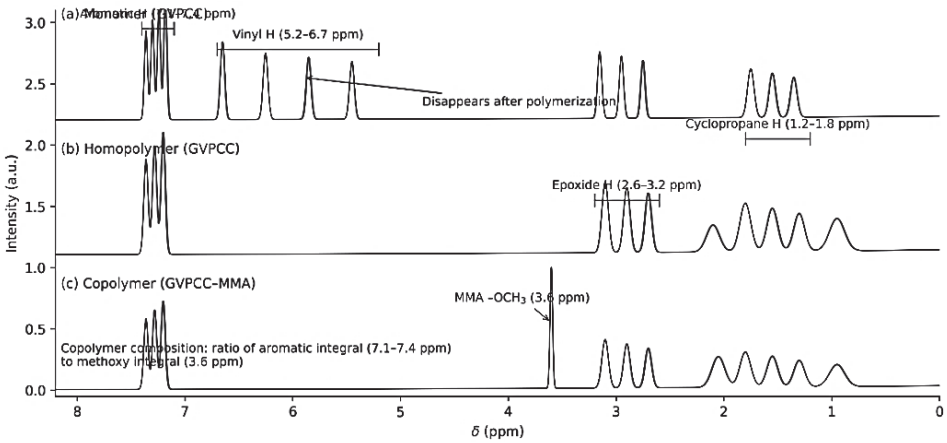

Fig. 2. Comparative ^{1}H-NMR spectra of the GVPCC monomer, its homopolymer and the GVPCC/MMA copolymer ($CDCl_3$, 300 MHz).

In the copolymer spectrum, the signals characteristic of the GVPCC-derived units are retained and, in addition, a sharp singlet at δ = 3.6 ppm corresponding to the methoxy (–OCH_3) group of the MMA fragment appears. The mole ratio of the comonomer units in the copolymer was determined from the integral intensity ratio of the aromatic protons of GVPCC (δ 7.1–7.4 ppm) to the methoxy protons of MMA.

Copolymer composition and reactivity ratios

Copolymerization was carried out at various initial molar feed ratios of GVPCC and MMA. The composition of the resulting copolymers was determined by ^{1}H--NMR spectroscopy based on the integral intensity ratio of the aromatic protons of the GVPCC units (δ 7.1–7.4 ppm) to the methoxy group of MMA (δ 3.6 ppm). It

was found that increasing the fraction of GVPCC in the initial feed led to a proportional increase in the content of epoxicarbonyl and cyclopropane fragments incorporated into the macromolecular chain.

To better understand the copolymerization behavior of the GVPCC/MMA system, the reactions were performed both in bulk and in benzene solution. Bulk polymerization made it possible to assess the behavior of the monomer pair in the absence of solvent, whereas solution polymerization in benzene provided lower viscosity and improved heat transfer, allowing better control of the reaction conditions. The obtained copolymerization results confirmed that GVPCC and MMA undergo efficient copolymerization, as reflected by the reactivity ratios r_1 = = 0.68±0.05 and r_2 = 0.51±0.07. Since both values are below unity and the product $r_1 r_2$ = 0.35, the system shows a tendency toward cross-propagation and partial alternation. Thus, the use of both bulk and solution conditions was helpful for evaluating the effect of the reaction medium on the copolymerization behavior and on the properties of the resulting copolymers.

As a quantitative characteristic of copolymerization, the relative reactivity of the monomers (reactivity ratios) was calculated using the Fineman–Ross method.[14] The compositions of GVPCC (M_1)/MMA (M_2) copolymers obtained at different initial feed ratios were determined by ^{1}H-NMR spectroscopy, and the results are summarized in Table I. The dependence of the copolymer composition on the initial monomer feed was well described by the Mayo–Lewis equation,[15] showing good agreement with the experimental data.

TABLE I. Copolymer composition (mol %) for the GVPCC/MMA system

Sample No.	M_1 in feed	M_2 in feed	m_1 in copolymer	m_2 in copolymer
1	90	10	87.1	12.9
2	75	25	72.2	27.8
3	50	50	52.7	47.3
4	25	75	32.7	67.3
5	10	90	16.1	83.9

Fig. 3 illustrates the relationship between the initial monomer feed composition (M_1) and the resulting copolymer composition (m_1) for the GVPCC/MMA copolymerization system. The deviation of the experimental points from the ideal $y = x$ line indicates the occurrence of compositional drift during copolymerization and reflects differences in monomer reactivity during radical chain propagation. At low M_1 values, the fraction of monomer 1 in the copolymer is relatively higher ($m_1 >$ $> M_1$), whereas at higher M_1 the data approach the ideal line ($m_1 \approx M_1$). These observations are consistent with reactivity ratios lower than unity ($r_1 < 1$ and $r_2 <$ < 1) suggesting a preference for cross-propagation in the system and indicating a certain tendency toward alternating incorporation.

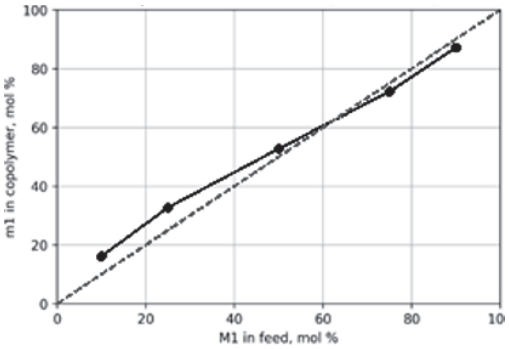

Fig. 3. Copolymer composition diagram for GVPCC/MMA: variation of m_1 as a function of the feed fraction M_1.

Based on the Fineman–Ross analysis, the reactivity ratios were determined as $r_1 = 0.68 \pm 0.05$ for GVPCC and $r_2 = 0.51 \pm 0.07$ for MMA. Since both ratios are below unity ($r_1 < 1$ and $r_2 < 1$), each propagating radical preferentially adds the other monomer during chain growth. The fact that $r_1 > r_2$ indicates that the GVPCC-derived radical is more selective than the MMA-derived radical. Moreover, the product $r_1 r_2 = 0.35$, which is significantly lower than 1, suggests that the copolymerization exhibits a tendency toward alternating incorporation on an otherwise statistical background.

To ensure reliable determination of the reactivity ratios (r_1 and r_2), copolymerization experiments were performed at low conversion (8–10 %), and the reactions were quenched at this stage to minimize composition drift.

Copolymer with a GVPCC:MMA feed mole ratio of 50:50 exhibited an intrinsic viscosity [η] of 0.66 dL·g^{-1}.

To assess the electronic and structural characteristics of the monomers, the Alfrey–Price scheme[16] was applied to determine the Q and e parameters. For the GVPCC/MMA system, the reactivity ratios (r_1 and r_2) obtained at low conversion were used. The literature Q and e values for MMA were treated as fixed constants, and the Q and e parameters of GVPCC were back-calculated using the Alfrey–Price equations. For GVPCC, the values $Q = 0.96$ and $e = -0.63$ were obtained.

Compared with the commonly accepted literature values for MMA ($Q = 0.74$, $e = 0.40$) the higher Q value of GVPCC suggests enhanced resonance stabilization of the vinyl group, promoted by the aromatic ring and the cyclopropane fragment. The negative e parameter (−0.63) reflects the predominance of resonance effects that increase electron density in the monomer. Overall, these results indicate that GVPCC exhibits moderate reactivity and copolymerizes efficiently with MMA. The calculated parameters are summarized in Table II.

The thermal behavior of the synthesized GVPCC/MMA copolymers was investigated by thermogravimetric analysis (TGA). The TGA data indicate that thermal degradation proceeds through multiple steps. The initial weight-loss temperature (T_5, corresponding to 5 % mass loss) was observed in the 250–320 °C

range depending on the copolymer composition: for GVPCC/MMA = 90/10, T_5=320 °C; for 75/25, T_5 = 305 °C; for 50/50, T_5 = 290 °C; for 25/75, T_5 = 280 °C; for 10/90, T_5 = 250 °C (Fig. 4). These results demonstrate that increasing the GVPCC fraction enhances the thermal stability of the copolymers and confirms that the materials possess sufficiently high thermal resistance for microelectronic processing.

TABLE II. Monomer reactivity ratios and Alfrey–Price Q–e parameters for the GVPCC/MMA copolymerization system. Q_2 and e_2 values for MMA were taken from the literature; Q_1 and e_1 for GVPCC were back-calculated using the Alfrey–Price scheme and the experimentally determined reactivity ratios

System	Method	r_1 (GVPCC)	r_2 (MMA)	r_1r_2	Q_1	e_1	Q_2 (MMA)	e_2 (MMA)
GVPCC/MMA	Fineman–Ross	0.68±0.05	0.51±0.07	0.35	0.96	–0.63	0.74	0.40

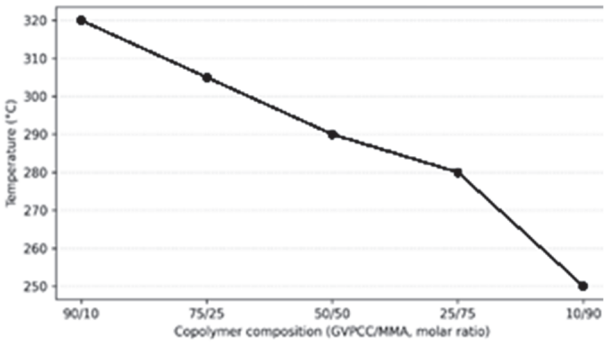

Fig. 4. Thermogravimetric (TGA) profiles of GVPCC/MMA copolymers at various GVPCC:MMA ratios.

The observed improvement in stability can be attributed to strengthened intrachain interactions promoted by the cyclopropane ring and aromatic moieties introduced into the side chains, which can hinder bond scission and slow down the overall decomposition process.

Table III shows that increasing the GVPCC comonomer content leads to a consistent improvement in both the thermal and mechanical performance of the MMA–GVPCC copolymers. When the GVPCC fraction is increased from 25 to 75 mol %, the adhesion strength rises from 2.5 to 5.6 MPa (approximately a 2.24--fold increase). This enhancement can be directly attributed to the structural features of the GVPCC units: the glycidyl epoxy ring and the ester linkage increase the overall polarity of the copolymer, thereby strengthening interfacial interactions with the substrate – particularly on surfaces bearing polar functional groups – through dipole–dipole interactions and hydrogen bonding. As a result, the interfacial bonding becomes more robust, leading to improved adhesion performance.

The Vicat softening temperature, used here as a measure of heat resistance, is also sensitive to the GVPCC content: 110 °C for 25 mol % GVPCC, 117 °C for 50 mol % and 121 °C for 75 mol % (an overall increase of 11 °C). This trend can be attributed to the aromatic vinylphenyl fragment and the cyclopropane ring introduced by GVPCC, which restrict segmental chain mobility. As a result, the softening temperature increases and the material exhibits improved dimensional stability at elevated temperatures.

In terms of mechanical performance, the tensile strength increases from 68 to 80 MPa (approximately +12 MPa, ~18 %). Importantly, this improvement is not achieved at the expense of brittleness; on the contrary, the elongation at break rises from 1.8 to 6.9 % (about a 3.8-fold increase). These results are consistent with a balanced structure–property effect in the copolymer: rigidifying fragments (aromatic and cyclopropane units) enhance strength, while polar functionalities (ester and epoxy groups) promote local intermolecular interactions, enabling more efficient energy dissipation under deformation.

A similar trend is observed for impact resistance: with increasing GVPCC content, the value rises from 152 to 169 $N \cdot cm^{-1}$ (an increase of 17 $N \cdot cm^{-1}$, ~11 %). This improvement is consistent with the higher elongation at break and indicates enhanced resistance to damage under dynamic loading.

Overall, the results summarized in Table III demonstrate that increasing the GVPCC fraction leads to a comprehensive enhancement of the GVPCC/MMA copolymer properties: adhesion, heat resistance, strength, ductility, and impact resistance all improve simultaneously. Although the highest performance is achieved for the sample containing 75 mol % GVPCC, a composition of 50 mol % GVPCC may represent a favorable compromise in terms of the heat-resistance–strength––ductility balance, depending on the intended application.

TABLE III. Effect of GVPCC content (25–75 mol %) in MMA–GVPCC copolymers on adhesion strength, Vicat softening temperature (heat resistance), tensile strength, elongation at break and impact resistance

GVPCC content, M_1 / mol %	Adhesion strength, MPa	Vicat softening temp., °C	Tensile strength, MPa	Elongation at break, %	Impact resistance, N/cm
25	2.5±0.1	110±2	68±3	1.8±0.2	152±5
50	3.2±0.2	117±2	75±3	4.7±0.3	160±4
75	5.6±0.3	121±2	80±2	6.9±0.4	169±5

Values are given as mean ± standard deviation (n = 3). Overall, the data in Table III show a consistent improvement in adhesion, heat resistance, tensile strength, elongation at break and impact resistance with increasing GVPCC content.

Increasing the GVPCC fraction leads to a simultaneous rise in strength and elongation at break, suggesting that the “stiffness–ductility” balance in this system cannot be explained solely by chain rigidification. Rather, it is also associated with

enhanced intermolecular interactions that promote energy dissipation during deformation. The aromatic ring and cyclopropane fragment within the GVPCC unit restrict segmental rotational freedom and therefore act as rigid structural elements that increase the load-bearing capacity (σ). At the same time, the ester (C=O) and epoxy (C–O) functionalities increase the cohesive energy density of the copolymer and can strengthen dipole–dipole attractions between chains, effectively creating physical association points.

In addition, partial epoxy ring opening under processing conditions (*e.g.*, trace moisture or catalytic impurities) is possible, which would generate –OH groups. In such a case, reversible hydrogen bonds of the –OH···O=C and –OH···O– types may form and act as additional "sacrificial" interactions. These dynamic bonds can delay crack propagation and increase damping of mechanical energy during stretching. The synergistic contribution of dipole–dipole interactions and hydrogen bonding has been reported to improve both strength and toughness (energy absorption/elongation) in various polymer systems.[17]

Overall, the rigid fragments introduced by GVPCC (aromatic + cyclopropane) enhance strength, while the polar functionality (ester/epoxy and potentially –OH sites) reinforces dynamic interchain interactions, compensates for embrittlement, and ultimately leads to the balanced mechanical response observed here.

The presence of multiple reactive functionalities of different chemical nature within the synthesized copolymer chains (*e.g.*, epoxy, ether/ester, and cyclopropane fragments) enhances both the photo-reactivity of the material and its potential for further functional modification. These groups can facilitate the formation of crosslinks under UV irradiation and may also serve as "active sites" for subsequent amination or other post-polymerization transformations. The synthesized GVPCC/ /MMA copolymers exhibited efficient UV-induced crosslinking and, according to the insolubility criterion in the developer, showed negative-tone photoresist behavior. A low critical exposure energy (E_c) indicates that network formation can be initiated at a lower energy input, *i.e.*, the material displays high photosensitivity. In this respect, the cyclopropane ring together with the epoxycarbonyl/ester functionalities can be regarded as structural features that promote photochemical conversion and accelerate network formation.

The copolymers also demonstrated high optical transparency ($T \approx 90$ %) which is important for light propagation within the film and for maintaining process stability during photopatterning. In addition, the refractive index $n_D^{20} = 1.583$ can be attributed to the influence of the cyclopropane ring and ester/carbonyl-type groups on polarizability and optical density in the macromolecular environment. Taken together, these characteristics support the potential of the materials as thin-film negative photoresists for applications in microelectronics and optoelectronics.

E_c decreased markedly with increasing copolymer concentration, from ~90 mJ cm^{-2} at 4 wt. % to ~15 mJ cm^{-2} at 13 wt. % (Fig. 5). This trend can be attributed

to the higher concentration of photoactive moieties (epoxy and cyclopropane fragments) in the resist film at elevated polymer loadings, which reduces the minimum energy required to initiate network formation under UV irradiation. Such a concentration-dependent decrease in E_c confirms that the resist becomes more sensitive at higher concentrations and can be viewed as a factor that improves energy efficiency in microelectronic photoprocessing, as illustrated in Fig. 5.

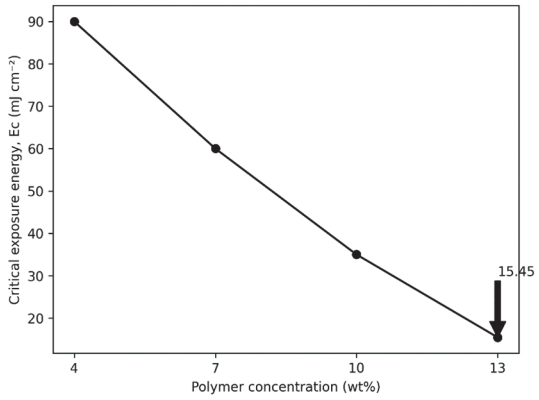

Fig. 5. Dependence of the critical exposure energy (E_c) on the concentration of the GVPCC/MMA copolymer.

The photoreactive behavior of the synthesized copolymer under UV irradiation was investigated by UV–Vis spectroscopy (Fig. 6).

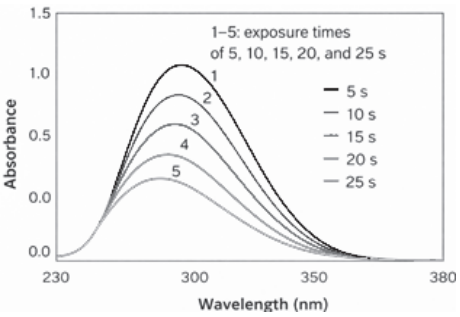

Fig. 6. UV–Vis spectra of the GVPCC/MMA copolymer recorded at different exposure times, showing the change in absorbance intensity.

UV–Vis spectra showed a progressive decrease of the absorption band at 296––300 nm as the exposure time increased from 5 to 25 s, indicating consumption of photoactive fragments and advancement of crosslinking. Similar trends have been reported as a sensitive marker of photopolymerization progress.[18] The combined presence of epoxy and cyclopropane units enhances the photochemical response, which is reflected in the working-curve parameters (E_c and D_p). Under the employed conditions (15 cm distance), 5–25 s exposure was sufficient to obtain stable negative-tone patterns in 0.20–0.25 μm films, as confirmed by optical microscopy.

The measured D_p values (0.25–0.35 μm) are comparable to the film thickness, suggesting that light may penetrate the entire film and cause dose redistribution due to substrate reflection; therefore, thicker films (0.5–1.0 μm) or the use of UV-absorbing additives could improve process robustness. FTIR spectra also support photostructuring, showing a decrease in bands attributed to the epoxide/cyclopropane-related vibrations and the carbonyl group upon irradiation, consistent with network formation. The crosslinking is likely promoted by UV activation of epoxy groups and possible cyclopropane-involving radical processes, resulting in an insoluble 3D network responsible for negative development behavior.

Because the epoxide ring is a highly reactive functional group, it may participate in ring-opening reactions initiated by photo-generated active centers, depending on the formulation and surrounding medium. This interpretation is consistent with the decreased intensity of epoxide-related FTIR bands and supports the assumption that epoxide groups contribute to the crosslinking process. An increased network (gel) density may, in turn, enhance film rigidity and help explain why structuring occurs at relatively low exposure doses (low E_c) in the working-curve analysis (Fig. 7).

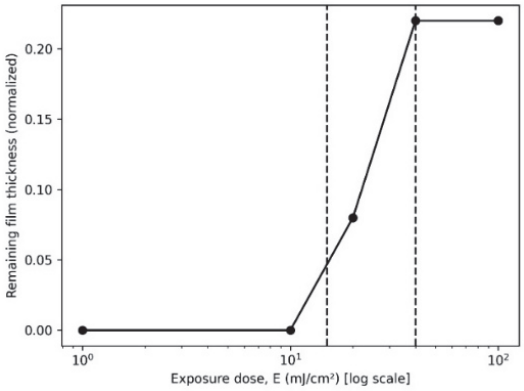

Fig. 7. Working curve of the GVPCC/MMA negative-tone photoresist: remaining film thickness after development (d) as a function of exposure dose (E, mJ/cm^2). The critical dose is E_c = 15.5 mJ/cm^2, and the effective optical penetration depth, D_p, is 0.25–0.35 μm (film thickness: 0.20–0.25 μm).

At the same time, epoxide groups can remain available as reactive sites for amination and other post-polymerization transformations, enabling further post-functionalization of the material.

CONCLUSION

In this work, free-radical copolymerization of the epoxy- and cyclopropane-functional monomer GVPCC with methyl methacrylate (MMA) was carried out, and the composition/structure of the resulting copolymers was confirmed by FTIR and ^{1}H-NMR spectroscopy. Reactivity ratios determined by the Fineman–Ross method were r_1(GVPCC) = 0.68±0.05 and r_2(MMA) = 0.51±0.07 (r_1r_2 = 0.35),

indicating that the system exhibits a tendency toward alternating incorporation on a predominantly statistical copolymerization background.

Thermogravimetric analysis showed that the thermal stability of the copolymers depends on composition: the temperature corresponding to 5 % mass loss (T_5) ranged from 250 to 320 °C and increased with increasing GVPCC content (*e.g.*, 10/90 → 250 °C, 50/50 → 290 °C, 90/10 → 320 °C). Increasing the GVPCC fraction from 25 to 75 mol % resulted in an overall improvement in both thermal and mechanical performance: adhesion strength increased from 2.5 to 5.6 MPa and the Vicat softening temperature rose from 110 to 121 °C. At the same time, tensile strength increased from 68 to 80 MPa without a loss in ductility; instead, elongation at break increased from 1.8 to 6.9 %, accompanied by an increase in impact resistance from 152 to 169 $N \cdot cm^{-1}$.

The copolymers exhibited efficient UV-induced crosslinking and negative-tone photoresist behavior. Working-curve analysis gave D_p 0.25–0.35 μm and E_c 14.5––16.4 $mJ \cdot cm^{-2}$ (S 61–69 $cm^2 \cdot J^{-1}$), confirming the high photosensitivity of the materials. Overall, combining epoxy and cyclopropane functionality provides a promising functional polymer platform for microelectronic applications, offering improved mechanical/thermal properties together with UV patternability.

Acknowledgements. The experimental work (polymer synthesis and characterization) was carried out at the Institute of Polymer Materials, Ministry of Science and Education of the Republic of Azerbaijan (Sumgayit, Azerbaijan). The authors gratefully acknowledge the Institute for access to instrumentation and laboratory facilities.

ИЗВОД

ЕПОКСИ- И ЦИКЛОПРОПАН-ФУНКЦИОНАЛНИ КОПОЛИМЕРИ: СИНТЕЗА, ТОПЛОТНА СВОЈСТВА И ПОНАШАЊЕ ПРИ ФОТОУМРЕЖАВАЊУ

VUSALA VAHABOVA*, KAZIM GULIYEV и ESFIRA ISKENDEROVA

Institute of Polymer Materials, Ministry of Science and Education of the Azerbaijan Republic, Sumgait, AZ5004, Azerbaijan

Кополимери са епоксидним и циклопропанским групама синтетизовани су кополимеризацијом глицидил-2-(4-винилфенил)циклопропанкарбоксилата полимеризацијом слободним радикалима (GVPCC) са метил-метакрилатом (MMA) користећи AIBN на 343 K, у маси и бензену под инертном атмосфером. Састави кополимера су одређени спектроскопијом, а параметри кополимеризације су процењени Fineman–Ross методом. Коефицијенти реактивности су били r_1(GVPCC) = 0,68±0,05 and r_2(MMA) = 0,51±0,07; њихов производ ($r_1 r_2$ = 0,35) указује на статистичку кополимеризацију са тенденцијом ка наизменичној. Alfrey–Price параметри (Q_1 = 0,96, e_1 = −0,63; Q_2 = 0,74, e_2 = 0,40) потврђују јаке интеракције комономера и изражене поларне ефекте. За 50/50 кополимер, интризична вискозност је 0,66 dL g^{-1} (бензен, 25 °C). Термогравиметријска анализа показала је стабилност зависну од састава са T_5 250–320 °C, која се повећава са GVPCC садржајем, уз побољшану адхезију (до 5,6 MPa) и Викатову температуру омекшавања (121 °C). UV зрачење је произвело ефикасно умрежавање и понашање фоторезиста негативног тона (резолуција са дубином пенетрације, D_p, 0.25–0.35 μm; критична енергија излагања, E_c,

14,5–16,4 mJ cm^{-2}; осетљивост, *S*, 61–69 cm^2 J^{-1}), демонстрирајући потенцијал за микрофабрикацију материјала за UV узорке.

(Примљено 13. фебруара, ревидирано 23. марта, прихваћено 21. априла 2026)

REFERENCES

1. Q. Lin, *Polymer* **286** (2023) 126395 (https://doi.org/10.1016/j.polymer.2023.126395)
2. C. Ober, K. Käfer, F. Yuan, Ch., *Polymer* **280** (2023) 126020 (https://doi.org/10.1016/j.polymer.2023.126020)
3. R. Zhou, M. Cao, Y. Tan, M. Neisser, H. Xu, *Sci. Adv.* **11**(29) (2025) 1918 (https://doi.org/10.1126/sciadv.adx1918)
4. Y. Wang, H. Yu, L. Wang, Y. Zhang, Z. Zhu, Y. Zhang, Y. Lu, Ch. Ouyang, *J. Mat. Chem., A* **13** (2025) 29860 (https://doi.org/10.1039/D5TA04194E)
5. Y. J. Wan, G. Li, Y. M. Yao, X. L. Zeng, P. L. Zhu, R. Sun, *Comp. Comm.* **19** (2020) 154 (https://doi.org/10.1016/j.coco.2020.03.011)
6. Y. Wen, C. Chen, Y. Ye, Z. Xue, H. Liu, X. Zhou, Y. Zhang, D. Li, X. Xie, Y. Mai, *Adv. Mat.* **34** (2022) e2201023 (https://doi.org/10.1002/adma.202201023)
7. K. G. Guliyev, G. Z. Ponomareva, Kh. G. Nazaraliyev, A. M. Guliyev, *Azerb. Khim. Zh.* **1** (1999) 87 (in Russian)
8. D. S. Garcia, D. Coto, R. Vicente, *Chem. - Eur. J.* **32(3)** (2025) 1 https://doi.org/10.1002/chem.202503281
9. K.G. Guliyev, S.B. Mamedli, T.S.D. Gulverdashvili, A.M. Guliyev, *Applied Chemistry and Chemical Engineering*, Vol. 2, Apple Academic Press, Palm Bay, FL, 2017
10. A. I. Sadygova, *Azerbaijan Chem. J.* **3** (2022) 45 (https://akj.az/en/journals/949)
11. M. Sayes, G. Benoit, A. B. Charette, *Angew. Chem. Int. Ed.* **57** (2018) 13514 (https://doi.org/10.1002/anie.201807347)
12. K. Mizuno, N. Ichinose, Y. Yoshimi, *J. Photochem. Photobiol., C* **1** (2000) 167 (https://doi.org/10.1016/S1389-5567(00)00011-3)
13. K.G. Guliev, G.Z. Ponomareva, A. M. Guliev, *Vysokomolekulyarnye soedineniya, B* **49** (2007) 1577 (in Russian)
14. M. Fineman, S. D. Ross, *J. Polymer Sci.* **5** (1950) 259 (https://doi.org/10.1002/pol.1950.120050210)
15. F. R. Mayo, F. M. Lewis, *J. Am. Chem. Soc.* **66** (1944) 1594 (https://doi.org/10.1021/ja01237a052)
16. T. Alfrey Jr., C. C. Price, *J. Polymer Sci.* **2** (1947) 101 (https://doi.org/10.1002/pol.1947.120020112)
17. Y. Zhang, Y. Li, W. Liu, *Adv. Funct. Mat.* **25** (2015) 471 (https://doi.org/10.1002/adfm.201401989)
18. J. Bennett, *Addit. Manuf.* **18** (2017) 203 (https://doi.org/10.1016/j.addma.2017.10.009).

Journal of the Serbian Chemical Society
JSCS-info@shd.org.rs • www.shd.org.rs/JSCS
J. Serb. Chem. Soc. 91 (6) 617–630 (2026)
JSCS–5514
Original scientific paper
Published 2 July, 2026

Hydrothermal synthesis of VO_2(B) and its phase transformation to VO_2(M): Investigating metal–insulator transition behavior

AISHWARYA RAJGONDA PATIL,[1] KRISHNA CHAITANYA SOLASA,[1] SOURAV KUMAR,[2] SHREEYA RANE[3] and PALASH ROY CHOUDHURY[4]*

[1]*École Centrale School of Engineering, Mahindra University, Hyderabad, India,* [2]*Department of Metallurgical Engineering and Materials Science, IIT Indore, India,* [3]*Department of Physics, University of Warwick, UK and* [4]*Mahindra University, Survey No: 62/1A, Bahadurpally, Jeedimetla, Hyderabad, Telangana 500043, India*

(Received 1 November, revised 16 December 2025, accepted 22 April 2026)

Abstract: In this study, VO_2(B) nanostructures were synthesized *via* a stabilizer--free hydrothermal route and successfully converted to VO_2(M) at 350 °C in just 30 min. This process offers a reduced thermal budget compared to established protocols, which generally require temperatures above 400 °C and durations exceeding 1 h. The resulting urchin-like VO_2 nanostructures were characterized using a variety of techniques such as XRD, Raman spectroscopy, SEM and DSC to investigate their structural evolution, surface morphology and metal–insulator transition characteristics. The experimental results reveal that VO_2(B) predominantly transforms to VO_2(M) upon annealing at 350 °C, with minor secondary oxide phases. Furthermore, the annealing at 450 °C led to the complete phase transformation of VO_2 to V_2O_5, indicating the sensitivity of VO_2 to annealing temperature. The results show that the insulator-to-metal transition temperature to be ~65 °C, which is lower than that of bulk VO_2 (~68 °C), indicating modified transition behavior in the nanostructured samples. These results demonstrate that hydrothermally synthesized VO_2(B) can be converted to predominantly VO_2(M) by annealing at 350 °C for 30 min, enabling the observation of a reversible metal–insulator transition near 65 °C

Keywords: VO_2 nanostructures; hydrothermal synthesis; annealing effect; metal–insulator transition.

INTRODUCTION

Materials exhibiting a metal–insulator transition (MIT) are used in resistive random-access memory (ReRAM) for non-volatile storage of data. Often this transition accompanies a corresponding change in their crystal structure and symmetry.[1] A transition between crystalline and amorphous phases may be exploited

* Corresponding author. E-mail: palashroychoudhury@gmail.com
https://doi.org/10.2298/JSC251101022P

for use in next-generation non-volatile memory because this transition corresponds to different resistive states.[2] Such materials can mimic neural synapses, which is essential in neuromorphic computing where devices emulate the human brain.[3] A gradual, analog variation in resistance near the MIT provides a means to model synaptic plasticity, achievable with materials that show progressive, voltage-dependent resistance changes.[4] Materials with MIT also hold promise in electronics beyond memory applications. They have the ability to replace conventional transistors in field-effect transistors (FETs), potentially enhancing energy efficiency and making the way for ultra-low-power computing.[5] The sharp MIT in materials like VO_2 at specific temperatures can be used in thermal switches for managing heat flow in electronics.[6] These materials can act as thermal insulators below the transition temperature and as thermal conductors above it. A sharp MIT, which is associated with changes in crystal structure, may also exhibit changes in optical properties.[7] This property may be exploited to construct optical sensors and smart windows that can automatically modulate light of a certain frequency. Oxides undergoing MIT without concurrent magnetic transitions are promising candidates for spin--based quantum applications, where control over electronic phases without perturbing spin order is advantageous.[8] Some materials exhibit a high Seebeck coefficient near the MIT temperature that can be useful for thermoelectric applications.[9] This could enable the development of efficient thermoelectric generators for waste heat recovery, enhancing energy efficiency across various industries.

Materials undergoing an MIT have attracted significant interest due to the abrupt, reversible modulation of their properties. Among these, vanadium dioxide (VO_2) is a premier candidate for next-generation smart windows, thermal switches, and energy-responsive devices. Interest in VO_2 is driven particularly due to its fully reversible structural and electronic transition occurring at a near-ambient temperature of approximately 68 °C.

Vanadium dioxide possesses many possible crystalline forms or polymorphs, some of which are stable, and others metastable. These include VO_2(M), VO_2(R), VO_2(A), VO_2(B), VO_2(C), VO_2(D) and VO_2 (paramontroseite).[10] Out of these, the MIT is associated with the transition between the metallic VO_2(R) phase above 68 °C and the insulating VO_2(M) phase below 68 °C. Many techniques have been used for VO_2 synthesis, including the sol–gel method,[11] magnetron sputtering,[12] chemical vapor deposition[13] and the hydrothermal method.[10,14] Among these, the hydrothermal method is known to have minimal environmental impact and is often employed to synthesize the metastable VO_2(B) phase. Vanadium pentoxide and ammonium metavanadate (NH_4VO_3) are commonly used vanadium sources in the hydrothermal synthesis of VO_2. Commonly used reducing agents include oxalic acid,[15] hydrazine hydrate,[16] ethylene glycol,[17] octadecyl amine,[18] citric acid,[16] formic acid[19] and formaldehyde.[20] Out of these, oxalic acid has been the most preferred reductant in the hydrothermal synthesis of VO_2 due to its low toxicity

and ease of use. Zhu *et al.*[15] reported the synthesis of several types of VO_2(B) nanostructures by a hydrothermal reaction combining (NH_4VO_3) and oxalic acid at different times and temperatures. The resulting products had combinations of nanorods, nanoflakes and nanoflowers with the concentration of oxalic acid influencing their proportions.[15]

In this paper, we report a simple method for the preparation of VO_2(M) *via* heat treatment of hydrothermally derived VO_2(B). The effect of different annealing conditions on the final products was characterized using X-ray diffraction (XRD), Raman spectroscopy, scanning electron microscopy (SEM) and UV–Vis spectroscopy, while the thermochemical properties were studied using differential scanning calorimetry (DSC).

EXPERIMENTAL

Synthesis of VO_2(B)

We synthesized VO_2(B) by a hydrothermal reaction between commercial vanadium pentoxide powder and oxalic acid. Firstly, 0.73 g of V_2O_5 (1 mmol) was added to a beaker containing 40 mL deionized water. This mixture was stirred under ambient conditions for 5 min using a magnetic stirrer. Then, 1.51 g of $H_2C_2O_4 \cdot H_2O$ (3 mmol) was added to it and further stirred for 5 min, yielding a green solution indicating partial reduction. This solution was continuously stirred at 80 °C until the aqueous solution turned into a clear, transparent dark blue color. The change in color implied a reduction of vanadium from V^{5+} to V^{4+}. Then, this solution was transferred into a Teflon®-lined stainless-steel autoclave, which was kept in a preheated oven (at 220 °C) for 3 h to complete the hydrothermal reaction for a duration of 3 h. The resulting bluish-black colored precipitate was separated by centrifugation. This precipitate was then washed with ethanol and DI water several times to remove any contamination and was dried for 12 h at 60 °C in an oven. This yielded black colored vanadium dioxide powder (henceforth referred to as S-22). The resulting powder was subsequently ground in a mortar and pestle and subjected to annealing in a tube-furnace at various temperatures. Fig. 1 illustrates the various steps involved in the synthesis of vanadium oxide nanobelts.

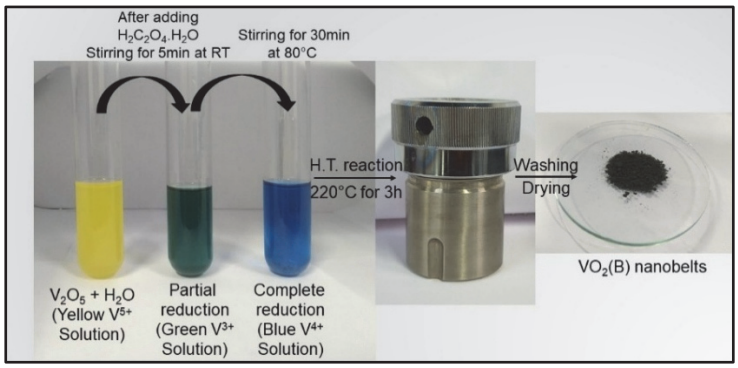

Fig. 1. Schematic illustration of the entire reaction mechanism during hydrothermal synthesis of VO_2 nanobelts.

Synthesis of VO_2(M)

VO_2(M) was derived from VO_2(B) through a controlled annealing process. A 500 mg sample from the as-synthesized VO_2 (S-22) was taken and annealed at different temperatures, namely 300, 350, 400 and 450° C (henceforth addressed as S-30, S-35, S-40 and S-45, respectively) for 30 min in a quartz-tube vacuum furnace under low vacuum (10^{-2} mbar). Both the heating and cooling rates were maintained at 5 °C/min.

Characterization

The crystal structure of the powder samples was characterized by XRD (Rigaku-D/MAX--RB) with CuKα radiation (λ = 0.154 nm). The data were analyzed using SMARTLab software. The samples were scanned over a 2θ range of 15–60°. Additionally, chemical and phase analysis were performed using a Raman spectrometer (Horiba, LabRAM) with a 633 nm laser excitation source. The microstructure and surface morphology of the sample were examined using field--emission SEM (FE-SEM, Jeol). Differential scanning calorimetry (DSC, TA Instruments, model 2910) studies were performed to investigate phase transition behavior over a temperature range of 15–100 °C using heating and cooling rates of 10 °C/min. Optical transmittance measurements were carried out using a UV–Vis spectrometer (Ocean Insights) in the wavelength range of 200–800 nm to evaluate the optical properties of the material.

RESULTS AND DISCUSSION

Structural studies

The crystalline phase and purity of the precursor, as-prepared and annealed samples were determined by XRD and obtained results are shown in Fig. 2. The V_2O_5 spectrum is that of the precursor used for synthesis. The XRD patterns are readily assigned to V_2O_5 (ICDD: 09-0387), which reveals the purity of the precursor. S-22 shows peaks that are in close agreement with the VO_2(B) phase with Miller indices (*hkl* planes) indicating growth of the monoclinic VO_2(B) phase (ICDD: 01-84-7141). The lattice parameter values calculated are as follows: a = = 12.04 Å, b = 3.68 Å and c = 6.43 Å and it shows $C2/m$ space group symmetry, with the strongest peaks at 2θ 25.28, 29.09, 30.13, 37.01, 49.28 and 55.24° corresponding to (110), (002), (111), (202), (11$\bar{3}$) and (221) planes, respectively. Additionally, VO_2(B) also exhibits a high degree of crystallinity, evidenced by the well-defined and strong XRD peaks. The diffraction peak at 2θ 42.2° is indexed to the VO_2(M) phase (ICDD: 01-076-0456) for the (21$\bar{2}$) plane. There is no evidence of diffraction peaks corresponding to secondary oxide phases, such as V_2O_5. These results confirm that the VO_2(B) phase is predominant, with no secondary oxides detected within XRD resolution limits. S-30 remains predominantly VO_2(B), with trace reflections indicating the onset of the phase transition to VO_2(M).

From the analysis of the XRD data, we observe that annealing the sample S-35 at 350 °C resulted in the formation of a predominantly monoclinic VO_2(M) phase, with minor secondary phases of V_2O_5 and V_3O_7. The lattice constants are a = 5.75 Å, b = 4.54 Å and c = 5.38 Å, indicating a monoclinic structure with $P2_1/c$ space group symmetry. The peaks detected at 2θ 27.79, 37.01, 39.72, 42.20, 51.24, 55.45

and 57.33° are assigned to the (001), ($21\bar{1}$), (020), ($21\bar{2}$), ($22\bar{1}$), (220) and (022) planes, respectively, for the monoclinic VO_2(M) phase (ICDD: 01-076-0456).

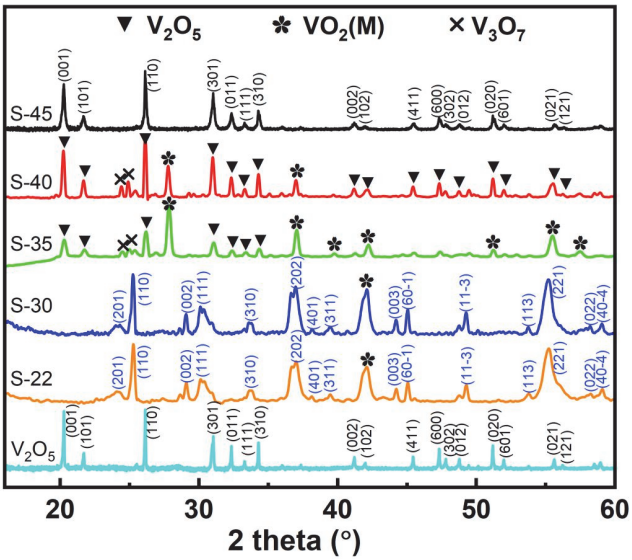

Fig. 2. XRD patterns of pristine V_2O_5, the hydrothermally synthesized sample (S-22) and samples annealed at various temperatures (S-30, S-35, S-40 and S-45) for 30 min.

The XRD patterns of sample S-40 are a combination of phases with the presence of both VO_2 (M) and peaks belonging to V_2O_5 and V_3O_7 (ICDD: 042-0876). It can be noted that with the increase in annealing temperature, the intensities of the peaks of VO_2(M) decrease while the intensities of the V_2O_5 peaks increase, showing reduced thermal stability of the VO_2 phase at elevated temperatures. In contrast, the XRD spectra of S-45 show complete oxidation of VO_2 to V_2O_5, which agrees well with existing literature.[21,22] This indicates that during high-temperature treatment, metastable VO_2 may have oxidized and transformed into its most thermodynamically stable phase, V_2O_5 (ICDD: 09-0387), which is the same as the precursor used for VO_2 synthesis. The average crystallite sizes estimated using Scherrer's formula for samples S-22, S-30, S-35, S-40 and S-45 are 19, 22, 24, 31 and 31 nm, respectively.

Raman spectroscopy was used to analyze the structural and phase information in addition to XRD. Raman spectra of S-22, the precursor V_2O_5 and the annealed samples are shown in Fig. 3a and b. Characteristic peaks at 146 and 197 cm^{-1} are consistent with orthorhombic V_2O_5, indicating high purity and crystallinity of the precursor. The Raman modes at 285 and 406 cm^{-1} correspond to the bending modes of V=O bonds, and the one at 482 cm^{-1} is attributed to the bending of

V–O–V bonds. The peaks at 528 and 701 cm^{-1} are attributed to V–O bonds (combined stretching and bending vibrations). The 995 cm^{-1} peak arises from the stretching of the V=O bond.[23–25]

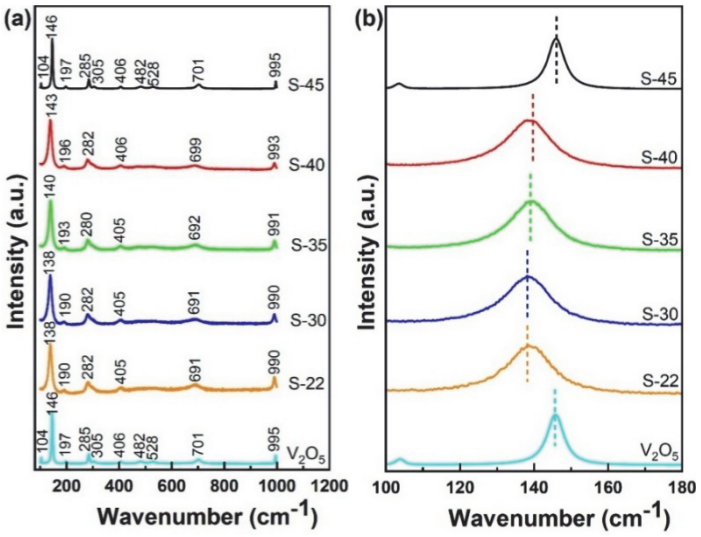

Fig. 3. Raman spectra of all samples: a) full spectra and b) Raman spectra in the range of 135–150 cm^{-1} highlighting the peak shift.

Furthermore, the Raman spectrum of the hydrothermally synthesized VO_2(B) phase (S-22) exhibits broad peaks at 138, 190, 282, 405, 691 and 990 cm^{-1}. The peaks at 138 and 282 cm^{-1} are attributed to V–O–V bending vibrations, while the 405 cm^{-1} peak corresponds to V–O–V stretching. The band at 691 cm^{-1} is associated with the coordination of three oxygen atoms around a vanadium center, and the strong peak at 990 cm^{-1} arises from V=O stretching vibrations. According to Cheng *et al.*[26] and Zhang *et al.*,[27] the above Raman peaks can be indexed to vibrational bands of the VO_2(B) phase.

The sample S-30 exhibits characteristics similar to VO_2(B), indicating the stability of the phase up to this temperature. For the samples S-35 and S-40, we observe a shift in peaks to higher frequencies (140, 280 and 692 cm^{-1}), indicating the formation of mixed phases and partial oxidation of VO_2(M). Finally, for the sample S-45, the Raman spectrum exhibits sharp peaks identical to those of the original V_2O_5 precursor, indicating complete oxidation. The zoomed region between 135–150 cm^{-1} (Fig. 3b) provides insights into peak shifts and the phase transition from VO_2(B) to VO_2(M). Thus, the development of the Raman bands corresponds well with the structural changes established using XRD and demonstrates the sensitivity of Raman spectroscopy for characterizing the long-range order and local structural changes.

A detailed analysis of the Raman spectra for samples S-35 and S-40, which consist of mixed phases of VO_2(M) and V_2O_5, indicates that these phases cannot be distinctly resolved *via* Raman spectroscopy due to the overlap in their characteristic vibrational modes. Thus, phase identification in this case needs to be done from X-ray diffraction (XRD) data. Additionally, the Raman spectrum of sample S-45 exhibits features consistent with V_2O_5, indicating a phase transformation from VO_2 to V_2O_5, and closely matches the spectral signature of the V_2O_5 precursor. Raman spectroscopy thus serves as a complementary technique to XRD, confirming that our simple synthesis method reliably produces VO_2 with MIT behavior.

Morphological studies

The morphology of VO_2 nanostructures was analyzed using SEM. Fig. 4 shows the SEM images of the as-grown and annealed vanadium oxide nanostructures. For the samples S-22, shown in Fig. 4a, multiple nanobelts are connected at the bottom and spread radially towards the top to form an urchin-like unit.

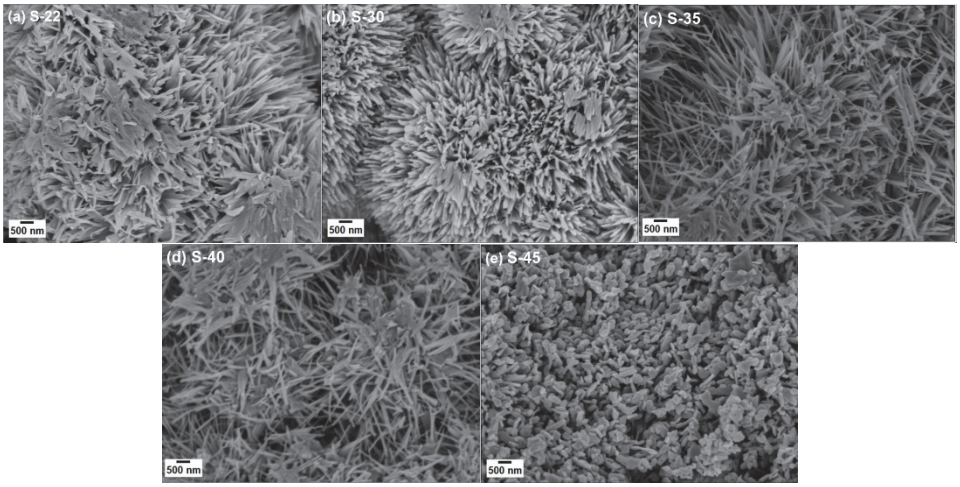

Fig. 4. SEM images illustrating the morphology of the nanostructure samples: a) S-22, b) S-30, c) S-35, d) S-40 and e) S-45.

The width of the nanobelts in the as-grown samples varies from ~50 to ~150 nm, and their length is in the sub-micrometer range. These urchin-like structures are symmetric with diameters ranging between 5–15 μm. This initial morphology is altered in the annealed samples. From the SEM image of S-30, we observe sharper needle-like structures compared to S-22, indicating denser, well-connected features with morphology that is consistent with the phase evolution observed from XRD data. The micrographs of samples S-35 and S-40 show a somewhat mixed microstructure. The micrograph of sample S-45 shows a significant change, where

needle-like features disappear, and the surface appears to develop granular features. Here, we did not detect the existence of the VO_2(M) phase and instead observe the formation of pure V_2O_5. In summary, SEM analysis demonstrates that annealing temperatures strongly influence the morphological evolution of the nanostructures, while the associated changes in crystallinity and phase composition are confirmed by XRD data.

Optical properties

We performed UV–Vis spectroscopy to study the transmittance characteristics of vanadium oxide nanostructures. We calculated the optical band gap of these nanostructures with the help of a Tauc plot, which follows the equation:

$$\alpha h\nu = A(h\nu - E_g)^n \quad (1)$$

Where E_g is the band gap, α is the absorption coefficient, $h\nu$ represents the energy of light, A is a constant and n denotes the nature of the transition.

Fig. 5 illustrates the effect of various annealing temperatures on the optical characteristics of the samples. The UV–Vis transmission spectra (Fig. 5a) indicate that the transmittance generally increases with annealing temperature, indicating improved crystallinity in the samples.

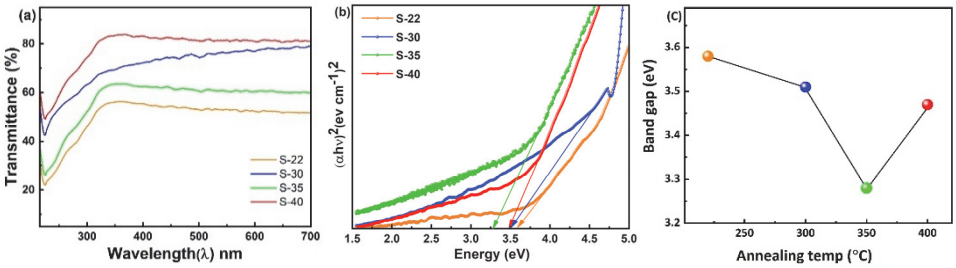

Fig. 5. a) Optical transmittance spectra of the samples annealed at various temperatures; b) corresponding Tauc plots representing the magnitude of the direct optical band gap; c) changes in optical band gap values with annealing temperature.

We calculated the direct band gap energies, from the Tauc plots in Fig. 5b, by extrapolating $(\alpha h\nu)^2$ *versus* energy ($h\nu$). The plots reveal a distinct trend of decreasing in optical band gap values with increasing annealing temperature up to 350 °C. Following this, there was a modest increase of the band gap at 400 °C. Corresponding band gap values were calculated from the Tauc plots. As shown in Fig. 5c, E_g decreases from 3.6 eV for sample S-22 to a minimum of 3.3 eV for sample S-35 and subsequently increases to 3.5 eV for sample S-40. Despite the minor morphological variations, the changes in E_g are primarily governed by phase transitions, as observed through XRD analysis. The increased band gap in hydro-

thermally synthesized urchin-like VO_2 samples with respect to bulk VO_2[28,29] (typically 0.6–0.7 eV for the monoclinic structure) can be explained by several factors. Nanoscale crystallite size leads to quantum confinement effects, producing a wider band gap. Since VO_2(B) was found to have a wider band gap than VO_2(M), the existence of both monoclinic (M) and metastable B phases together also contributes to the wider band gap.[30] The lattice distortion and structural distortions also change the electronic structure. Defects and oxygen vacancies create localized states that change the band gap.[32] All these factors together are the potential reasons behind the much broader band gap in the VO_2 nanostructures.

Thermochromic properties

Fig. 6 presents the differential scanning calorimetry (DSC) thermograms of VO_2(B) powders annealed at various temperatures (300–450 °C) for 30 min, with corresponding thermal parameters summarized in Table I. The transition temperature (T_C) was determined as the midpoint between the endothermic peak temperature during heating and the exothermic peak temperature during cooling. Samples S-22, S-30 and S-45 do not display any prominent endothermic or exothermic peaks in the DSC curves. The absence of a clear metal–insulator transition in S-22 and S-30 can be attributed to the dominance of the VO_2(B) phase, which does not exhibit a sharp transition like monoclinic VO_2(M). In addition, broader XRD peaks were observed for these samples, indicating reduced crystallinity. This leads to weaker cooperative lattice distortion, which is necessary for an abrupt structural transition. For sample S-45, the disappearance of the transition is due to the dominant V_2O_5 phase as identified by XRD, which does not exhibit a metal–insulator transition in this temperature range.[31,32]

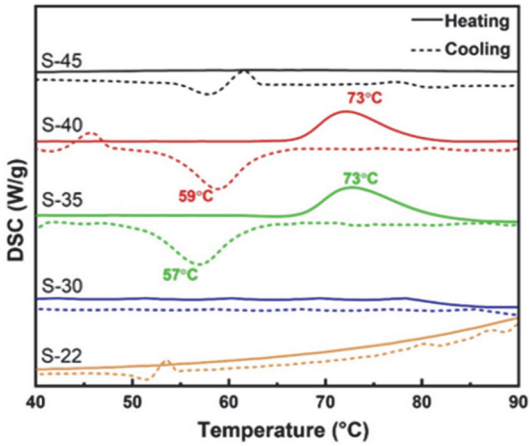

Fig. 6. DSC results illustrating a well-defined, reversible metal–insulator transition exclusively in the specimens annealed at 350 and 400 °C. In contrast, other samples exhibit a featureless thermal profile indicating the absence of a detectable phase transition.

For the samples S-35 and S-40, the endothermic peak maximum during the heating cycle remains nearly constant at ~73 °C. However, the exothermic peak

during the cooling cycle shifts slightly from 57 °C for S-35 to 59 °C for S-40. As a result, the calculated transition temperature (T_C, determined as the midpoint between heating and cooling peaks) increases only slightly from 65 °C (for S-35) to 66 °C (for S-40). Simultaneously, the thermal hysteresis width (ΔT), calculated as the difference between the heating and cooling transition temperatures, decreases from 16 to 14 °C. A reduction in the magnitude of ΔT suggests improved reversibility of the structural transformation. This behavior correlates with the enhanced crystallinity observed in the XRD patterns of S-40 relative to S-35, implying that improved structural ordering contributes to a more uniform and coherent phase transition. The observed T_C values are slightly lower than those of bulk VO_2(M), which is typically ~68 °C. This reduction to ~65 °C can be attributed to residual VO_2(B) and nanocrystalline interfaces. Overall, the appearance and sharpness of the metal–insulator transition are strongly governed by phase composition and crystallinity. Samples dominated by VO_2(B) or V_2O_5 do not exhibit a prominent transition, whereas samples containing predominantly the monoclinic VO_2(M) phase exhibit a distinct and reversible MIT. The improved crystallinity observed in XRD for S-35 and S-40 contributes to a narrower hysteresis width and more consistent structural transformation. Similar reductions in transition temperature and broadening of the MIT in nanocrystalline or mixed-phase VO_2 systems have been reported in previous studies, where strain effects and phase heterogeneity were found to influence MIT behavior.[33–35]

TABLE I. Comparison of phase transition temperatures obtained from DSC analysis during heating and cooling cycles

Sample	Annealing temp. °C	Dominant phase	Secondary phase	T_{heat} °C	T_{Cool} °C	T_C °C	ΔT °C
S-22	As-synthesized	VO_2(B)	–	–	–	–	–
S-30	300	VO_2(B)	VO_2(M)	–	–	–	–
S-35	350	VO_2(M)	V_2O_5, V_3O_7	73	57	65	16
S-40	400	V_2O_5	VO_2(M), V_3O_7	73	59	66	14
S-45	450	V_2O_5	–	–	–	–	–

The reduction in hysteresis width may be attributed to partial conversion of VO_2(B) to V_2O_5, as detected by X-ray diffraction (XRD). It may also be due to the presence of defects at the interface.[34] In contrast, samples S-35 and S-40 clearly exhibit a phase transition, consistent with the phase evolution confirmed by XRD.

In addition, sample S-35 exhibited an average transmittance of up to about 59 % obtained at room temperature (300 K), which is comparable to or slightly improved compared to published literature.[32,33] Phase transformation in VO_2 was clearly observed for samples annealed at 350 °C, demonstrating that this procedure is simple and energy efficient. For an observable phase transition in VO_2 prepared by reduction of V_2O_5, the required annealing temperature is often above 400 °C

and the annealing time is more than 1 h as reported in previous works.[36,37] Our method lowers the thermal budget by achieving VO_2 phase transformation faster (30 min) and at a lower annealing temperature than previously reported schemes. The resulting VO_2(M) nanostructures exhibit reversible thermochromic behavior.

Integrating XRD, Raman, optical and DSC analyses indicates a distinct phase––property correlation across the synthesized and annealed nanostructures. Specimens dominated by VO_2(B) (S-22, S-30) are characterized by broadened diffraction profiles and wider band gaps, while also lacking an observable MIT. In contrast, the formation of a predominantly VO_2(M) phase at 350 °C (S-35) is associated with significant band gap narrowing and the emergence of a well-defined, reversible MIT near 65 °C. Progressive oxidation from 400–450 °C results in the formation of V_2O5, which effectively suppresses this transition. These findings show that phase purity and crystallinity are major factors governing the thermochromic properties and MIT in these nanostructures.

CONCLUSION

VO_2 nanostructures were synthesized using a stabilizer-free hydrothermal process followed by controlled thermal annealing. The as-prepared sample (S-22) predominantly exhibited the metastable VO_2(B) phase with high crystallinity. Annealing at 350 °C resulted in the formation of a predominantly monoclinic VO_2(M) phase, accompanied by minor secondary phases of V2O5 and V_3O_7. With a further increase in annealing temperature to 400 °C, V_2O_5 became the predominant phase while the relative intensity of VO_2(M) decreased, indicating progressive oxidation of VO_2. Annealing at 450 °C resulted in the complete oxidation of VO_2 to V_2O_5. While the crystallite size increased with annealing temperature, the band gaps exhibited a non-monotonic variation with annealing temperature and phase composition. The sample annealed at 350 °C showed an average room-temperature transmittance of 59 % and a phase-transition temperature of ~65 °C. Samples S-35 and S-40 exhibit clear, reversible phase transitions between 65 and 66 °C. In summary, we demonstrate the tunability of phase composition and transition behavior in annealed VO_2 nanostructures and provide insight into the relationship between structural evolution and metal–insulator transition behavior. Our demonstration of a cost-effective and stabilizer-free hydrothermal synthesis route also offers a reduced thermal budget route for scalable vanadium dioxide production, enabling controlled phase evolution and metal–insulator transition behavior in VO_2 nanostructures.

Acknowledgements. The authors want to acknowledge the support and facilities provided by National Institute of Technology Raipur, India. The author also wants to acknowledge the Guru Ghasidas University Bilaspur, India for granting the study leave to do Ph.D.

ИЗВОД

ХИДРОТЕРМАЛНА СИНТЕЗА И ФАЗНА ТРАНСФОРМАЦИЈА VO_2(B) У VO_2(M): ИСТРАЖИВАЊЕ ПРЕЛАЗА МЕТАЛ–ИЗОЛАТОР

AISHWARYA RAJGONDA PATIL,[1] KRISHNA CHAITANYA SOLASA,[1] SOURAV KUMAR,[2] SHREEYA RANE[3] и PALASH ROY CHOUDHURY[4]

[1]École Centrale School of Engineering, Mahindra University, Hyderabad, India, [2]Department of Metallurgical Engineering and materials science, IIT Indore, India, [3]Department of Physics, University of Warwick, UK и [4]Mahindra University, Survey No: 62/1A, Bahadurpally, Jeedimetla, Hyderabad, Telangana 500043, India

У овом раду, VO_2(B) наноструктуре су синтетизоване хидротермалним путем без стабилизатора и успешно конвертоване у VO_2(M) на 350 °C за само 30 min. Овим поступком се постиже уштеда енергије у односу на уобичајене поступке, који генерално захтевају температуре више од 400 °C и трајање дуже од једног сата. Добијене VO_2 наноструктуре са игличастим честицама су окарактерисане коришћењем различитих техника као што су XRD, раманска спектроскопија, SEM и DSC како би се испитао фазни састав, морфологија и карактеристике прелаза метал-изолатор. Експериментални резултати показују да се VO_2(B) претежно трансформише у VO_2(M) након калцинације на 350 °C, са малим уделом секундарних оксидних фаза. Додатно, жарење на 450 °C довело је до потпуне фазне трансформације VO_2 у V_2O_5, што указује на осетљивост VO_2 на температуру калцинације. Температура прелаза изолатор-метал је ~65 °C, што је ниже него за VO_2 у комаду (~68 °C), што указује на модификовано понашање прелаза у наноструктурним узорцима. Ови резултати показују да се хидротермално синтетисани VO_2(B) може трансформисати претежно у VO_2(M) жарењем на 350 °C током 30 min, што омогућава реверзибилни прелаз метал–изолатор близу 65 °C.

(Примљено 1. новембра, ревидирано 16. децембра 2025, прихваћено 22. априла 2026)

REFERENCES

1. A. B. Georgescu, A. J. Millis, *Commun. Phys.* **5** (2022) 135 (https://doi.org/10.1038/s42005-022-00909-z)
2. A. Moatti, R. Sachan, J. Narayan, *J. Appl. Phys.* **128** (2020) 045302 (https://doi.org/10.1063/5.0006671)
3. G. Ekinci, B. Özkal, S. Kazan, *ACS Omega* **9** (2024) 26235 (https://doi.org/10.1021/acsomega.4c02001)
4. A. R. Galloni, Y. Yuan, M. Zhu, H. Yu, R. S. Bisht, C.-T. M. Wu, C. Grienberger, S. Ramanathan, A. D. Milstein, *Proc. Natl. Acad. Sci.* **121** (2024) e2318362121 (https://doi.org/10.1073/pnas.2318362121)
5. N. Shukla, A. V Thathachary, A. Agrawal, H. Paik, A. Aziz, D. G. Schlom, S. K. Gupta, R. Engel-Herbert, S. Datta, *Nat. Commun.* **6** (2015) 7812 (https://doi.org/10.1038/ncomms8812)
6. S. Jessadaluk, N. Khemasiri, P. Rattanawarinchai, S. Rahong, A. Rangkasikorn, N. Kayunkid, S. Wirunchit, A. Klamchuen, J. Nukeaw, *Jpn. J. Appl. Phys.* **58** (2019) SDDE12 (https://doi.org/10.7567/1347-4065/ab0aca)
7. A. Ainabayev, B. Walls, D. Casey, D. Caffrey, D. Mullarkey, A. McGlinchey, A. Khare, A. Tikhonov, C. Ilhan, D. Brennan, S. J. McCormack, I. Shvets, *J. Phys. Chem., C* **127** (2023) 24432 (https://doi.org/10.1021/acs.jpcc.3c06057)
8. R. Zhang, Q. S. Fu, C. Y. Yin, C. L. Li, X. H. Chen, G. Y. Qian, C. L. Lu, S. L. Yuan, X. J. Zhao, H. Z. Tao, *Sci. Rep.* **8** (2018) 17093 (https://doi.org/10.1038/s41598-018-35490-5)

9. Q. Song, J. Zhou, L. Meroueh, D. Broido, Z. Ren, G. Chen, *Appl. Phys. Lett.* **109** (2016) 263902 (https://doi.org/10.1063/1.4973292)
10. M. Li, S. Magdassi, Y. Gao, Y. Long, *Small* **13** (2017) 1701147 (https://doi.org/10.1002/smll.201701147)
11. M. M. Seyfouri, R. Binions, *Solar Energy Mater. Solar Cells* **159** (2017) 52 (https://doi.org/10.1016/j.solmat.2016.08.035)
12. F. Xu, X. Cao, Z. Shao, G. Sun, S. Long, T. Chang, H. Luo, P. Jin, *ACS Appl. Mater. Interfaces* **11** (2019) 4712 (https://doi.org/10.1021/acsami.8b20794)
13. D. Malarde, M. J. Powell, R. Quesada-Cabrera, R. L. Wilson, C. J. Carmalt, G. Sankar, I. P. Parkin, R. G. Palgrave, *ACS Omega* **2** (2017) 1040 (https://doi.org/10.1021/acsomega.7b00042)
14. C. Wang, H. Xu, C. Wang, T. Liu, S. Yang, Y. Nie, X. Guo, X. Ma, X. Jiang, *J. Alloys Compd.* **877** (2021) 159888 (https://doi.org/10.1016/j.jallcom.2021.159888)
15. J. Ni, W. Jiang, K. Yu, Y. Gao, Z. Zhu, *Electrochim. Acta* **56** (2011) 2122 (https://doi.org/10.1016/j.electacta.2010.11.093)
16. S. R. Popuri, M. Miclau, A. Artemenko, C. Labrugere, A. Villesuzanne, M. Pollet, *Inorg. Chem.* **52** (2013) 4780 (https://doi.org/10.1021/ic301201k)
17. S. Zhang, Y. Li, C. Wu, F. Zheng, Y. Xie, *J. Phys. Chem., C* **113** (2009) 15058 (https://doi.org/10.1021/jp903312h)
18. B.-R. Jia, M.-L. Qin, Z.-L. Zhang, S.-M. Li, X.-L. Wang, M. Huang, H.-Y. Wu, Z. Chen, X. Lu, L. Zhang, X-H. Qu, *J. Alloys Compd.* **704** (2017) 79 (https://doi.org/10.1016/j.jallcom.2017.02.046)
19. J. Liu, Q. Li, T. Wang, D. Yu, Y. Li, *Angew. Chem. Int. Ed.* **43** (2004) 5048 (https://doi.org/10.1002/anie.200460104)
20. K.-C. Zhou, D.-M. Cao, Z.-Y. Li, *Trans. Nonferrous Met. Soc. China* **16** (2006) 517 (https://doi.org/10.1016/S1003-6326(06)60090-3)
21. H. H. Afify, S. A. Hassan, M. Obaida, A. Abouelsayed, *Phys., E* **114** (2019) 113610 (https://doi.org/10.1016/j.physe.2019.113610)
22. D. Alie, L. Gedvilas, Z. Wang, R. Tenent, C. Engtrakul, Y. Yan, S. E. Shaheen, A. C. Dillon, C. Ban, *J. Solid State Chem.* **212** (2014) 237 (https://doi.org/10.1016/j.jssc.2013.10.023)
23. M. Dhananjaya, N. G. Prakash, A. L. Narayana, O. M. Hussain, *Appl. Phys., A* **124** (2018) 185 (https://doi.org/10.1007/s00339-017-1522-0)
24. D. Dreifus, M. P. F. Godoy, A. C. Rabelo, A. D. Rodrigues, Y. G. Gobato, P. C. Camargo, E. C. Pereira, A. J. A. De Oliveira, *J. Phys., D* **48** (2015) 445002 (https://doi.org/10.1088/0022-3727/48/44/445002)
25. D. Surya Bhaskaram, R. Cheruku, G. Govindaraj, *J. Mater. Sci. Mater. Electron.* **27** (2016) 10855 (https://doi.org/10.1007/s10854-016-5194-x)
26. B. Cheng, H. Zhang, Q. Li, J. Liu, B. Liu, *Inorganics* **10** (2022) 122 (https://doi.org/10.3390/inorganics10080122)
27. S. Zhang, Z. Zou, T. Lv, S. Li, Y. Zhang, *Int. J. Electrochem. Sci.* **15** (2020) 7203 (https://doi.org/10.20964/2020.08.05)
28. H. W. Verleur, A. S. Barker, C. N. Berglund, *Rev. Mod. Phys.* **40** (1968) 737 (https://doi.org/10.1103/RevModPhys.40.737)
29. K. Schneider, *J. Mater. Sci. Mater. Electron.* **31** (2020) 10478 (https://doi.org/10.1007/s10854-020-03596-0)

30. Meenu, P. Kumar, B. S. Dehiya, *J. Nanosci. Technol.* **5** (2019) 584 (https://doi.org/10.30799/jnst.195.19050102)
31. F. Mehmood, R. Pachter, N. R. Murphy, W. E. Johnson, C. V. Ramana, *J. Appl. Phys.* **120** (2016) 191 (https://doi.org/10.1063/1.4972038)
32. F. Arteaga-Cardona, A. P. Franco-Bacca, F. Cervantes-Alvarez, J. J. Alvarado-Gil, N. R. Silva-González, U. Salazar-Kuri, *Appl. Phys., A* **127** (2021) 159 (https://doi.org/10.1007/s00339-021-04309-y)
33. C. Xu, G. Liu, M. Li, K. Li, Y. Luo, Y. Long, G. Li, *Mater. Des.* **187** (2020) 108396 (https://doi.org/10.1016/j.matdes.2019.108396)
34. K. L. Gurunatha, S. Sathasivam, J. Li, M. Portnoi, I. P. Parkin, I. Papakonstantinou, *Adv. Funct. Mater.* **30** (2020) 27 (https://doi.org/10.1002/adfm.202005311)
35. L. Liu, F. Cao, T. Yao, Y. Xu, M. Zhou, B. Qu, B. Pan, C. Wu, S. Wei, Y. Xie, *New J. Chem.* **36** (2012) 619 (https://doi.org/10.1039/C1NJ20798A)
36. B. S. Beckerle, A. B. Cezar, I. T. Neckel, W. H. Schreiner, A. G. Bezerra Jr., I. L. Graff, J. Varalda, D. H. Mosca, *J. Appl. Phys.* **134** (2023) 123 (https://doi.org/10.1063/5.0169279)
37. S. A. Corr, M. Grossman, Y. Shi, K. R. Heier, G. D. Stucky, R. Seshadri, *J. Mater. Chem.* **19** (2009) 4362 (https://doi.org/10.1039/B900982E).

Journal of the Serbian Chemical Society
JSCS-info@shd.org.rs • www.shd.org.rs/JSCS
J. Serb. Chem. Soc. 91 (6) 631–647 (2026)
JSCS–5515
Original scientific paper
Published 6 July, 2026

Adsorption of copper ions onto acid-modified *Aframomum africanum* shell: Isotherm and kinetic studies

YANE CHIMBILIMA, MURALI DADI and TANWEER AHMAD*

Department of Chemistry, School of Mathematics and Natural Sciences, The Copperbelt University, P.O. Box 21692, Kitwe, Zambia

(Received 3 June, revised 29 July 2025, accepted 23 February 2026)

Abstract: In this work, copper ions were successfully removed from aqueous solution using the acid-modified *Aframomum africanum* shell (MAAS) as an adsorbent. The adsorbent was characterized using Fourier transform infrared (FTIR) spectroscopy and field emission scanning electron microscopy (FESEM). The *A. africanum* shells were also characterized before and after acid modification to determine their pH at the point of zero charge (pH_{PZC}). MAAS was found to have a pH_{PZC} value of 4.77. In batch experiments, the adsorption capacity of MAAS was investigated as a function of solution pH, adsorbent dosage, contact time, initial copper ion concentration and agitation speed. The results revealed that at a solution pH of 9, an adsorbent dosage of 5 g/L, a contact time of 30 min, an initial Cu(II) ion concentration of 50 mg/L and at an agitation speed of 250 rpm, the maximum Cu(II) ion adsorption capacity of MAAS was 31.25 mg/g. The adsorption kinetic data and isotherm data were also studied to find the suitable models of Cu(II) removal. The kinetic data and the isotherm data of Cu(II) removal by MAAS were found to follow the pseudo-second order kinetics model ($R^2 = 0.999$) and the Langmuir isotherm model ($R^2 = 0.990$), respectively. Therefore, the outcome suggested that *A. africanum* shells can be utilized as an economical and efficient adsorbent for the removal of Cu(II) from aqueous solution.

Keywords: adsorption; *Aframomum africanum*; copper ion; heavy metal; adsorption kinetics; adsorption isotherms.

INTRODUCTION

The existence of life on this planet depends on the availability of water. Water is increasingly being contaminated anthropogenically by activities such as industrial activities, agriculture, poor land usage, urbanization and non-sustainable growth. These factors have led to rapid degradation of surface and groundwater quality.[1] Among these activities, the release of effluents containing heavy metals remains a

* Corresponding author. E-mail: tanweerakhan@gmail.com
https://doi.org/10.2298/JSC250603010C

serious concern, especially for humans and aquatic life in mining areas of the world. According to the Environmental Protection Agency (EPA), a heavy metal is one that has a higher density and potential toxicity even at a lower concentration.[2] By specifying the lower limit value of heavy metals, defines heavy metals as metals having density greater than 5 g/cm^3.[3] A common heavy metal, copper is employed in innovative applications, including solar cells and phytotherapies, as well as in decorative work and electric cable manufacturing. The element is an essential micronutrient for various processes such as photosynthesis, metabolism and reproduction processes in living organisms.[4] However, high concentrations of non-biodegradable heavy metals, such as copper, in water bodies and in the soil have toxic effects on living organisms including humans.[5] If humans are exposed to large doses of copper, degeneration or possibly necrosis of the kidneys, liver and gastrointestinal tract would be the outcome. Copper has also been linked to changes in the nervous system or mental health issues, including anxiety and insomnia.[6]

The physicochemical techniques have mostly been employed in heavy metal eradication processes such as chemical precipitation, membrane-based techniques, ion exchange and electrochemical processes.[7] However, these remediation techniques have some drawbacks, such as high operational costs for metal complexes in trace concentrations, and high energy prerequisite.[8,9] Efforts have been made to resolve these drawbacks by adopting the adsorption technique. The process of adsorption involves the migration and accumulation of dissolved molecules onto the surface and porous structure of a biomaterial. As adsorbents, activated carbons have been widely employed to remove harmful metal ions from wastewater. But owing to their high cost of production and regeneration challenges, there is now more effort being made to find adsorbent materials of low energy requirements, simplicity in operation and, of course, which can be regenerated.[10] Examples of biomaterials that have been used before as adsorbents to eliminate heavy metals from wastewater include agricultural waste residues like groundnut shells, corn cob, rice husk and many more.[11] Adsorption has been found to exhibit the following advantages: cost-effectiveness, high efficiency, easy accessibility, minimal production of sludge, high adsorption capacity,[12] regeneration of adsorbents and possibility of metal recovery.[13] Furthermore, the use of unconventional materials is being widely encouraged now owing to the fact that they possess functional groups that may bind metals.[14–16]

The shell of the *Aframomum africanum* plant is another agricultural waste that may be a very good adsorbent for metal removal. Among a diverse range of affordable adsorbents, the *A. africanum* fruit shells (AAFS) were used as one of the promising, renewable, cost-effective biosorbents to eliminate Cu(II) ion from wastewater. *A. africanum* is a perennial, bushy and wild-growing plant with a leafy stem that may be up to 1.5 m high. The leaves are simple, alternate and lanceolate with matured ones measuring as long as 40 cm in length and 12–15 cm wide. The

plant is native to tropical African countries such as Ghana, Nigeria, Liberia and Cameroon and is an important commercial crop in east African countries such as Ethiopia. *A. africanum* fruit belongs to the family of *Zingiberaceae*.[17] It is one of the highly consumed fruits in Zambia, which creates a notable environmental problem because the shells are usually thrown anyhow after the inner contents of the fruit have been eaten.[18]

To the best of the authors' knowledge, no studies have been done regarding the application of acid-modified *A. africanum* shell (MAAS) as an adsorbent for Cu(II) ion removal from aqueous solution. Therefore, this study was planned to assess the adsorption properties of the acid-modified *A. africanum* shell towards the removal of Cu(II) ions from aqueous solution. The surface functional groups and the morphology of the acid-modified *A. africanum* shells were evaluated before and after adsorption procedures. The experimental variables have been examined in relation to the removal of Cu (II), including the solution pH, initial metal concentration, particle size and contact time. Analysis of the experimental data has been done using kinetic and equilibrium isotherm models.

EXPERIMENTAL

Materials

Analytical grade chemicals were used. Copper (II) sulfate pentahydrate ($CuSO_4.5H_2O$) was prepared by dissolving in distilled water for the experiment. The solution pH was adjusted from 2 to 12 using 0.1 M sodium hydroxide (NaOH) and 0.1 M hydrochloric acid (HCl). 0.5 M nitric acid (70 %, HNO_3) was utilized for the chemical treatment of the adsorbent.

Preparation of the adsorbent

The adsorbent *Aframomum africanum* fruit shell (AAFS) was procured from Chisokone market in Kitwe town of Zambia. The authenticity of the fruit was confirmed by the Department of Forest Herbarium Section under the Ministry of Green Economy in Kitwe Town. The fruit shell was washed thoroughly to remove dust and impurities using tap water. Later, the shells were sun-dried for 10 days and then oven-dried for 24 h at 80 °C to remove moisture from the shells properly. Dried shells were crushed in a blender and sieved by allowing the particles to pass through the 212-μm sieve. The powder obtained was again boiled in distilled water for 24 h to completely eliminate any coloration from the sample. Finally, the sample was dried in the oven for 24 h at 80 °C to remove moisture and stored in an air-tight bottle.

Chemical modification of the AAFS dried powder

The AAFS dried powder (82.58 g) was added to a 2 L conical flask that contained 0.5 M dilute nitric acid. The mixture was shaken for 2 h on an orbital shaker at 140 rpm and was left to stand for 24 h. After repeatedly washing the modified sample in distilled water to get rid of any remaining nitric acid, it was dried in an oven set at 60 °C for 48 h. The modified AAFS powder (now called MAAS) was stored in an air-tight bottle for later use. The flow diagram of *A. africanum* fruit shell drying and its conversion into acid-modified adsorbent is shown in Fig. 1.

Preparation of copper sulphate solution

To prepare a 1000 ppm Cu (II) sulphate stock solution, 3.93 g of copper (II) sulphate pentahydrate was dissolved in 1 L of distilled water. All subsequent Cu(II) ion concentration

solutions in this experiment were prepared by withdrawing the calculated volume of stock solution and diluting it in a volumetric flask of the required volume using distilled water only. To prepare a solution of a specific concentration, the dilution formula was used.

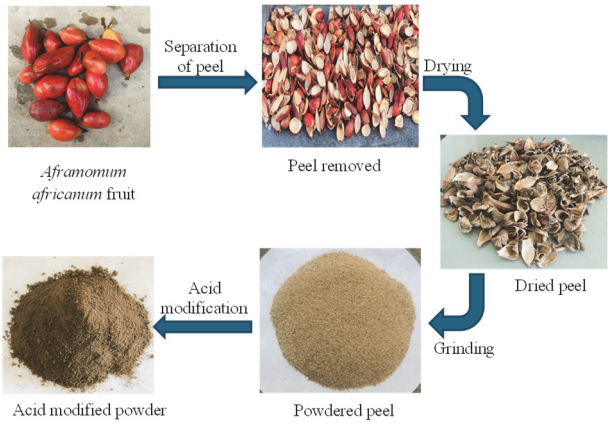

Fig. 1. Schematic representation of *Aframomum africanum* fruit shell drying and its conversion into acid-modified adsorbent.

Characterization of the adsorbent

The different functional groups on the adsorbent's surface were identified using Fourier transform infrared spectroscopy (FTIR, Alpha-II, Bruker, Germany). With a resolution range of 2–4 cm^{-1}, the FTIR spectra were captured before and after the Cu(II) adsorption within the wavenumber 400–4000 cm^{-1} region. The FESEM (JEOL-JST-IT80, Japan) was used to investigate the surface morphology of the adsorbent before and after the adsorption process.

The pH_{PZC} parameter was determined by placing 40 ml of an aliquot of sodium nitrate into 10 different Erlenmeyer flasks. The pH of the sodium nitrate solutions in the Erlenmeyer flasks was changed from 3 to 12 by reading values on the pH meter using 0.1 M HCl and 0.1 M NaOH solutions. To each flask, 5 g of the adsorbent was added and the flasks were shaken for 24 h. After equilibrium, the content was filtered, the final pH of the filtrate of each flask was measured and recorded. Finally, plots of change in pH (ΔpH, *i.e.*, initial pH – final pH) against initial pH (pHi) were constructed.

Batch adsorption studies

In the batch experiment, 250 mL conical flasks were used to pour 100 mL of Cu(II) solution with the calculated amount of MAAS adsorbent. To get the concentration needed for each experiment, the Cu(II) solution was diluted with distilled water in a standard flask. The content of the conical flask was then agitated at a fixed number of revolutions per minute on a shaker, for a fixed contact time and at room temperature. After that, filter paper was used to separate the adsorbent from the mixture. The residual concentrations of Cu ions were measured using an atomic absorption spectrophotometer (contrAA 300, Analytik Jena, Germany.)

The adsorption capacity (amount of adsorption) of the adsorbent at equilibrium, q_e (mg/g), and the percentage of heavy metal removal R (%) were determined as:

$$q_e = \frac{c_i - c_e}{m} V \tag{1}$$

$$R = 100\frac{c_i - c_e}{c_i} \quad (2)$$

where m is the dry weight of the adsorbent (g), V is the volume of the Cu(II) ions in solution (L), c_i is the initial Cu(II) ion concentration (mg/L) and c_e is the Cu(II) ion concentration (mg/L) at equilibrium.

The effect of independent variables, such as contact time (5–120 min), and initial Cu(II) concentration (10–150 mg/L) on the adsorption capacity of MAAS adsorbent against Cu(II) was observed at a fixed temperature (25 °C), fixed volume of Cu(II) solution (100 mL) and adsorbent dosage (5.0 g/L). The effect of varying each individual parameter was investigated while holding the other parameters constant. To calculate the kinetic parameters, the adsorption data of Cu(II) against time were used and to calculate the isotherm parameters, the adsorption data of Cu(II) against its equilibrium concentration was equally exploited. Additionally, regression coefficients (R^2) were calculated for the adsorption kinetics and the isotherms.

RESULTS AND DISCUSSION

FTIR analysis of the MAAS

It is crucial to identify the chemical functional groups on the adsorbent's surface in order to understand the adsorption mechanism of Cu(II) by the adsorbent. The chemical functional groups present could be responsible for the metal ion binding onto the surface of the adsorbent.[19] As seen in Fig. 2, the FTIR spectrum of MAAS before adsorption contains hydroxyl groups (–O–H) and phenols as well as the –N–H group indicated by the broad transmission peak at 3365.[20] The asymmetric C–H stretching of surface methyl groups, which are often found in the lignin structure, is indicated by the peak at 2917 cm^{-1}.[21,22] The band observed around 1637 cm^{-1} is due to the C=O stretching of the carbonyl group. The C–O stretching of alcohol and carboxylic acid groups in cellulose, hemicelluloses and lignin or C–O–C stretching in cellulose and hemicellulose, was identified by the strong band at 1043 cm^{-1}.[20] The role played by these functional groups is quite important in heavy metal adsorption because of the functional groups' affinity for metal ions.

The FTIR spectrum of post adsorption MAAS (MAAS–Cu) is shown in Fig. 2 as well. It was observed that the post adsorption spectra had peaks at exactly the same wavenumber as the pre-adsorption spectra. However, a reduction in peak intensities was observed. The reduction in peak intensities suggests the involvement of various functional groups in complexation with Cu(II) without undergoing major chemical transformation. Additionally, this showed that the copper adsorption mechanism involved a large number of functional groups found in the spectra.[9]

FESEM analysis of MAAS

Using FESEM, the surface morphology of MAAS was analyzed before and after the adsorption of Cu(II) ions. Fig. 3a shows the surface morphology of the

adsorbent before Cu(II) adsorption, while Fig. 3b represents Cu(II) adsorbed onto the surface of MAAS.

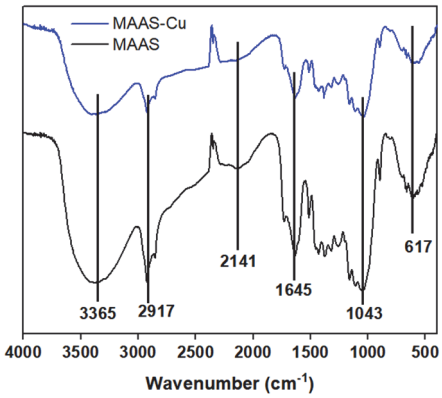

Fig. 2. FTIR spectra for the acid-treated adsorbent.

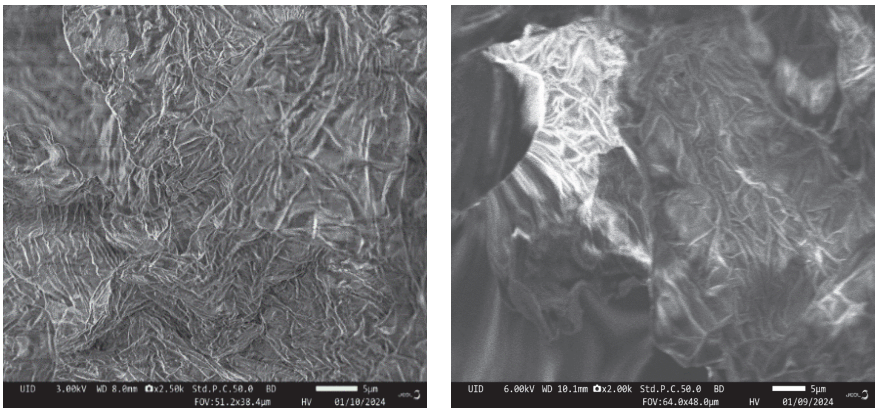

(a) (b)

Fig. 3. FESEM images of MAAS before (a) and after (b) adsorption of Cu(II).

Pre-adsorption surface of MAAS (Fig. 3a) contains pores and cavities on a rough and uneven surface of the acid-modified adsorbent. The post-adsorption MAAS surface pores were covered with Cu(II) ions, as seen in Fig. 3b, and the majority of the pores became invisible. Furthermore, the post-adsorption MAAS surface became somewhat smoother. This indicated that the surface pores were covered with Cu(II)ions.

Point of zero charge

It is the pH at which the adsorbent surface has no net charge. The pH_{PZC} of MAAS was determined for both the untreated adsorbent and the nitric acid-treated adsorbent. The results are shown in Fig. 4. The acid-modified adsorbent had a

pH_{PZC} of 4.77, which means that at pH values lower than this its surface is positively charged and at pH higher than 4.77 the adsorbent's surface is negatively charged. The pH_{PZC} of the untreated adsorbent was 7.62.

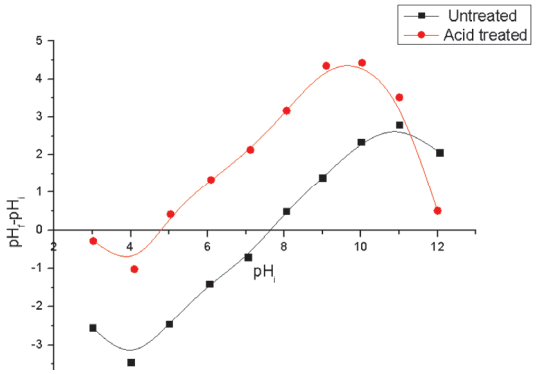

Fig. 4. pH_{PZC} of the untreated and treated adsorbent.

Effect of solution pH

The most significant parameter affecting the adsorption of Cu(II) ions onto MAAS is the solution pH. It establishes the adsorbent's surface charge as well as the adsorbate's degree of ionization and speciation.[23] The pH of the Cu(II) solutions was changed from 2 to 12 while maintaining the same initial concentration of 50 mg/L, contact time of 60 min, agitation speed of 150 rpm, and dosage of 5 g/L. From the experiment, maximum adsorption was 99.73 % at pH 9. The percentage of copper removed was low at low pH. The adsorbent surface is positively charged if the pH of the solution is lower than the pH_{PZC}. Conversely, for a solution pH greater than pH_{PZC}, deprotonation causes the adsorbent surface to become negatively charged, which promotes Cu(II) and the adsorbent surface's electrostatic attraction and raises the adsorption percentage.[9] This is explained by the extra H^+ that surrounds the binding sites and causes a protonation process that makes them positively charged. This results in the repulsion of metal cations away from the adsorption sites, making the adsorption process unfavorable. Additionally, the presence of H^+ in solution results in competitive adsorption between the H^+ and metal cations. This leads to competition between H^+ and Cu(II) for the adsorbent's adsorption sites, which results in repulsion.[24, 25] Thus, pH 9 was chosen for the subsequent adsorption studies because it is above the pH_{PZC}. Above pH 9 the percentage removal of Cu(II) decreased. This may be due to the hindrance effect caused by the abundant OH^- (hydroxide precipitation) preventing the diffusion of Cu(II) onto the adsorbent. The results are shown in Fig. 5a.

Effect of adsorbent dose

To explore the influence of adsorbent dosage on the elimination of copper from wastewater, the dosage was varied from 0.5, 1.0, 2.0, 3.0, 4.0 and 5.0 g/L

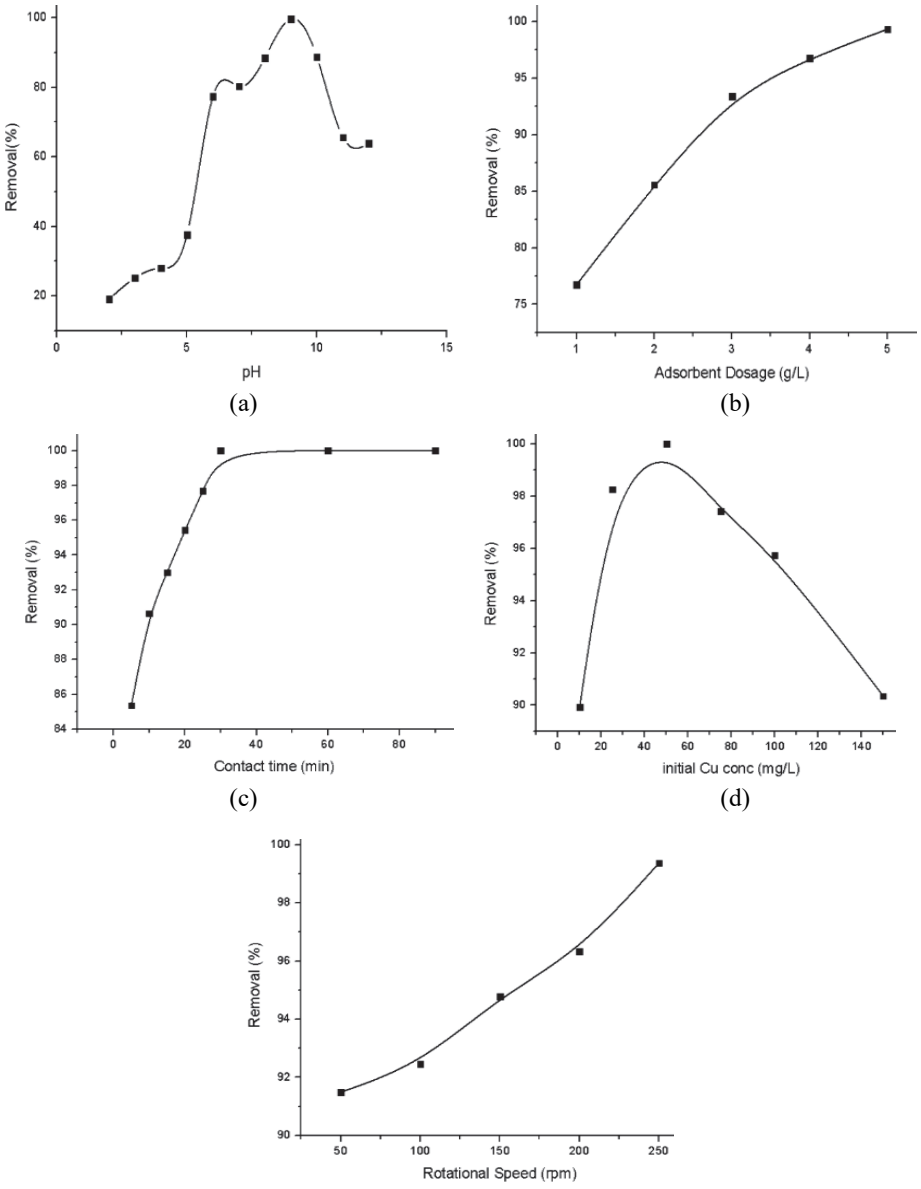

Fig. 5. Effect of: a) solution pH, b) adsorbent dosage, c) contact time, d) initial Cu(II) concentration and e) rotational speed on Cu ion removal efficiency.

while keeping other parameters unchanged (pH 9, contact time 60 min, initial concentration 50 mg/L and agitation speed 150 rpm). The results in Fig. 5b show that the removal efficiency increased with increasing adsorbent dosage, producing

the highest efficiency removal of 99.33 % at a dosage of 5 g/L. The increased percentage removal can be attributed to the number of available adsorption sites, which increased with the mass of the adsorbent.[26] Therefore, an optimal adsorbent dosage of 5 g/L was used in the follow-up adsorption experiments.

Effect of contact time

The time of contact between the adsorbent and the aqueous metal solution is another parameter which influences the uptake of metal ions. At constant parameters (pH 9, adsorbent dose 5 g/L, initial concentration 50 mg/L and agitation speed 150 rpm), studying the effect of contact time (5, 10, 20, 30, 60, 90 and 120 min) on the removal percentage of Cu(II), the results are revealed in Fig. 5c. From the graph, the greatest removal efficiency of Cu(II) was more pronounced during the first 30 min. This is attributed to the availability of vacant sorption sites of the adsorbent during the initial stage of the adsorption process.[27] After 30 min, the amount of Cu(II) adsorbed remained unchanged. This could be due to the active sites present on the adsorbent's surface being saturated by the Cu (II) molecules.

Effect of initial Cu(II) concentration

The effect of initial Cu(II) concentration on the removal efficiency was investigated for different solution concentrations of 10, 25, 50, 75, 100 and 150 mg/L while ensuring that the other parameters were kept constant. From the experimental results, the percentage removal of Cu(II) increased with the increase of Cu(II) concentration from 10 to 50 mg/L. As can be seen from Fig. 5d, the removal efficiency increased from 89.93 % for the initial Cu(II) concentration of 10 mg/L to 100 % for the initial Cu(II) concentration of 50 mg/L after the adsorption process. However, from 50 mg/L, further increase in the initial Cu(II) concentration resulted in a decreased removal efficiency. This reduced removal at higher initial concentrations is attributed to the adsorbent's surface being saturated at the relatively high metal concentration[13] and also desorption may have occurred.[28]

Effect of agitation speed

The influence of varying the speed of agitation at 50, 100, 150, 200 and 250 rpm was also investigated while maintaining other parameters constant (pH 9, adsorbent dose 5g/L, 30 min of contact time and initial metal concentration 50 mg/L). From the experimental results obtained in Fig. 5e, the removal efficiency increased with an increase in the speed of agitation. The results show a maximum removal percentage of almost 100 % at an agitation speed of 250 rpm. At low speeds, the adsorbent accumulates at the bottom instead of spreading throughout the solution. The result is that the sorption sites below the above layers of the adsorbent get buried leading to the low removal percentage of the metal ions.

Therefore, the speed of agitation of the adsorbate-adsorbent mixture should be sufficient enough to ensure the adsorbent spreads throughout the solution so that the unoccupied binding sites are exposed for the metal uptake.[29]

Adsorption isotherm studies

In order to investigate the distribution of Cu(II) ions between the adsorbent and the bulk solution, the most common adsorption isotherm models were used by fitting the equilibrium adsorption data into their respective isotherm equations.[30] The adsorption isotherm models used were the Langmuir, Freundlich, Temkin and Dubinin–Radushkevich (D–R) isotherm models.

Langmuir adsorption isotherm. The Langmuir adsorption isotherm model suggests that the adsorption of adsorbate molecules onto the adsorbent surface is a monolayer[31] and that the adsorbent has a finite number of homogeneously distributed and energetically uniform sorption sites. Therefore, this model applies to adsorption on adsorbent surfaces which are entirely homogeneous. A plot of c_e/q_e *vs*. c_e should yield a straight line if the Langmuir isotherm model is obeyed by the adsorption equilibrium as shown in Fig. 6a. From the plot, q_m and K_L values can be evaluated, which are obtained from the slope ($1/q_m$) and the intercept ($1/q_mK_L$), respectively.

An important aspect of the Langmuir isotherm called the separation factor, R_L (a dimensionless constant), is very useful in predicting the affinity between the adsorbate and the adsorbent.[32] The separation factor, which is also called the equilibrium parameter, is defined as:

$$R_L = \frac{1}{1 + K_L c_i} \tag{3}$$

By determining the magnitude of the separation factor, the adsorption process is favorable within the range $0 < R_L < 1$, unfavorable when $R_L > 1$, linear when $R_L = 1$, and the process is irreversible when $R_L = 0$. The Langmuir constant (K_L = = 0.508 L/mg) indicates a strong affinity between the adsorbent and the adsorbate. Furthermore, the separation factor (R_L = 0.04), being closer to zero, confirms highly favorable adsorption. Table I shows that adsorption follows the Langmuir isotherm model (R^2 = 0.99) with a q_{max} value of 31.25 mg/g. Modified *A. africanum* shell has a higher biosorption capacity for Cu(II) ion removal than most of the biosorbents previously described in the literature.[33–36]

Freundlich adsorption isotherm. The Freundlich adsorption isotherm suggests that the uptake of adsorbate solutes occurs on the heterogeneous surface of an adsorbent by multilayer adsorption. The model's assumption is that the uptake of sorbate molecules occurs on the heterogeneous surface of an adsorbent by multilayer adsorption.[37] This isotherm model describes adsorbents whose active sites have different affinities or adsorption energies for adsorbate solutes. The values of the

Freundlich constants can be obtained by plotting ln q_e *vs.* ln c_e with log k_F as the intercept and the slope equal to $1/n$ shown in Fig. 6b. The magnitude of n indicates the favorability of biosorption. If the value of $n < 1$ then the biosorption is unfavorable, when $n = 1$ then the separation within the two phases is not dependent on the concentration and when $n > 1$, it implies the adsorption of the adsorbate molecules onto the adsorbent surface is favorable. The Freundlich constant (k_F = 9.92 $mg^{1-1/n}$ $L^{1/n}$ g^{-1}) indicates a high adsorption capacity of the adsorbent. The value of $1/n = 0.412$ ($n = 2.43$) suggests favorable adsorption on a heterogeneous surface. However, the comparatively lower R^2 value indicates that the Freundlich isotherm provides a weaker fit than the Langmuir isotherm. The values of n and k_F calculated using slope and intercept were 2.42 and 9.92 with $R^2 = 0.862$ as shown in Table I. Consequently, adsorption has been conducted as a chemical process since the value of $n > 1$.

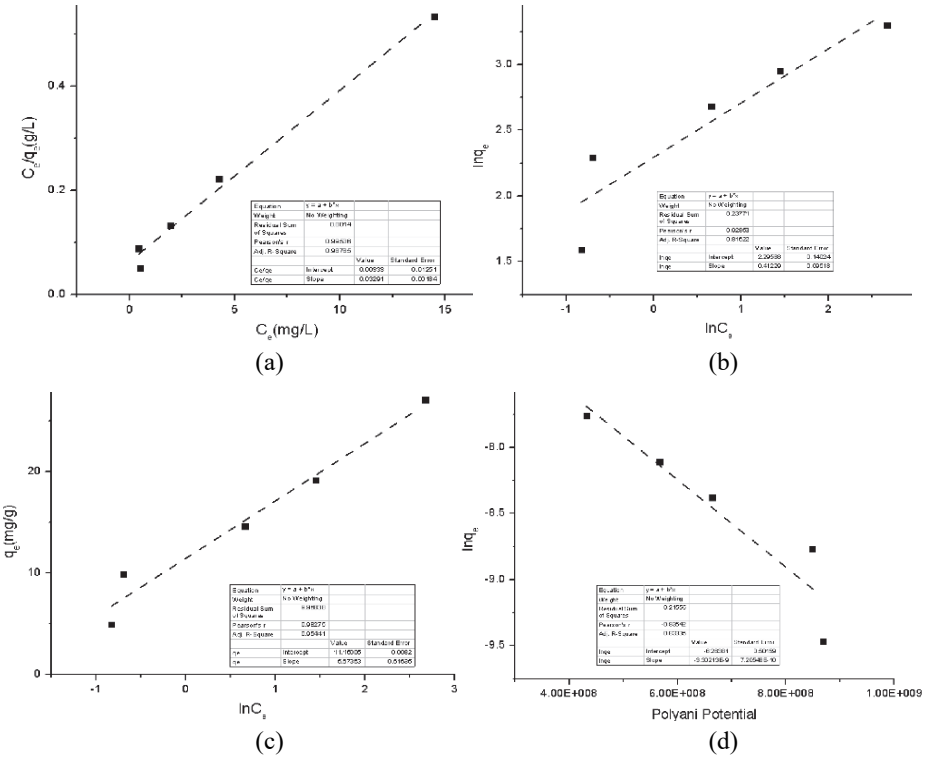

Fig. 6. Adsorption isotherm plots of Cu(II) removal through MAAS; a) Langmuir linear model, b) Freundlich linear model plot, c)Temkin isotherm linear model plot and d) D–R isotherm linear model.

Temkin adsorption isotherm. The heat involved in the adsorption of Cu(II) on MAAS was evaluated through the Temkin isotherm. It is assumed that the decline

in the heat of adsorption followed a linear trend as opposed to a logarithmic curve.[38] As illustrated in Fig. 6c, the slope of the q_e *vs.* ln c_e plot can be used to compute the heat of adsorption constant (B). The Temkin constant B (436.73 J/mol) indicates a moderate heat of adsorption, suggesting that the process is predominantly physical in nature. The equilibrium binding constant (K_T = 7.52 L/mg) reflects a good affinity between the adsorbent and the adsorbate. Table I provides a summary of the computed values for the Temkin isotherm constants and associated parameters. The computed values are close to the actual heat involved in the adsorption, as indicated by the model's correlation coefficient for Cu(II) adsorption data, which was determined to be 0.985.

Dubinin–Radushkevich (D–R) adsorption isotherm. The D–R isotherm assumes that the sorption sites are not identical and takes into account the idea of adsorbent surface heterogeneity, just like the Freundlich isotherm does.[39] The D–R model's linearized form is provided as:

$$\ln q_e = \ln q_{2,\max} - \beta\varepsilon^2 \tag{4}$$

where ε (kJ^2 mol^2) is the Polanyi potential and β (mol^2/J^2) is the activity coefficient associated with the mean adsorption energy.

The following relation was used to derive the Polanyi potential:[40]

$$\varepsilon = RT \ln(1 + 1/c_e) \tag{5}$$

The mean free energy of adsorption (E_A) per molecule of adsorbate can be calculated using the D–R isotherm constant ($K_{D–R}$) when the adsorbate molecules migrate from infinity to the adsorbent surface. It can be computed as:

$$E_A = \frac{1}{\sqrt{2K_{D–R}}} \tag{6}$$

Table I lists the D–R isotherm constants for Cu(II) adsorption onto MAAS along with the associated mean free energy of adsorption. The type of the adsorbent and the adsorbate determine the adsorption potential, which is unaffected by temperature. It is possible to determine whether adsorption is physical or due to chemical ion exchange by examining the E_A. The adsorption phase that comes after the chemical ion exchange is shown by the values of E_A that fall between 8 and 16 kJ/mol. The average free energy for this adsorption (E_A = 12.90 kJ/mol) falls within the range, indicating that ion-exchange followed the adsorption mechanism. The D–R constant β (3.00×10^{-9} mol^2/J^2) suggests a narrow energy distribution and supports adsorption occurring predominantly in microporous region of the adsorbent. Fig. 5d displays the linearized D–R plot, and the linear plot's correlation coefficient (R^2) was determined to be 0.875. As a result, the Langmuir isotherm was better suited by the adsorption data than the Freundlich, Temkin and D–R isotherm models.

TABLE I. The parameter values of adsorption isotherm models of Cu(II) adsorption onto modified *Aframomum africanum* shells at 25 °C

Model	Model parameter	Value
Langmuir	q_{max} / mg g^{-1}	31.25
	K_L / L mg^{-1}	0.508
	R_L	0.04
	R^2	0.99
Freundlich	K_F / mg$^{1-1/n}$ L$^{1/n}$ g^{-1}	9.92
	$1/n$	0.412
	R^2	0.862
Temkin	B / J mol^{-1}	436.73
	K_T / L mg^{-1}	7.52
	R^2	0.985
D–R	q_{max} / mg g^{-1}	121.1
	$q_{2,max}$ / mmol g^{-1}	1.91
	E_A / kJ mol^{-1}	12.9
	β	3.00×10^{-9}
	R^2	0.875

Adsorption kinetic study

During adsorption studies, determining the rate and comprehending the mechanism of heavy metal adsorption are crucial. In order to fit the experimental results, various kinetic models have been presented.[41] The pseudo-first-order kinetic model and the pseudo-second-order kinetic models are the only two kinetic models covered in this study.

Pseudo-first-order kinetics model (PFO). As illustrated in Fig. 7a, linear plots of log ($q_e - q_t$) *versus* t suggest the applicability of this kinetic model. From the graph, k_1 can be computed.

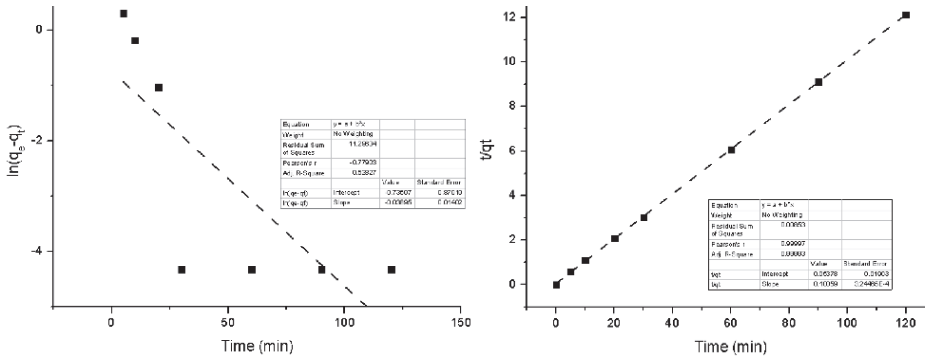

(a) (b)

Fig. 7. Adsorption kinetics of Cu(II) removal: a) pseudo-first and b) pseudo-second order kinetic model plot.

Pseudo-second-order kinetics model (PSO). The mechanism of adsorption is assumed to follow a second-order kinetics model if a plot of t/q_t against t produces a straight-line graph. The plot's slope ($1/q_e$) and intercept ($1/k_2q_e^2$) yield the values of q_e and k_2, respectively.

A well-established kinetic models, PFO and PSO were used to study the adsorption kinetics of Cu(II) adsorption onto MAAS. The Cu(II) adsorption data were collected at 50 mg/L an initial concentration at different time intervals (from 5 min to 120 min) and applied to linearized PSO shown in Fig. 7a and b. Within 30 min of contact time, 99 % of adsorption was found to occur. PFO and PSO were used to visualize the collected kinetic data. From the plotted data, it was observed that Cu(II) adsorption onto MAAS poorly followed the PSO ($R^2 = 0.606$) shown in Fig. 7a but perfectly followed the PSO kinetic model. The linear curve fitting of the PFO and PSO gave the correlation coefficient (R^2) value of 0.999 shown in Fig. 7b. It was also observed that for PSO kinetics, the theoretical adsorption capacity $q_{e,cal}$ (10.00 mg/g) and experimental values $q_{e,exp}$ (9.901 mg/g) were extremely close, however for PFO kinetics, these values were different, Table II. The PSO kinetics model was therefore more applicable, as evidenced by the same values for $q_{e,cal}$ and $q_{e,exp}$ and a higher regression coefficient value ($R^2 = 0.99$) compared to the PFO ($R^2 = 0.606$).

TABLE II. The parameter values of adsorption kinetic models of Cu(II) ion adsorption by modified *Aframomum africanum* shells

Model	Model parameter	Value
Pseudo-first-order	q_e / mg g^{-1}	0.478
	k_1 / min^{-1}	0.038
	R^2	0.606
Pseudo-second-order	q_e / mg g^{-1}	10
	k_2 / g mg^{-1} min^{-1}	0.189
	R^2	0.999

CONCLUSION

In the present study, low-cost adsorbents were successfully prepared from *Aframomum africanum* fruit through chemical surface modification. Nitric acid was used to modify the fruit shell powder, FESEM and FTIR were used to observe the changes in the adsorbent surface. The adsorption of Cu(II) from aqueous solution by the acid-modified adsorbent was investigated under various conditions of pH, adsorbent dosage, contact time, initial Cu(II) concentration and agitation speed. Among these conditions, pH was found to be the most significant factor affecting the adsorption of Cu(II). For a dosage of 5 g/L, a contact time of 30 min and an initial Cu(II) concentration of 50 mg/L, the maximum removal of Cu(II) was 100 % at pH 9. The Langmuir isotherm model and the pseudo-second-order kinetic model were able to adequately fit the experimental results. The Langmuir isotherm predicted monolayer

adsorption of Cu(II) ions with a maximum adsorption capacity of 31.25 mg/g. *A. africanum* is an effective adsorbent for the sequestration of Cu (II) from aqueous solution, according to the experimental data.

Acknowledgement. Thanks to Department of Chemistry, School of Mathematics and Natural Sciences, The Copperbelt University for laboratory facilities.

ИЗВОД

АДСОРПЦИЈА ЈОНА БАКРА НА КИСЕЛИНОМ МОДИФИКОВАНУ ЉУСКУ *Aframomum africanum*: ИЗОТЕРМСКА И КИНЕТИЧКА ИСПИТИВАЊА

YANE CHIMBILIMA, MURALI DADI и TANWEER AHMAD

Department of Chemistry, School of Mathematics and Natural Sciences, The Copperbelt University, P.O. Box 21692, Kitwe, Zambia

У овом раду јони бакра су успешно уклоњени из воденог раствора применом киселином модификоване љуске *Aframomum africanum* (MAAS) као адсорбента. Адсорбент је окарактерисан применом инфрацрвене спектроскопије са Фуријеовом трансформацијом (FTIR) и скенирајуће електронске микроскопије са емисијом поља (FESEM). Љуске *A. africanum* су такође окарактерисане пре и после киселинске модификације ради одређивања pH вредности на тачки нултог наелектрисања (pH_{PZC}). Утврђено је да MAAS има pH_{PZC} вредност од 4,77. У серији експеримената испитиван је адсорпциони капацитет MAAS у зависности од pH вредности раствора, дозе адсорбента, времена контакта, почетне концентрације јона бакра и брзине мешања. Резултати су показали да је при pH вредности раствора од 9, дози адсорбента од 5 g/L, времену контакта од 30 min, почетној концентрацији Cu(II) јона од 50 mg/L и брзини мешања од 250 rpm постигнут максимални адсорпциони капацитет MAAS за Cu(II) јоне од 31,25 mg/g. Кинетички подаци и подаци изотерме адсорпције анализирани су ради одређивања одговарајућих модела уклањања Cu(II). Утврђено је да кинетички подаци прате модел псеудо-другог реда ($R^2 = 0{,}999$), док изотермски подаци прате Ленгмиров модел изотерме ($R^2 = 0{,}990$). Резултати указују да се љуске *A. africanum* могу користити као економичан и ефикасан адсорбент за уклањање Cu(II) јона из водених раствора.

(Примљено 13. јуна, ревидирано 30. јуна, прихваћено 2. децембра 2026)

REFERENCES

1. V. Homem, L. Santos, *J. Environ. Manage.* **92** (2011) 2304 (https://doi.org/10.1016/j.jenvman.2011.05.023)
2. C. Yan, Y. Yang, J. Zhou, M. Liu, M. Nie, H. Shi, L. Gu, *Environ. Pollut.* **175** (2013) 22 (https://doi.org/10.1016/j.envpol.2012.12.008)
3. C. S. Lundborg, A. Tamhankar, *BMJ.* **358** (2017) j2440 (https://doi.org/10.1136/bmj.j2440)
4. *Pharmaceuticals in drinking-water,* World Health Organization, Geneva, 2012, p. 35 (https://apps.who.int/iris/handle/10665/44630)
5. S. Babić, M. Periša, I. Škorić, *Chemosphere* **91** (2013) 1635 (https://doi.org/10.1016/j.chemosphere.2012.12.072)
6. J. Porras, C. Badoya, J. Silva-Agredo, A. Santamaría, J. J. Fernández, R. A. Torres-Palma, *Water Res.* **94** (2016) 1 (https://doi.org/10.1016/j.watres.2016.02.024)

7. Z. Wei, J. Liu, W. Shangguan, *Chinese J. Catal.* **41** (2020) 1440 (https://doi.org/10.1016/S1872-2067(19)63448-0)
8. K. Košutić, D. Dolar, D. Ašperger, B. Kunst, *Sep. Purif. Technol.* **53** (2007) 244 (https://doi.org/10.1016/j.seppur.2006.07.015)
9. C. A. Igwegbe, S. N. Oba, C. O. Aniagor, A. G. Adeniyi, *Ind. Eng. Chem. Res.* **93** (2021) 57 (https://doi.org/10.1016/j.jiec.2020.09.023)
10. M. N. Chong, B. Jin, C. W. K. Chow, C. Saint, *Water Res.* **44** (2010) 2997 (https://doi.org/10.1016/j.watres.2010.02.039)
11. S. Dong, J. Feng, M. Fan, Y. Pi, L. Hu, X. Han, M. Liu, J. Sun, J. Sun, *RSC Adv.* **5** (2015) 14610 (https://doi.org/10.1039/C4RA13734E)
12. W. S. Koe, J. W. Lee, W. C. Chong, Y. L. Pang, L. C. Sim, *Environ. Sci. Pollut.* **27** (2020) 2522 (https://doi.org/10.1007/s11356-019-07193-5)
13. S. Zhu, D. Wang, *Adv. Energy Mater.* **7** (2017) 1700841 (https://doi.org/10.1002/aenm.201700841)
14. A. Malathi, J. Madhavan, M. Ashokkumar, P. Arunachalam, *Appl. Catal., A* **555** (2018) 47 (https://doi.org/10.1016/j.apcata.2018.02.010)
15. M. Guo, Q. He, A. Wang, W. Wang, Z. Fu, *Crystals* **6** (2016) 81 (https://doi.org/10.3390/cryst6070081)
16. O. Monfort, G. Plesch, *Environ. Sci. Pollut.* **25** (2018) 19362 (https://doi.org/10.1007/s11356-018-2437-9)
17. H. L. Tan, R. Amal, Y. H. Ng, *J. Mater. Chem., A* **5** (2017) 16498 (https://doi.org/10.1039/C7TA04441K)
18. Y. Li, D. Liao, T. Li, W. Zhong, X. Wang, X. Hong, H. Yu, J. *Colloid Interface Sci.* **570** (2020) 232 (https://doi.org/10.1016/j.jcis.2020.02.093)
19. S. Obregón, G. Colón, *RSC Adv.* **4** (2014) 6920 (https://doi.org/10.1039/c3ra46603e)
20. X.-J. Wen C. G. Niu, L. Zhang, C. Liang, H. Guo, G. M. Zeng, *J. Catal.* **358** (2018) 141 (https://doi.org/10.1016/j.jcat.2017.11.029)
21. B. Zhang, H. Zhang, Z. Wang, X. Zhang, X. Qin, Y. Dai, Y. Liu, P. Wang, Y. Li, B. Huang, *Appl. Catal.* **211** (2017) 258 (https://doi.org/10.1016/j.apcatb.2017.03.078)
22. D. B. Hernández-Uresti, C. Alanis-Moreno, D. Sanchez-Martinez, *Mater. Sci. Semicond.* **102** (2019) 104585 (https://doi.org/10.1016/j.mssp.2019.104585)
23. K. Pingmuang, J. Chen, W. Kangwansupamonkon, G. G. Wallace, S. Phanichphant, A. Nattestad, *Sci. Rep.* **7** (2017) 8929 (https://doi.org/10.1038/s41598-017-09514-5)
24. Z. Ye, X. Xiao, J. Chen, Y. Wang, *Photochem. Photobiol., A* **368** (2018) 153 (https://doi.org/10.1016/j.jphotochem.2018.09.044).
25. J. Yang, Q. Shi, R. Zhang, M. Xie, X. Jiang, F. Wang, X. Cheng, W. Han, *Carbon* **138** (2018) 118 (https://doi.org/10.1016/j.carbon.2018.06.003)
26. Y. Hu, W. Chen, J. Fu, M. Ba, F. Sun, P. Zhang, J. Zou, *App. Surf. Sci.*, **436** (2018) 319 (https://doi.org/10.1016/j.apsusc.2017.12.054)
27. W. Li, Z. Wang, D. Kong, D. Du, M. Zhou, Y. Du, T. Yan, J. You, D. Kong, *J. Alloys Compd*. **688** (2016) 703 (http://dx.doi.org/10.1016/j.jallcom.2016.07.249)
28. Y.-R. Lv, C.-J. Liu, R.-K. He, X. Li, Y.-H. Xu, *Mater. Res. Bull*. **117** (2019) 35 (https://doi.org/10.1016/j.materresbull.2019.04.032)
29. K. T. Drisya, M. Solís-López, J. J. Ríos-Ramírez, J. C. Durán-Álvarez, A. Rousseau, S. Velumani, R. Asomoza, A. Kassiba, A. Jantrania, H. Castaneda, *Sci. Rep*. **10** (2020) 13507 (https://doi.org/10.1038/s41598-020-69032-9)

30. G, Longo, F. Fresno, S. Gross, U. L. Štangar, *Environ. Sci. Pollut. Res.* **21** (2014) 11189 (https://doi.org/10.1007/s11356-014-2624-2)
31. S. Okunaka, H. Tokudome, Y. Hitomi, R. Abe*, J. Mater. Chem., A* **4** (2016) 3926 (https://doi.org/10.1039/C5TA09789D)
32. Y. Zhou, G. Jiang, R. Wang, X. Wang, R. Hu, X. Xi, *J. Fiber Bioeng. Inform.* **5** (2012) 181 (https://doi.org/10.3993/jfbi06201207)
33. L. Zhang, G. Tan, S. Wei, H. Ren, A. Xia, Y. Luo, *Ceram. Int.* **39** (2013) 8597 (https://doi.org/10.1016/j.ceramint.2013.03.106)
34. D. Li, H. Song, X. Meng, T. Shen, J. Sun, W. Han, X. Wang, *Nanomaterials (Basel)* **10** (2020) 546 (https://doi.org/10.3390/nano10030546)
35. M. Jiméenez-Salcedo, M. Monge, M. T. Tena, *Chemosphere* **247** (2020) 125910 (https://doi.org/10.1016/j.chemosphere.2020.125910)
36. T. Ahamad, M. Naushad, S. M. Alshehri, *Chem. Eng. J.* **417** (2021) 127969 (https://doi.org/10.1016/j.cej.2020.127969)
37. T. G. Vasconcelos, D. M. Henriques, A. König, A. F. Martins, K. Kümmerer, *Chemosphere* **76** (2009) 487 (https://doi.org/10.1016/j.chemosphere.2009.03.022)
38. Y. Kang, Y. Yang, L.-C. Yin, X. Kang, G. Liu, H.-M. Cheng, *Adv. Mater.* **27** (2015) 4572 (https://doi.org/10.1002/adma.201501939)
39. N. D. Van, D. T. A. Thu, N. T. H. Le, Do. T. Anh, *Mater. Sci. Eng., B* **278** (2022) 115616 (https://doi.org/10.1016/j.mseb.2022.115616).

Journal of the Serbian Chemical Society
JSCS-info@shd.org.rs • www.shd.org.rs/JSCS
J. Serb. Chem. Soc. 91 (6) 649–663 (2026)
JSCS–5516
Original scientific paper
Published 2 July, 2026

Fabrication of visible-light photoactive $TiO_2/BiVO_4$ composite for photocatalytic degradation of ciprofloxacin

THU LOAN DANG[1], VU VAN TU[2], THI HUE NGUYEN[2], DUC VAN NGUYEN[3]* and THI THAO TA[1]**

[1]*Faculty of Chemistry, VNU University of Science, 19 Le Thanh Tong, 100000, Vietnam,* [2]*Institute of Science and Technology for Energy and Environment, Vietnam Academy of Science and Technology, 18 Hoang Quoc Viet, Nghia Do Ward, Hanoi 100000, Vietnam and* [3]*Institute of Materials Science, Vietnam Academy of Science and Technology, 18 Hoang Quoc Viet, Nghia Do Ward, Hanoi 100000, Vietnam*

(Received 13 June, revised 30 June, accepted 2 December 2025)

Abstract: Pure $BiVO_4$ and three $TiO_2/BiVO_4$ composite photocatalysts with Bi^{3+}:Ti^{4+} mole ratios of 1:1, 2:1 and 4:1 were readily synthesized, for the first time, using a one-pot hydrothermal procedure for the photodegradation of ciprofloxacin. Conducting the hydrothermal reaction in a basic medium yielded single-phase scheelite monoclinic polymorphic $BiVO_4$ (ms-$BiVO_4$) in the composite samples. Microstructural analysis showed spherical TiO_2 nanoparticles with an average grain size of 120 nm embedded on the surface of $BiVO_4$ nanoplates. The optimized composite exhibited a ciprofloxacin photodegradation reaction rate constant about 3.8 times higher than that of the pure $BiVO_4$ sample. This significant enhancement is attributed to the formation of a $TiO_2/BiVO_4$ heterojunction, which promotes efficient charge separation. This research expands the knowledge on designing of $BiVO_4$-rich composites (with Bi^{3+}:Ti^{4+} mole ratio ≥ 1:1) *via* heterogeneous junction engineering to enhance photocatalytic activity beyond that of pure $BiVO_4$. The research also provided a perspective on using the $BiVO_4$-rich composites as effective photocatalysts for degradation of antibiotics in aqueous media under visible-light irradiation.

Keywords: photocatalysis; semiconductor; heterojunctions; antibiotic residues; hydrothermal.

INTRODUCTION

Over the last years, the widespread use of antibiotics in veterinary and human medicine has resulted in an increased risk for water contamination, as they are treat even at trace concentrations.[1,2] Particularly, it is estimated that many tons of antibiotic residues are released into the environment in Southeast Asia annually.[3] The

*,** Corresponding authors. E-mail: (*)vannd@ims.vast.ac.vn; (**)tathithao@hus.edu.vn
https://doi.org/10.2298/JSC250613001D

World Health Organization (WHO) typically reports that pharmaceutical concentrations in surface waters, groundwater and partially treated water were below 0.1 μg L^{-1} and concentrations in treated water were generally below 0.05 μg L^{-1}.[4] The emerging environmental issue relating to antibiotic residues not only threatens public health but also compromises the effectiveness of the drugs themselves (*i.e.*, contributing to antibiotic resistance). Among the quinolone antibiotics class, ciprofloxacin (CFX) is widely utilized due to its broad-spectrum activity against many pathogenic bacteria. After medication, CFX can be partially broken down by metabolism in human or animal bodies and largely excreted in its pharmacologically active forms.[5,6] Therefore, practical and economical processes are urgently required to reduce the CFX antibiotic discharge into the environment.

To overcome this environmental challenge, various processes have been applied to degrade or remove contaminants, including adsorption, photocatalysis, biodegradation and electrochemical treatment.[7] While conventional treatments like filtration and coagulation/flocculation/sedimentation require subsequent procedure to treat the pollutants, other current techniques such as membrane, ozonation and Fenton process often bring weakness in the high costs of installation, investment and operation.[1,8,9] Consequently, photocatalytic semiconductors based on the advanced oxidation process (AOPs) are highly recommended. This technology is recognized largely as one of the most low-cost, sustainable and environmentally friendly approaches for wastewater treatment.[10–13]

Monoclinic bismuth orthovanadate ($BiVO_4$), an *n*-type semiconductor, widely recognized as a promising solar-driven photocatalyst due to its narrow band gap (2.4 eV). $BiVO_4$ exhibits outstanding features: nontoxic nature, high stability towards photocorrosion, low production cost, relatively strong oxidation properties for the decomposition of organic pollutants and its promising application as a photoanode material for water splitting. Nevertheless, the performance of the single component $BiVO_4$ is still restricted by the fast recombination of photoinduced carriers (electron/hole pairs).[14–17] To date, various alternative strategies have been investigated to overcome limitation of $BiVO_4$, including cocatalyst loading, construction of heterostructures, and substitution of the metal cation or anion.[18–22] For the research approach of constructing heterostructures, $BiVO_4$ was assembled with another semiconductor to form a heterojunction that can significantly reduce the combination and speed up the separation rate of photogenerated charge carriers.[23–25] To couple with $BiVO_4$ to form these heterostructures, one of the most frequently-used semiconductors that serve as a second component is anatase titanium dioxide (TiO_2) – a well-known photocatalyst with the band gap value of 3.2 eV to benefit its high chemical stability, and excellent photocatalytic activity.[26–30] Although numerous researches on TiO_2/$BiVO_4$ photocatalytic composites have been reported, an optimized synthesis procedure has not been established. In addition, most published synthesis procedures of these photocatalytic

composites usually involve multi-steps, and to date, only limited number of one-pot approaches have been described in the literature.[28,30] Lv *et al*. applied one-pot hydrothermal procedure to synthesize $TiO_2/BiVO_4$ nanocomposites with Bi^{3+}:Ti^{4+} mole ratios less than 0.2:1.[28] The photocatalytic efficiency of 60 % for photodegradation reaction of rhodamine B over the optimized sample after 4 h of visible-light irradiation. For $TiO_2/BiVO_4$ system, to the best of our knowledge, TiO_2-rich composites were studied the most,[19,26–28,30] while only one work focusing on $BiVO_4$-rich composites with Bi^{3+}:Ti^{4+} mole ratio equals to or over 1:1 was reported.[29] However, the effects of Bi^{3+}:Ti^{4+} mole ratio on the photocatalytic efficiency of $BiVO_4$-rich composites were not studied systematically by Drisya *et al.* for they only investigated Bi^{3+}:Ti^{4+} mole ratio value of 1:0.6. This might originate from the fact that these researches focused mainly on improving Vis-photocatalytic performances of TiO_2 *via* designing TiO_2-based composites, in which $BiVO_4$ played role as a dopant or a minor component, rather than hindering the fast recombination of photoinduced electron-hole pairs, the main drawback of the pure $BiVO_4$, *via* designing $BiVO_4$-rich composites. In other words, the design of a heterogeneous junction to enhance photo-induced charge separation and consequently improve the photocatalytic performance of $BiVO_4$-rich composites containing anatase as a minor component for photodegradation of antibiotics in general and CPX in particular, has not been mentioned yet.

Hence, this research aimed to synthesize $TiO_2/BiVO_4$ semiconductors with Bi^{3+}:Ti^{4+} mole ratio equals to or greater than 1:1 using hydrothermal method in a basic medium, and their photocatalytic activities were determined by the degradation of CPX antibiotic in aqueous solution under visible-light irradiation.

EXPERIMENTAL PROCEDURE

Synthesis of photocatalysts

All the reagents were of analytical grade and used without any further purification. Typically, 1 mmol $Bi(NO_3)_3{\cdot}5H_2O$ (Acros) and a certain amount of TiO_2 (Sigma–Aldrich) were dissolved in 2 mL of 4 M HNO_3 solution, while 1 mmol NH_4VO_3 (Sigma–Aldrich) was dissolved in 10 mL double distilled water at 80 °C. The two solutions were mixed and transferred into a 120 mL Teflon®-lined stainless-steel autoclave. The pH of these mixtures was adjusted to 11 by addition of 12 mL of concentrated NH_3 solution (25 %). Subsequently, the autoclave was filled with double distilled water up to 75 % of its capacity. The sealed autoclave was heated at 180 °C for 24 h under autogenous pressure. After undergoing hydrothermal treatment, the precipitated solids were collected and washed with double distilled water until reaching a neutral medium. Finally, the yellow precipitates were obtained after drying naturally in air.

For the synthesis of the pure $BiVO_4$, the same synthesis procedure was performed except that no TiO_2 was added. The three composite products were denoted as $1TiO_2/4BiVO_4$, $1TiO_2/2BiVO_4$ and $1TiO_2/1BiVO_4$ corresponding to the sample with the Bi^{3+}:Ti^{4+} mole ratios of 4:1, 2:1 and 1:1, respectively.

Characterization methods

The crystalline phases of the as-synthesized samples were determined by using an X-ray diffractometer (XRD, D8 Advance, Bruker). The synthesized samples were also characterized by field-emission scanning electron microscopy (FESEM, Hitachi S-4800), high resolution transmission electron microscopy (HR-TEM, Jeol 2100), and diffuse-reflectance UV–Vis spectrometry (DR-UV–Vis, Jasco V670).

Photocatalytic properties

The photocatalytic activities of the studied composites were estimated by the degradation of ciprofloxacin (CPX) solution (0.5 ppm) at room temperature under visible-light irradiation. Typically, 0.025 g photocatalyst was added to 100 mL the antibiotic solution in each experiment. The solution was stirred for one hour in dark for reaching of adsorption-desorption equilibrium. The suspension was then irradiated by a visible-light source provided by a 100 W halogen lamp with the center wavelength of 700 nm from a distance of 20 cm. At certain interval times (30, 60, 90 and 120 min) during irradiation, 5 mL of the tested solution was taken out and was then filtrated with 0.22 μm membrane prior to concentration determination by using a LC––MS/MS system (ACQUITY UPLC H-class/Xevo-TQ, USA).

The photocatalytic degradation efficiency was calculated by the following equation:

$$H = 100\frac{C_0 - C_t}{C_0} \quad (1)$$

wherein: C_0 is the initial concentration of CPX (without any photocatalyst); C_t is the remaining concentration of CPX in the solution at time t / min after irradiation.

RESULTS AND DISCUSSION

Crystalline structure

From XRD diagrams (Fig. 1), it can be confirmed that the monoclinic scheelite structure of $BiVO_4$ (ms-$BiVO_4$) was successfully synthesized for all studied samples, namely, pure $BiVO_4$, $1TiO_2/4BiVO_4$, $1TiO_2/2BiVO_4$ and $1TiO_2/1BiVO_4$. Particularly, diffraction peaks at 2θ values of 18.65, 18.98, 28.94, 30.54, 34.49, 35.22 and 39.78° are corresponding to (1 1 0), (0 1 1), (–1 3 0), (0 4 0), (2 0 0), (0 0 2) and (2 1 1) lattice planes of monoclinic scheelite structure of $BiVO_4$ (JCPDS card No. 14-0688), respectively. Moreover, the doublet peaks at 2θ values of around 18.5 and 35° can be a useful mark to distinguish a monoclinic scheelite phase and a tetragonal scheelite phase of $BiVO_4$.[31]

The result indicated that, by carrying out the hydrothermal synthesis procedure in basic medium, the monoclinic scheelite structure was controlled to grow as a unique crystalline phase of $BiVO_4$ and the coexistence of monoclinic scheelite and tetragonal zircon, as reported previously, was avoided.[32] In another word, the formation of tetragonal zircon phase, a thermodynamically stable polymorph of $BiVO_4$ under the acidic medium of hydrothermal synthesis reaction, was totally inhibited.

In addition, for all XRD patterns of $TiO_2/BiVO_4$ composite samples, a set of diffraction peaks at 2θ25.6, 38.3 and 48.8° were detected, indicating the existence

of anatase TiO_2 (JCPDS card No. 21-1272).[33] Furthermore, no other impurity was found in all investigated samples, similar to those published for $TiO_2/BiVO_4$ composites.[28–30] The intensity of anatase TiO_2 increased monotonously as desirable with the TiO_2 content in the composite samples when the Bi^{3+}:Ti^{4+} mole ratio decreased from 4:1 to 1:1. It is also worthy to note that by the coupling with anatase TiO_2 to form photocatalytic composites, the calculated lattice parameters of the monoclinic scheelite $BiVO_4$ existed in pure $BiVO_4$, $1TiO_2/4BiVO_4$, $1TiO_2/2BiVO_4$ and $1TiO_2/1BiVO_4$ samples were almost unchanged as tabulated in Table I.

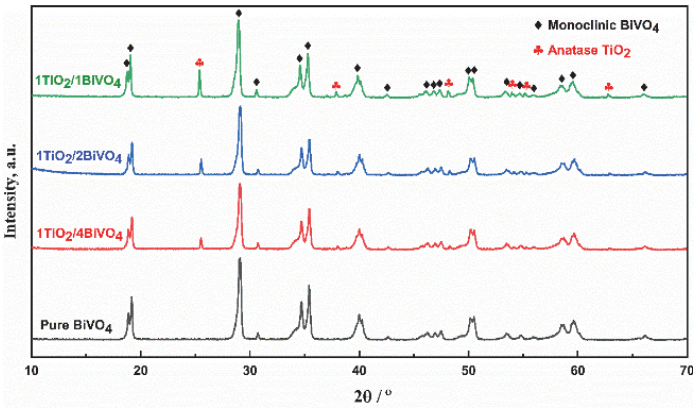

Fig. 1. XRD patterns of pure 9+$BiVO_4$ and $TiO_2/BiVO_4$ composite samples.

TABLE I. The calculated lattice parameters () of pure $BiVO_4$, $1TiO_2/4BiVO_4$, $1TiO_2/2BiVO_4$ and $1TiO_2/1BiVO_4$ samples

Sample	Lattice parameters			
	a / Å	*b* / Å	*c* / Å	*β* / °
Pure $BiVO_4$	5.194(2)	11.699(2)	5.090(1)	90.38(1)
$1TiO_2/1BiVO_4$	5.195(1)	11.701(3)	5.089(2)	90.37(2)
$1TiO_2/2BiVO_4$	5.194(3)	11.700(2)	5.091(3)	90.38(2)
$1TiO_2/4BiVO_4$	5.194(1)	11.700(1)	5.092(2)	90.38(1)

Microstructures

To investigate the morphology of the synthesized $TiO_2/BiVO_4$ composite, the $1TiO_2/4BiVO_4$ and $1TiO_2/1BiVO_4$ samples were subjected to SEM observation as examples. The SEM image of the composite material, as shown in Figs. 2 and 3, reveals the presence of spherical-like TiO_2 nanoparticles with the average grain size of 120 nm embedded on the surface of $BiVO_4$ in contrast to that of the pure $BiVO_4$. This agrees well with the statement given for XRD patterns. For both cases of pure $BiVO_4$ and $TiO_2/BiVO_4$ composites, the $BiVO_4$ nanoplates with average width of 200 nm and length of 300 nm are observed.

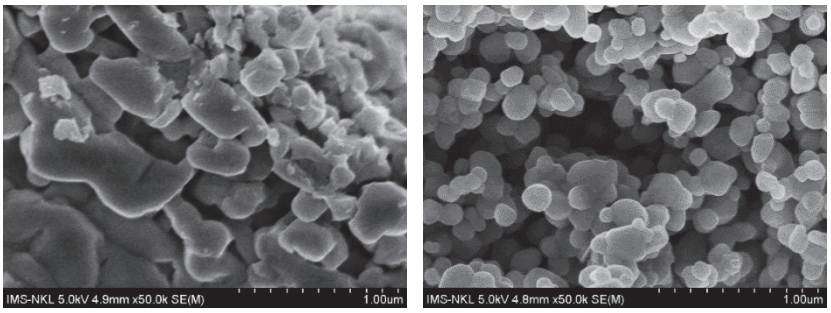

(a) (b)

Fig. 2. SEM images of: a) pure $BiVO_4$ and b) $1TiO_2/4BiVO_4$ samples.

Compared to the case of commercialized TiO_2 precursor, the shape and average grain size TiO_2 nanoparticles existed in $TiO_2/BiVO_4$ composite are almost unchanged, suggesting the inhibition role of basic medium on grain growth of TiO_2 (Fig. 3).[34]

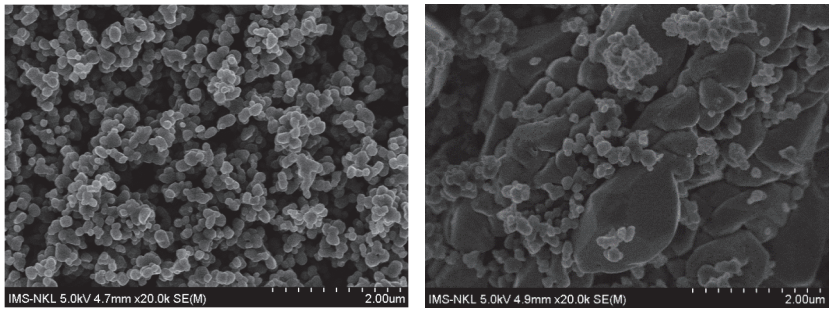

(a) (b)

Fig. 3. SEM images of :a) commercialized TiO_2 precursor and b) $1TiO_2/1BiVO_4$ composite.

To investigate further the microstructure of as-synthesized samples, the HR--TEM image and its corresponding FFT pattern of $1TiO_2/1BiVO_4$ composite sample were presented in Fig. 4a and b, respectively. Two lattice fringe spacings of 0.292 and 0.467 nm with an interfacial angle of 66.5° that are assigned to (0 4 0) and (0 1 1) lattice planes of ms-$BiVO_4$, respectively, were observed in both HR--TEM image and its corresponding FFT pattern. At the same time, two other lattice fringe spacings of 0.347 and 0.469 nm that formed an included angle of 68.3° were interpreted respectively as (0 1 1) and (0 0 2) lattice planes of anatase TiO_2 phase. These calculated results indicated obviously that the investigated $1TiO_2/1BiVO_4$ contained both ms-$BiVO_4$ and anatase TiO_2 particles. Moreover, as shown in Fig. 4a, the direct contact between ms-$BiVO_4$ nanoplates and anatase TiO_2 nanoparticles was observed, suggesting the formation of heterojunction between them.

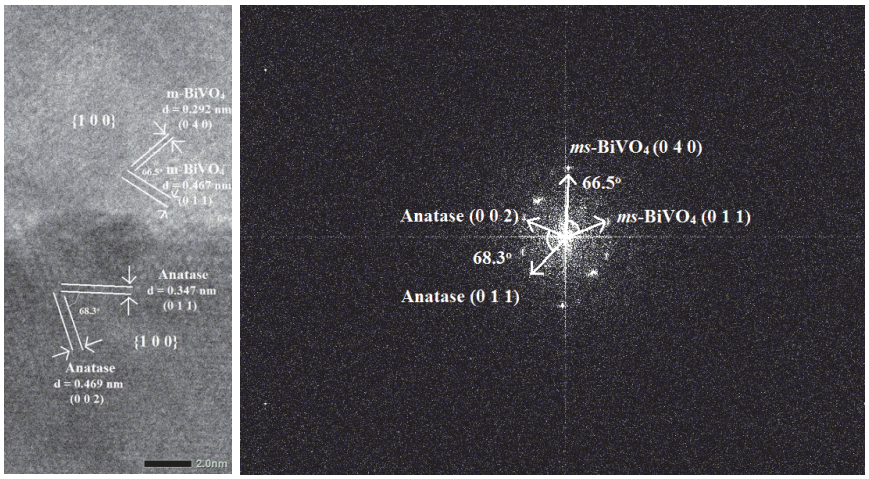

(a) (b)

Fig. 4. a) HR-TEM image and b) its corresponding FFT pattern of $1TiO_2/1BiVO_4$ composite sample.

Diffuse-reflectance (DR) UV–Vis spectra

From the spectra received by DR UV–Vis measurements as shown in Fig. 5, a derived Tauc's plot was then depicted in Fig. 6 that showed the relationship between $h\nu$ (the energy of the light) and $(\alpha h\nu)^2$, where α was the absorption coefficient of the material. Based on extrapolating the linear region in Fig. 6, the band gap (E_g) values of synthesized photocatalysts were estimated to be 2.43, 2.42 and 2.44 eV, corresponding to the 4:1, 2:1 and 1:1 composite samples, respectively. The results showed the absorption feature of the composite materials and the pure $BiVO_4$ as well (E_g = 2.42 eV), in visible region, did not have a significant difference. Therefore, to conclude which as-prepared material was exhibiting the best photocatalytic activity, it was necessary to perform further photocatalytic tests with

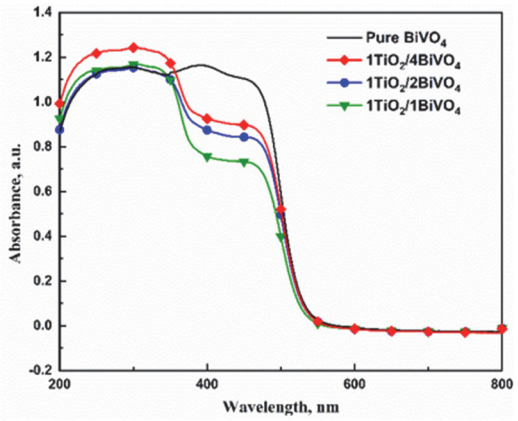

Fig. 5. Diffuse-reflectance UV–Vis spectra of pure $BiVO_4$ and $BiVO_4/TiO_2$ composites.

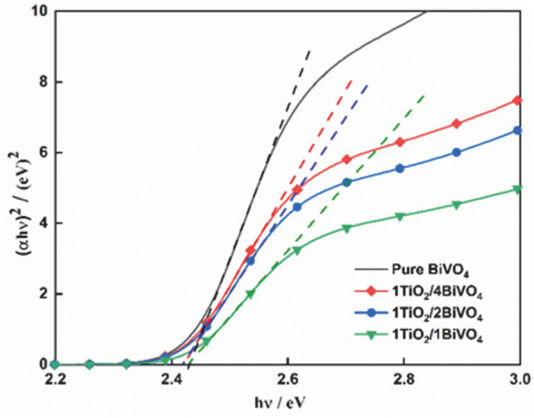

Fig. 6. Tauc's plots of pure $BiVO_4$ and $BiVO_4/TiO_2$ composites.

the analyte (*i.e.* ciprofloxacin (CFX)). However, the band gap values of around 2.4 eV suggested that photocatalytic experiments should be performed under visible-light irradiation.

Photocatalytic activities

Photocatalytic activities of as-synthesized samples were evaluated according to the degradation of CFX. These experiments included the photocatalytic degradation of only CFX solution without any photocatalyst; ciprofloxacin and pure $BiVO_4$ (CFX+$BiVO_4$); ciprofloxacin and 4:1 composite (CFX+1TiO_2/4$BiVO_4$); and CFX and 1:1 composite (CFX+1TiO_2/1$BiVO_4$). The photocatalytic degradation efficiency, after that, was illustrated in Fig. 7.

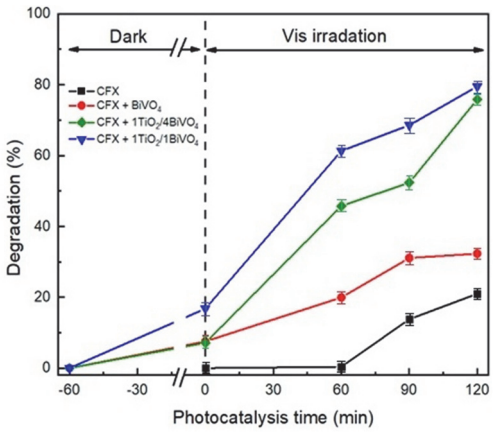

Fig. 7. Photocatalytic degradation efficiency of ciprofloxacin with and without the as-prepared photocatalysts under irradiation using a 100 W halogen lamp.

The results showed that after 120 min under visible-light irradiation, while CFX was degraded only 32 % in the activity of pure $BiVO_4$, but it was decomposed 75 and 80 % by 1TiO_2/4$BiVO_4$ and 1TiO_2/1$BiVO_4$, respectively. Thus, similar to the previous works, the composite materials were visible-light photoactive with

their photodegradation efficiency obviously twice as high as that of the pure $BiVO_4$ sample.[19,23,28] The existence of a heterojunction formed between $BiVO_4$ nanoplates and embedded 120 nm spherical-like TiO_2 nanoparticles can probably be attributed to this significant improvement in ciprofloxacin photodegradation efficiency of the studied $TiO_2/BiVO_4$ composites with respect to that of the pure $BiVO_4$. Also, it can be derived from Fig. 7 that, after reaching of adsorption-desorption equilibrium, the CFX adsorption percentage of pure $BiVO_4$ and $1TiO_2$/ /$4BiVO_4$ samples was around 7 % and was almost the same while that of $1TiO_2$/ /$1BiVO_4$ sample was higher (17 %). That can be explained by the fact that, the $1TiO_2/1BiVO_4$ sample possessed the higher amount of spherical-like anatase TiO_2 nanoparticles, with relatively high specific surface area (of around 10 m^2/g), than pure $BiVO_4$ and $1TiO_2/4BiVO_4$ samples. In addition, the kinetics of the CFX photodegradation reactions over pure $BiVO_4$ and $1TiO_2/1BiVO_4$ samples was also investigated. The obtained results indicated that the CFX photodegradation reactions over these two samples can be described by the first-order kinetic equation (Fig. 8):

$$\ln(C_0 / C_t) = kt \tag{2}$$

where C_0 is the initial CFX concentration, C_t is the CFX concentration at reaction time t, and k is the observed first-order rate constant. The photodegradation reaction rate constant of 0.00899° min^{-1} calculated for the $1TiO_2/1BiVO_4$ sample was about 3.8 times higher than that of the pure $BiVO_4$ sample (0.00235° min^{-1}) (Fig. 8, the inset).

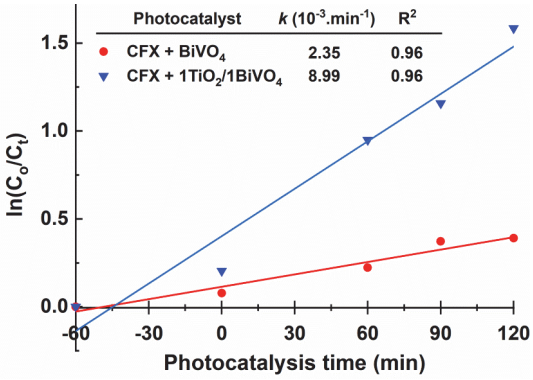

Fig. 8. The dependence of $\ln(C_0/C_t)$ on the visible-light irradiation time of the optimized $1TiO_2/1BiVO_4$ and the pure $BiVO_4$ samples.

From m/z values obtained from LC–QTOFMS spectrum for the photodegradation of CFX over the optimized $1TiO_2/1BiVO_4$ sample under visible-light irradiation, two major possible intermediate products, denoted as CFX1 and CFX2, were detected (Table II). The ion at m/z 314.1 can be assigned to the dehydration of the CFX to produce CFX1.[35] The quinolone moiety of the CFX was attacked by the produced •OH radicals, leading to a decarboxylation process to form CFX2 with m/z value of 288.1.[36] Based on these data, a CFX photocatalytic degradation

pathways under visible-light irradiation was proposed as shown in Scheme 1.[36,37] Accordingly, in a first step of the photodegradation reaction, CFX2 was formed as an intermediate product from the CFX under visible-light irradiation. By increasing the photocatalytic reaction time further, CFX2 was degraded into smaller substances. The photocatalytic reaction was completed when all available intermediate products of photodegradation reaction were mineralized into H_2O and CO_2 as final compounds.[36,37]

TABLE II. Major *m*/*z* values and chemical formula of possible intermediate products detected by LC-MS/MS for the photodegradation of ciprofloxacin under visible-light irradiation

No.	Intermediate product	*m*/*z*	Possible chemical formula
1	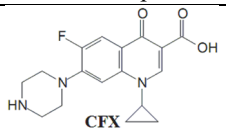 CFX	332.1	$C_{17}H_{18}FN_3O_3$
2	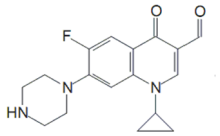 CFX1	314.1	$C_{17}H_{17}FN_3O_2$
3	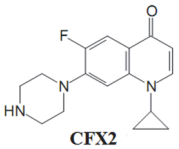 CFX2	288.1	$C_{16}H_{18}FN_3O$

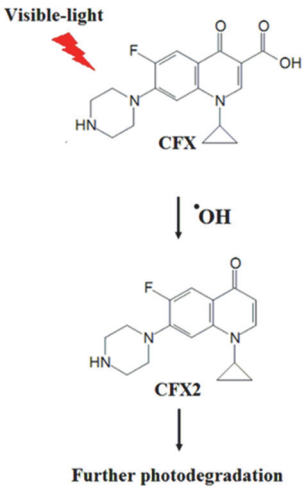

Scheme 1. Proposed reaction pathways and intermediate products generated in the photodegradation reaction of ciprofloxacin under visible-light irradiation.

In Fig. 9 the recyclability testing results of CFX over the optimized $1TiO_2$/ /$1BiVO_4$ sample for three recycling photocatalytic runs under visible-light

irradiation are shown. The results illustrate that the photodegradation efficiency decreased slightly to 79.2 and 78.8 % for the second and third cycles, respectively from the value of 80 % for the first cycle. The CFX photodegraded species existing on the composite's surface might block the photoactive sites, leading to this slight decrease in photodegradation efficiency. This implied that our optimized TiO_2/ /$BiVO_4$ composite sample can be reusable with high photocatalytic stability.

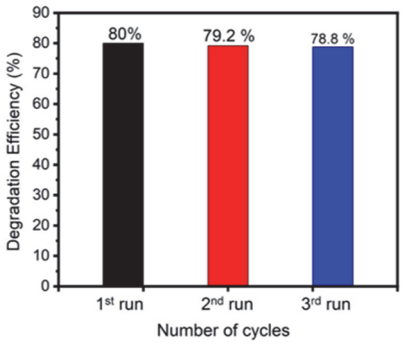

Fig. 9. Photodegradation recyclability test of ciprofloxacin over the optimized $1TiO_2/1BiVO_4$ sample under visible-light irradiation.

Similar to the previous studies,[27,38,39] the photocatalytic activity-enhancing mechanism for CFX photodegradation in aqueous medium under visible-light irradiation over the $BiVO_4$-rich composites containing anatase as a minor component can be proposed as follows.

1) The incident light was absorbed mainly by the Vis-photoactive $BiVO_4$ component of $TiO_2/BiVO_4$ composite, leading to the generation of photo-induced pairs electron-hole pairs:

$$h\nu + \text{ms-}BiVO_4 \rightarrow h^+_{VB} + e^-_{CB} \quad (3)$$

2) *Via* the heterojunction formed between ms-$BiVO_4$ nanoplates and TiO_2 nanoparticles, the photo-induced electrons in the conduction band of anatase TiO_2 were transferred to that of $BiVO_4$ while holes in the valence band of $BiVO_4$ were transferred to that of anatase TiO_2 under visible-light irradiation (Scheme 2).

3) The photo-induced charge transfer *via* heterojunction led to the increase in lifetime of electron-charge separation of the $TiO_2/BiVO_4$ composites. This transfer was supposed to depend on the Bi^{3+}:Ti^{4+} mole ratio of this photocatalytic composite. The highest photocatalytic efficiency was found for the composite with the highest Bi^{3+}:Ti^{4+} mole ratio of 4:1 while the pure $BiVO_4$ sample exhibited the fastest photo-induced charge recombination due to the absence of a charge transferring process. The further increase in TiO_2 to decrease Bi^{3+}:Ti^{4+} mole ratio down to 1:1, however, lowered the composite's photocatalytic activity. This was probably due to multiple trapping of photo-induced charges.[35]

4) At the composite's surface, the dissolved oxygen in aqueous medium was oxidized by photo-induced electrons to active free radical species such as $O_2^{\bullet-}$ and $^{\bullet}OH$:

$$e^- + O_2 \rightarrow O_2^{\bullet-} \quad (4)$$

$$O_2^{\bullet-} + H^+ + e^- \rightarrow {}^{\bullet}OH + H^- \quad (5)$$

5) The electron donors (H_2O) reacted with photo-induced holes at the composite's surface to produce $^{\bullet}OH$:

$$h^+ + H_2O \rightarrow {}^{\bullet}OH + H^+ \quad (6)$$

6) The photo-induced holes and other freshly-produced free radicals like $O_2^{\bullet-}$, $^{\bullet}OH$, *etc.* oxidized the surface-adsorbed CFX (CFX_{ad}) molecules to form photodegraded species like CO_2, H_2O and other by-products:

$$CFX_{ad} + h^+ / {}^{\bullet}OH / O_2^{\bullet-} \rightarrow CO_2 + H_2O + \text{other by-products} \quad (7)$$

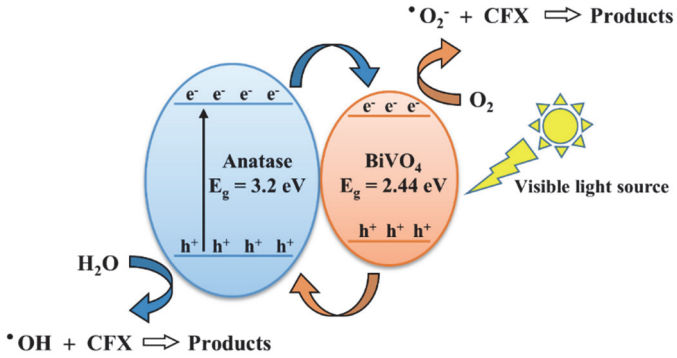

Scheme 2. The proposed photocatalytic mechanism of $1TiO_2/1BiVO_4$ sample for CFX photodegradation under visible-light irradiation.

CONCLUSION

Pure $BiVO_4$ and three $TiO_2/BiVO_4$ composite samples with mole ratios of 1:1, 2:1 and 4:1 were readily synthesized at a pH of 11 *via* hydrothermal method. Under the hydrothermal conditions, only a single-phase scheelite monoclinic polymorphic type of $BiVO_4$ (ms-$BiVO_4$) was obtained, and the $BiVO_4$ nanoplates had average width of 200 nm and length of 300 nm.

Compared to the case of the pure $BiVO_4$, the photocatalytic degradation rate of ciprofloxacin over the $TiO_2/BiVO_4$ composites was significantly higher, and the $1TiO_2/1BiVO_4$ sample was expected to be the most potential photocatalyst with its highest efficiency of ciprofloxacin degradation after 120 min under visible-light irradiation. The enhancement in ciprofloxacin removal of the studied $TiO_2/BiVO_4$

composites might have originated from the existence of a heterojunction formed between $BiVO_4$ nanoplates and embedded 120 nm spherical-like TiO_2 nanoparticles.

ИЗВОД

СИНТЕЗА $TiO_2/BiVO_4$ КОМПОЗИТА ФОТОАКТИВНОГ НА ВИДЉИВУ СВЕТЛОСТ ЗА ФОТОКАТАЛИТИЧКУ ДЕГРАДАЦИЈУ ЦИПРОФЛОКСАЦИНА

THU LOAN DANG[1], VU VAN TU[2], THI HUE NGUYEN[2], DUC VAN NGUYEN[3] и THI THAO TA[1]

[1]Faculty of Chemistry, VNU University of Science, 19 Le Thanh Tong, 100000, Vietnam, [2]Institute of Science and Technology for Energy and Environment, Vietnam Academy of Science and Technology, 18 Hoang Quoc Viet, Nghia Do Ward, Hanoi 100000, Vietnam и [3]Institute of Materials Science, Vietnam Academy of Science and Technology, 18 Hoang Quoc Viet, Nghia Do Ward, Hanoi 100000, Vietnam

Чист $BiVO_4$ и три $TiO_2/BiVO_4$ композитна фотокатализатора са молским односима Bi^{3+}:Ti^{4+} од 1:1, 2:1 и 4:1 успешно су синтетисани по први пут применом „*one-pot*“ хидротермалне процедуре за фотодеградацију ципрофлоксацина. Извођење хидротермалне реакције у базној средини резултирало је стварањем једнофазног моноклиничног $BiVO_4$ (ms-$BiVO_4$) структуре шелита у узорцима композита. Микроструктурна анализа показала је сферичне наночестице TiO_2, просечне величине зрна од 120 nm, које су уграђене на површину наноплоча $BiVO_4$. Оптимизовани композит показао је константу брзине реакције фотодеградације ципрофлоксацина која је била око 3.8 пута већа у поређењу са узорком чистог $BiVO_4$. Ово значајно побољшање приписује се формирању $TiO_2/BiVO_4$ хетеројединења које поспешује ефикасно раздвајање наелектрисања. Ово истраживање проширује знање о дизајнирању композита богатих са $BiVO_4$ (са молским односом Bi^{3+}:Ti^{4+} ≥ 1:1) путем инжењеринга хетерогених спојева ради побољшања фотокаталитичке активности изнад нивоа чистог $BiVO_4$. Истраживање је такође пружило перспективу о коришћењу композита богатих $BiVO_4$ као ефикасних фотокатализатора за деградацију антибиотика у воденим растворима, под зрачењем видљивом светлошћу.

(Примљено 13. јуна, ревидирано 30. јуна, прихваћено 2. децембра 2026)

REFERENCES

1. V. Homem, L. Santos, *J. Environ. Manage.* **92** (2011) 2304 (https://doi.org/10.1016/j.jenvman.2011.05.023)
2. C. Yan, Y. Yang, J. Zhou, M. Liu, M. Nie, H. Shi, L. Gu, *Environ. Pollut.* **175** (2013) 22 (https://doi.org/10.1016/j.envpol.2012.12.008)
3. C. S. Lundborg, A. Tamhankar, *BMJ.* **358** (2017) j2440 (https://doi.org/10.1136/bmj.j2440)
4. *Pharmaceuticals in drinking-water,* World Health Organization, Geneva, 2012, p. 35 (https://apps.who.int/iris/handle/10665/44630)
5. S. Babić, M. Periša, I. Škorić, *Chemosphere* **91** (2013) 1635 (https://doi.org/10.1016/j.chemosphere.2012.12.072)
6. J. Porras, C. Badoya, J. Silva-Agredo, A. Santamaría, J. J. Fernández, R. A. Torres--Palma, *Water Res.* **94** (2016) 1 (https://doi.org/10.1016/j.watres.2016.02.024)
7. Z. Wei, J. Liu, W. Shangguan, *Chinese J. Catal.* **41** (2020) 1440 (https://doi.org/10.1016/S1872-2067(19)63448-0)
8. K. Košutić, D. Dolar, D. Ašperger, B. Kunst, *Sep. Purif. Technol.* **53** (2007) 244 (https://doi.org/10.1016/j.seppur.2006.07.015)

9. C. A. Igwegbe, S. N. Oba, C. O. Aniagor, A. G. Adeniyi, *Ind. Eng. Chem. Res.* **93** (2021) 57 (https://doi.org/10.1016/j.jiec.2020.09.023)
10. M. N. Chong, B. Jin, C. W. K. Chow, C. Saint, *Water Res.* **44** (2010) 2997 (https://doi.org/10.1016/j.watres.2010.02.039)
11. S. Dong, J. Feng, M. Fan, Y. Pi, L. Hu, X. Han, M. Liu, J. Sun, J. Sun, *RSC Adv.* **5** (2015) 14610 (https://doi.org/10.1039/C4RA13734E)
12. W. S. Koe, J. W. Lee, W. C. Chong, Y. L. Pang, L. C. Sim, *Environ. Sci. Pollut.* **27** (2020) 2522 (https://doi.org/10.1007/s11356-019-07193-5)
13. S. Zhu, D. Wang, *Adv. Energy Mater.* **7** (2017) 1700841 (https://doi.org/10.1002/aenm.201700841)
14. A. Malathi, J. Madhavan, M. Ashokkumar, P. Arunachalam, *Appl. Catal., A* **555** (2018) 47 (https://doi.org/10.1016/j.apcata.2018.02.010)
15. M. Guo, Q. He, A. Wang, W. Wang, Z. Fu, *Crystals* **6** (2016) 81 (https://doi.org/10.3390/cryst6070081)
16. O. Monfort, G. Plesch, *Environ. Sci. Pollut.* **25** (2018) 19362 (https://doi.org/10.1007/s11356-018-2437-9)
17. H. L. Tan, R. Amal, Y. H. Ng, *J. Mater. Chem., A* **5** (2017) 16498 (https://doi.org/10.1039/C7TA04441K)
18. Y. Li, D. Liao, T. Li, W. Zhong, X. Wang, X. Hong, H. Yu, J. *Colloid Interface Sci.* **570** (2020) 232 (https://doi.org/10.1016/j.jcis.2020.02.093)
19. S. Obregón, G. Colón, *RSC Adv.* **4** (2014) 6920 (https://doi.org/10.1039/c3ra46603e)
20. X.-J. Wen C. G. Niu, L. Zhang, C. Liang, H. Guo, G. M. Zeng, *J. Catal.* **358** (2018) 141 (https://doi.org/10.1016/j.jcat.2017.11.029)
21. B. Zhang, H. Zhang, Z. Wang, X. Zhang, X. Qin, Y. Dai, Y. Liu, P. Wang, Y. Li, B. Huang, *Appl. Catal.* **211** (2017) 258 (https://doi.org/10.1016/j.apcatb.2017.03.078)
22. D. B. Hernández-Uresti, C. Alanis-Moreno, D. Sanchez-Martinez, *Mater. Sci. Semicond.* **102** (2019) 104585 (https://doi.org/10.1016/j.mssp.2019.104585)
23. K. Pingmuang, J. Chen, W. Kangwansupamonkon, G. G. Wallace, S. Phanichphant, A. Nattestad, *Sci. Rep*. **7** (2017) 8929 (https://doi.org/10.1038/s41598-017-09514-5)
24. Z. Ye, X. Xiao, J. Chen, Y. Wang, *Photochem. Photobiol., A* **368** (2018) 153 (https://doi.org/10.1016/j.jphotochem.2018.09.044).
25. J. Yang, Q. Shi, R. Zhang, M. Xie, X. Jiang, F. Wang, X. Cheng, W. Han, *Carbon* **138** (2018) 118 (https://doi.org/10.1016/j.carbon.2018.06.003)
26. Y. Hu, W. Chen, J. Fu, M. Ba, F. Sun, P. Zhang, J. Zou, *App. Surf. Sci.*, **436** (2018) 319 (https://doi.org/10.1016/j.apsusc.2017.12.054)
27. W. Li, Z. Wang, D. Kong, D. Du, M. Zhou, Y. Du, T. Yan, J. You, D. Kong, *J. Alloys Compd*. **688** (2016) 703 (http://dx.doi.org/10.1016/j.jallcom.2016.07.249)
28. Y.-R. Lv, C.-J. Liu, R.-K. He, X. Li, Y.-H. Xu, *Mater. Res. Bull*. **117** (2019) 35 (https://doi.org/10.1016/j.materresbull.2019.04.032)
29. K. T. Drisya, M. Solís-López, J. J. Ríos-Ramírez, J. C. Durán-Álvarez, A. Rousseau, S. Velumani, R. Asomoza, A. Kassiba, A. Jantrania, H. Castaneda, *Sci. Rep*. **10** (2020) 13507 (https://doi.org/10.1038/s41598-020-69032-9)
30. G, Longo, F. Fresno, S. Gross, U. L. Štangar, *Environ. Sci. Pollut. Res.* **21** (2014) 11189 (https://doi.org/10.1007/s11356-014-2624-2)
31. S. Okunaka, H. Tokudome, Y. Hitomi, R. Abe*, J. Mater. Chem., A* **4** (2016) 3926 (https://doi.org/10.1039/C5TA09789D)

32. Y. Zhou, G. Jiang, R. Wang, X. Wang, R. Hu, X. Xi, *J. Fiber Bioeng. Inform.* **5** (2012) 181 (https://doi.org/10.3993/jfbi06201207)
33. L. Zhang, G. Tan, S. Wei, H. Ren, A. Xia, Y. Luo, *Ceram. Int.* **39** (2013) 8597 (https://doi.org/10.1016/j.ceramint.2013.03.106)
34. D. Li, H. Song, X. Meng, T. Shen, J. Sun, W. Han, X. Wang, *Nanomaterials (Basel)* **10** (2020) 546 (https://doi.org/10.3390/nano10030546)
35. M. Jiméenez-Salcedo, M. Monge, M. T. Tena, *Chemosphere* **247** (2020) 125910 (https://doi.org/10.1016/j.chemosphere.2020.125910)
36. T. Ahamad, M. Naushad, S. M. Alshehri, *Chem. Eng. J.* **417** (2021) 127969 (https://doi.org/10.1016/j.cej.2020.127969)
37. T. G. Vasconcelos, D. M. Henriques, A. König, A. F. Martins, K. Kümmerer, *Chemosphere* **76** (2009) 487 (https://doi.org/10.1016/j.chemosphere.2009.03.022)
38. Y. Kang, Y. Yang, L.-C. Yin, X. Kang, G. Liu, H.-M. Cheng, *Adv. Mater.* **27** (2015) 4572 (https://doi.org/10.1002/adma.201501939)
39. N. D. Van, D. T. A. Thu, N. T. H. Le, Do. T. Anh, *Mater. Sci. Eng., B* **278** (2022) 115616 (https://doi.org/10.1016/j.mseb.2022.115616).